2004

A dual-laser-ultrasonic, nondestructive evaluation system for imaging surface-breaking cracks in aerospace materials

Adam Todd Cooney
University of Dayton

A DUAL-LASER-ULTRASONIC, NONDESTRUCTIVE EVALUATION SYSTEM FOR IMAGING SURFACE-BREAKING CRACKS IN AEROSPACE MATERIALS

Thesis

Submitted to

School of Engineering

UNIVERSITY OF DAYTON

In Partial Fulfillment of the Requirements for

the Degree

Master of Science in Electro-Optics

by

Adam Todd Cooney

UNIVERSITY OF DAYTON

Dayton, Ohio

December, 2004

A DUAL-LASER-ULTRASONIC, NONDESTRUCTIVE EVALUATION SYSTEM FOR IMAGING SURFACE-BREAKING CRACKS IN AEROSPACE MATERIALS

APPROVED BY:

Joseph Haus, Ph.D.
Advisory Committee Chairman
Director, Electro-Optics
Engineering Department

Qiwen Zhan, Ph.D.
Committee Member
Assistant Professor, Electro-Optics
Engineering Department

James L. Blackshire, Ph.D.
Committee Member
Non-Destructive Evaluation Branch
Materials and Manufacturing
Directorate
Air Force Research Laboratory

Donald L. Moon, Ph.D.
Associate Dean
Graduate Engineering Programs & Research
School of Engineering

Joseph E. Saliba, Ph.D., P.E.
Dean, School of Engineering

ABSTRACT

A DUAL-LASER-ULTRASONIC, NONDESTRUCTIVE EVALUATION SYSTEM FOR IMAGING SURFACE-BREAKING CRACKS IN AEROSPACE MATERIALS

Cooney, Adam Todd
University of Dayton

Advisor: Dr. Joseph Haus

An all optical, non-contact, laser ultrasonic system has been developed for the purpose of non-destructive detection, characterization, and imaging of surface-breaking cracks in aerospace materials. This system exploits near-field thermoelastic waveforms generated by the absorption of a Q-switched laser pulse and monitors, via heterodyne interferometry, the interaction of both the ultrasonic source and the resultant surface acoustic waves with material defects. The presence of surface cracks is detected through a localized intensification of the ultrasonic wave fields in the immediate vicinity of the defect due to near-field ultrasonic scattering mechanisms. Theoretical and experimental studies of the near-field thermoelastic source were conducted along with a systematic investigation of the ideal dual-beam scanning configuration to optimize crack-detection capabilities. An automated scanning system combined with data analysis algorithms was developed and implemented to allow for surface-breaking crack imaging.

TABLE OF CONTENTS

LIST OF ILLUSTRATIONS

LIST OF TABLES

CHAPTER I

INTRODUCTION

Early detection of defects in aerospace and industrial systems is crucial for the purpose of safety and life extension of critical equipment and machinery. The detection of surface-breaking cracks, in particular, is of major concern for aircraft systems and has, therefore, been the primary goal of researchers involved in non-destructive evaluation (NDE) for many decades[1,2]. In high-stress environments such as flight, small material defects can rapidly develop into complete component failure leading to expensive and hazardous results. An illustration, provided by Figure 1, is used to portray this evolution of a microscopic crack towards the structural failure of a material, as well as to indicate the present state of typical NDE crack detection capabilities and limits.

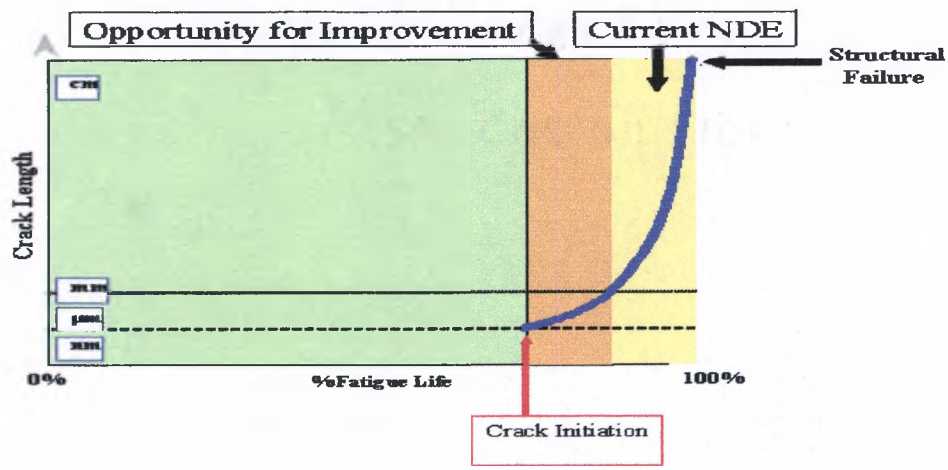

Figure 1 Effect of crack initiation and growth on life of structure and current crack detection capabilities[3].

Obviously, any detection capability which indicates the presence of a crack before structural failure provides useful and vital information which can prevent, especially in the context of aerospace components, a catastrophic outcome. Current NDE techniques detect and locate cracks between 80%-90% of the fatigue life (Figure 1), which provides some time-critical notification of potential system failures, allowing for the grounding/retirement of aircraft or the replacement of damaged components. The earliest possible crack detection, however, is not only imperative for safety purposes but affords more time for either cost effective replacement or possible life-extension remedies of the structure.

Traditional methods of ultrasonic crack detection have relied primarily on the use of contact transducers for ultrasound generation and detection[3,5-10]. Current state-of-the-art methods using contact transducers provide for detecting, locating, and sizing cracks in the 100μm – 1mm size range. Recent advances in surface-breaking crack detection include efforts to not only locate but to visualize a crack on the surface of a material[3,11-15]. A recent extension of traditional ultrasound methods uses contact transducers combined with laser-based detection methods to image ultrasonic waves and material defects. With the emergence of laser ultrasound generation, detailed most notably by Scruby et. al[4,16], a fully non-contact ultrasound source is readily available. Experiments conducted using a scanning laser generated source of acoustic waves has also shown to provide crack detection and characterization capabilities[17,18].

In this effort, the benefits of using a combination of the above techniques, namely a complete non-contact, laser generation and interferometric detection of ultrasound was investigated. With this dual laser beam system, the ability to manipulate both the ultrasonic source and receiver is realized. In particular, the laser ultrasonic receiver can be positioned in the very near field, and actually within, the

laser ultrasonic source (an option not available using contact transducers). While early laser generation of surface-acoustic waves was focused primarily on the detection of far-field ultrasonic waveforms[4], it is this near-field ultrasonic interaction with surface-breaking cracks which is explored in this work. To develop a further understanding of the non-destructive laser generation of ultrasonic surface waves, a theoretical model is presented and compared with experimental waveforms measured in this region where the generation laser interacts with the surface of the material.

With the added flexibility of both laser ultrasound source and receiver manipulation, it is desirable to determine the optimal scanning technique for detecting and imaging surface-breaking cracks. Three basic configurations were explored in this work including; 1) scanning only the detection beam while leaving the source beam stationary, 2) scanning only the source beam while leaving the detection beam stationary, and 3) scanning both the source and detection beams at a fixed distance. Further, in a dual-beam scanning configuration, the effects of the laser beam source-receiver separation, as well as generation spotsize, were studied. Several data analysis procedures and noise reduction algorithms were also developed and implemented to enhance the crack imaging capabilities of the system.

CHAPTER II

BACKGROUND

Because ultrasonic inspection methods are such an important part of this thesis, a brief introduction to ultrasonic nondestructive evaluation (NDE) is provided. In particular, ultrasonic methods for detecting surface-breaking cracks are discussed. The laser generation and detection of ultrasound will then be covered. The non-destructive, thermoelastic generation of ultrasonic waves will be discussed in some detail, followed by a brief description of heterodyne interferometry, and its use in detecting ultrasound motion fields on a material surface. A conceptual description of the laser ultrasound crack imaging system developed for this thesis will then be provided. The similarities and differences of two related measurement techniques (near-field scanning interferometry[3,11,12,15] and scanning laser source[17,18]) will then be covered.

2.1 ULTRASONIC NDE

2.1.1 BASIC ULTRASONIC PRINCIPLES

In an elastic medium, energy propagates in the form of acoustic waves. Particle displacements due to this energy propagation generally involve three mutually orthogonal components, one longitudinal and two-transverse (Figure 2). Each component travels at its own velocity, dependant primarily on the properties of the material, and experiences different reflection and scattering phenomena at

boundaries. The interested reader is referred to excellent overviews of this topic by Cartz[1], Hull[2], and Thompson[6].

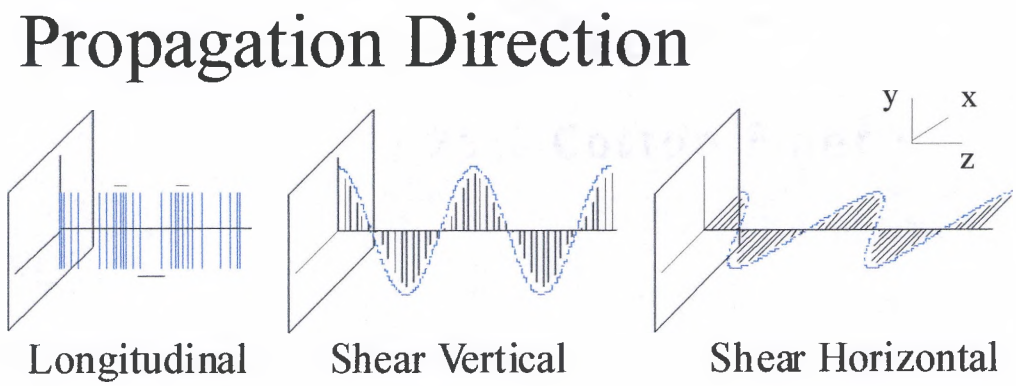

Figure 2 Schematic of longitudinal and transverse acoustic waves.

An important sub-class of acoustic waves which is used extensively in ultrasonic NDE inspections is referred to as surface-acoustic waves (SAW) or Rayleigh waves. Unlike waveforms which propagate through three-dimensions in the bulk of a material, Rayleigh waves are predominantly confined to the surface of a material. Due to this more concentrated energy, SAW are more easily generated and detected over larger distances, making them ideal for ultrasonic testing purposes[4]. In addition, because they propagate along the surface of a material, they are particularly suited for detecting surface-breaking cracks[4].

2.1.2 ULTRASONIC SCATTERING/FREE-BOUNDARY INTERACTION

The vast majority of ultrasonic NDE inspection methods detect and characterize cracks based on the reflection and/or scattering of ultrasonic waves from the crack site[4]. An incident elastic wave field, upon interacting with a material defect, is subjected to a wide variety of reflection and scattering processes including; simple reflection and transmission, diffraction, and mode conversion[4]. In a typical measurement, the position of a crack can be determined by the time-of-flight of the

transmitted and reflected/scattered wave, and the size of the crack can be determined by the amplitude of the received signal[3].

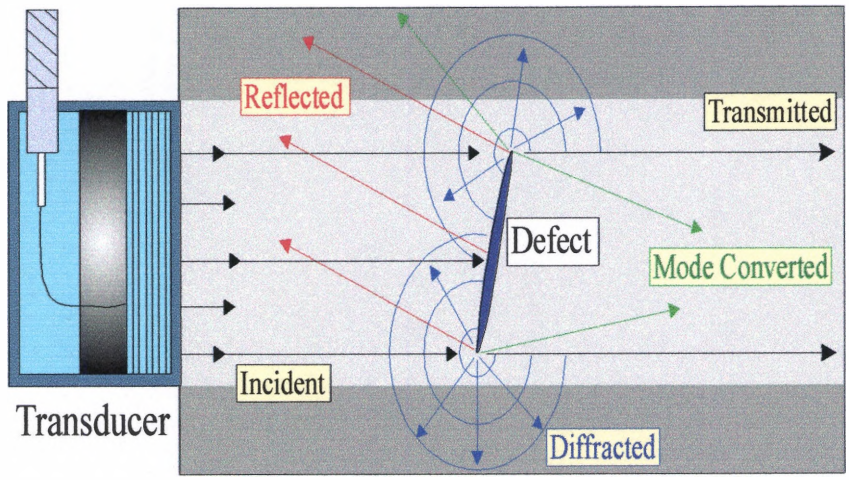

Figure 3 Diagram showing reflection and scattering processes occurring due to SAW's interacting with a surface-breaking crack.

Another interesting and important crack detection phenomenon that has recently been published[3,11] involves the local intensification of an elastic wave amplitude in the immediate vicinity of a crack site. The intensification levels have been reported to be between 200%-500% of the incident wave amplitude levels[3,11], which provides an opportunity to discriminate cracked regions on a material surface from undamaged regions based on measurements of the local displacement amplitude levels.

The physical description of this phenomenon has been attributed to free-boundary reflection processes, where motions near the crack are less restricted, compared with material in the bulk[3,12]. This results in larger amplitude motions near the crack site when an exciting elastic wave is incident on the defect. As depicted schematically in Figure 4a, a surface-breaking crack can be represented by the

uncoupling of the springs at the crack location. The two opposing crack faces represent free-boundaries which vibrate and reflect ultrasonic waves more energetically than the bulk material. When an incident ultrasonic pulse arrives at a free-boundary, the particles are free to move because of the lack of material (and resistive forces) further upstream. When the incoming ultrasonic pulse reaches the surface-breaking crack, a reflected pulse is created with the same sign and amplitude as the incident pulse (Figure 4b). The incident and reflected pulses thus reinforce each other, creating an antinode at the free boundary that has a nominal peak displacement that is twice the amplitude of either of the individual pulses (Figure 4b).

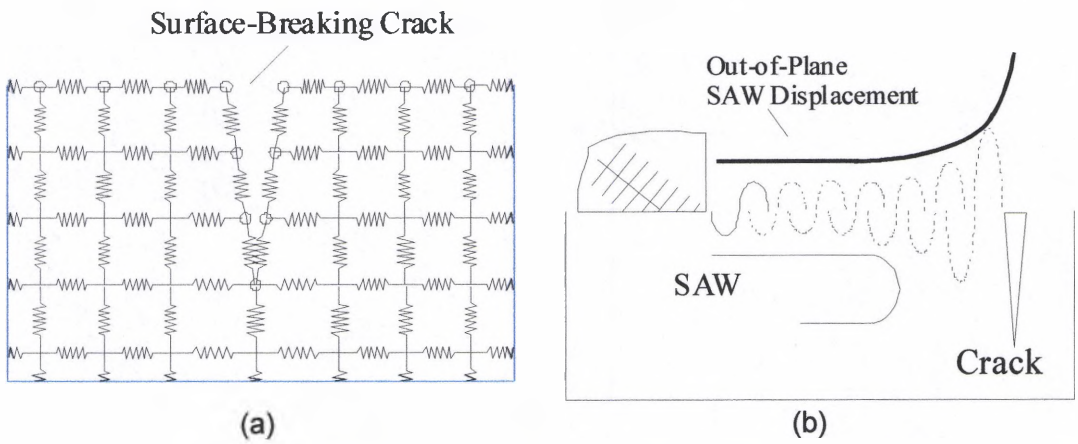

Figure 4 (a) Surface-breaking represented by the uncoupling of the springs at the crack location. (b) Superposition of incident and reflected SAW's contributing to near-field intensification at the surface crack location.

2.2 LASER GENERATED ULTRASONICS

Non-destructive laser generation of ultrasound is created through the absorption of energy from a laser pulse, mainly in the form of heat, at the surface of a material. Due to the relatively short pulse duration of commonly used generation lasers, thermal conductivity is minimal and this absorbed heat is confined to a small

volume near the surface of the material[4]. This small heated volume leads to a localized thermal expansion where, since it is bound within the material, creates strains which ultimately generate elastic waves[28]. While other mechanisms, such as ablation, can also lead to the propagation of elastic waves, permanent damage to the material occurs, thus the thermoelastic process is the desired mechanism for laser ultrasonic NDE.

2.2.1 SURFACE HEATING INDUCED BY A LASER PULSE

The thermoelastic mechanism, as its name suggests, is a result of rapid heating typically induced by the absorption of a laser pulse at the surface of a material. With this surface heating being the initial process of the thermoelastic mechanism, it is desirable to develop a basic theoretical understanding of this heating process. The development of a technique to approximate the surface temperature increase due to laser pulse absorption will also provide insurance that the experimental laser parameters used, specifically the laser power density, is well below a level where the material will reach its melting point and thus, no longer remain a non-destructive mechanism.

In the thermoelastic regime, interaction of a laser pulse with a material such as a metal can be treated as a heat flux located at the incident surface[27]. Early treatments of this transient surface heating, and the resultant thermoelastic stresses induced, were conducted in a one-dimensional form, most notably by R.M White[28].

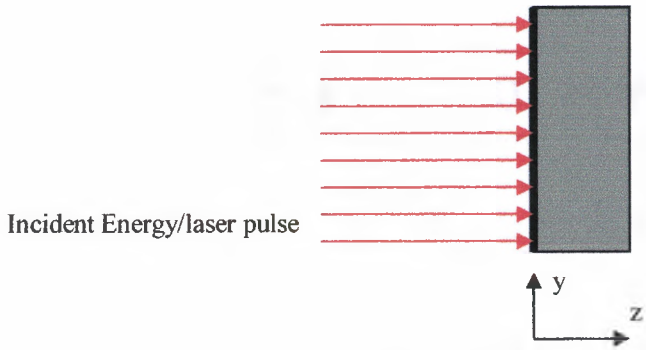

Figure 5 Uniform heating at the surface of a half space.

To determine the temperature change of the material the classical heat equation is typically used[4,28]. Thus

$$\nabla^2 T - \frac{1}{k}\frac{\partial T}{\partial t} = -\frac{A}{K} \qquad \text{Eq. 1}$$

where $T(x,y,z,t)$ is the temperature distribution, $A(x,y,z,t)$ is the heat source, k is the thermal diffusivity, and K is the thermal conductivity. The boundary conditions are such that $T(x,y,z,0)=0$, no heat flux crosses the incident plane (z=0), and the temperature must approach zero as x approaches infinity[4]. For the one-dimensional situation depicted by Figure 5, assuming the laser (heat source) is turned on instantaneously at t=0, with the absorbed laser flux density being I_o, the solution to this equation is well known[4,17,29] and is represented by[4]

$$T_H(z,t) = \frac{I_o}{K\sqrt{\pi}}\left[2\sqrt{\kappa t}\exp\left(-\frac{1}{4}\frac{z^2}{\kappa t}\right) + z\sqrt{\pi}\,erf\left(\frac{1}{2}\frac{z}{\sqrt{\kappa t}}\right) - z\sqrt{\pi}\right] \qquad \text{Eq. 2}$$

Due to the initial temporal properties of the heat source, namely, the instantaneous application of uniform heating at t=0, a simple procedure can be used to obtain an impulse response of a material in the context of the previous situation. Since the heating of the above solution was applied in a manner which can be

described by a Heaviside $u(t)$ time dependence, and since the relation of the $u(t)$ function to the Dirac delta function is simply

$$\frac{d}{dt}u(t) = \delta(t) \qquad \text{Eq. 3}$$

the response of a half-space due to heat applied with an impulse time dependence can be written as

$$T_D(z,t) = \frac{\partial}{\partial t}T_H(z,t) = \frac{I_o\kappa}{K\sqrt{\pi\kappa t}}\exp\left(-\frac{1}{4}\frac{z^2}{\kappa t}\right) \qquad \text{Eq. 4}$$

Using this impulse function, the temperature response can now be found for any pulse or heating cycle simply by

$$T(z,t) = q(t) * T_D(z,t) = \int_0^t q(\tau)T_D(z,t-\tau)d\tau \qquad \text{Eq. 5}$$

where q(t) is the time dependence of the laser pulse. For example, the temperature distribution due to a square pulse with a 100ns width (Figure 6), can be seen in Figure 9 for three different depths into an aluminum sample. The parameters used in this case are $I_o = 1.4x10^9 Wm^{-2}$, $K = 240\text{Wm}^{-1}\text{K}^{-1}$, and $\kappa = 1.0\text{x}10^{-4}\text{m}^2\text{s}^{-1}$.

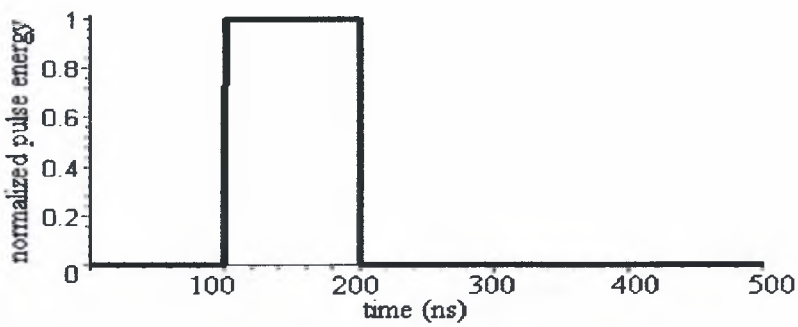

Figure 6 Square pulse with 100ns width used for temperature model.

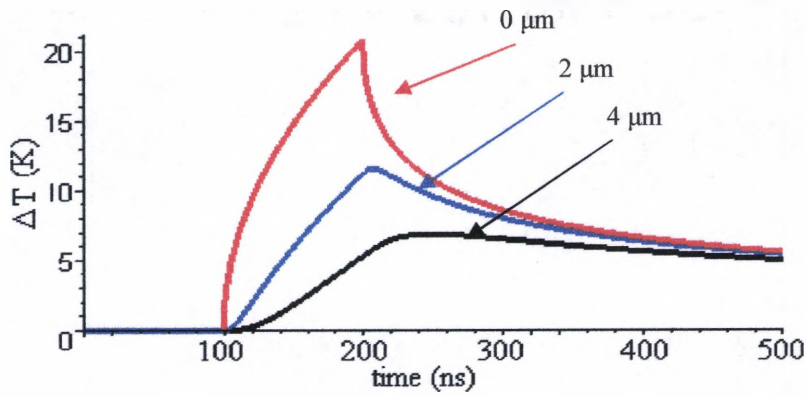

Figure 7 Temperature response of Aluminum due to 100ns square pulse at 0,2, and 4μm depths into the material (z-direction).

Figure 7 shows that the temperature drops off appreciably over a depth of several microns. In many cases, due to this small depth of penetration, the heat source is simply considered as being confined to the surface.

Using the same technique, the effect of using a more realistic, Gaussian, pulse can be compared to the square pulse time dependence used previously. These pulses, a 100ns square pulse and a Gaussian pulse with FWHM=100ns, can be seen in Figure 8 and the temperature rise of the surface (z=0) due to these pulses can be seen in Figure 9. The parameters used in these plots are the same as used previously.

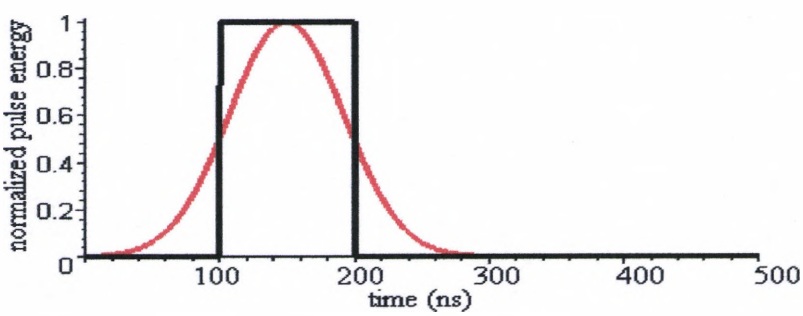

Figure 8 A 100ns square pulse and Guassian pulse with FWHM=100ns.

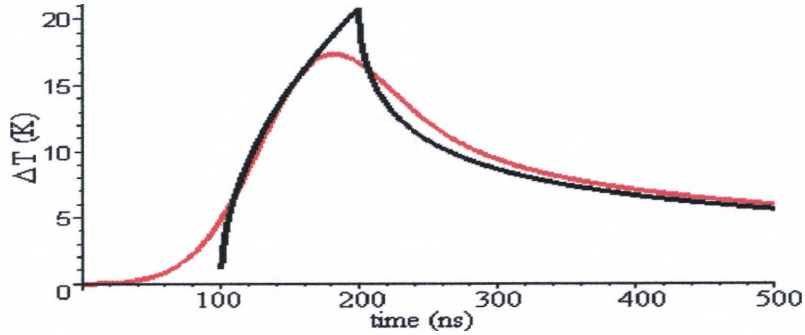

Figure 9 Temperature rise due to the pulses of Figure 8.

Figure 9 shows the effect of using a Guassian pulse, compared to a square pulse of similar width, is a slight reduction in peak magnitude as well as a small broadening in time of the temperature distribution.

In applications of laser ultrasonics, the heat source (laser) is typically applied to the material in the form of a series of pulses, incident at some repetition rate. It is therefore important to examine the heat response due to a series of pulses. In the following example, three distinct heating cycles are analyzed using different on/off ratios which is denoted by Ω. In all cases the magnitudes of the heating pulses are set to 1/ Ω. These transient heating cycles can be seen, plotted using arbitrary magnitude and time parameters, in Figure 10.

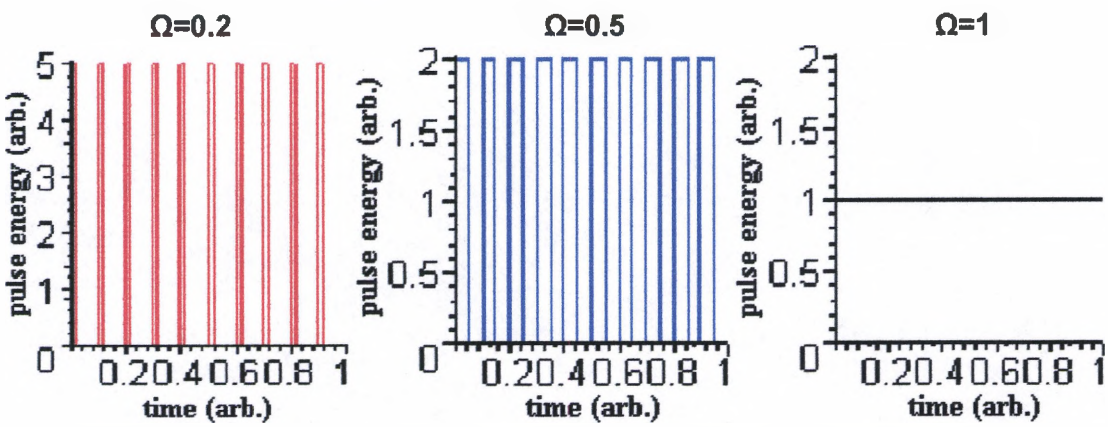

Figure 10 Transient heating cycles with various on/off ratios and magnitudes.

Using equation 5, and setting arbitrary parameters I_o=K=κ=1, the surface temperature response (z=0) can be seen in Figure 11 for these heating cycles. The colors shown in Figure 11 represent the cases of the same color in Figure 10.

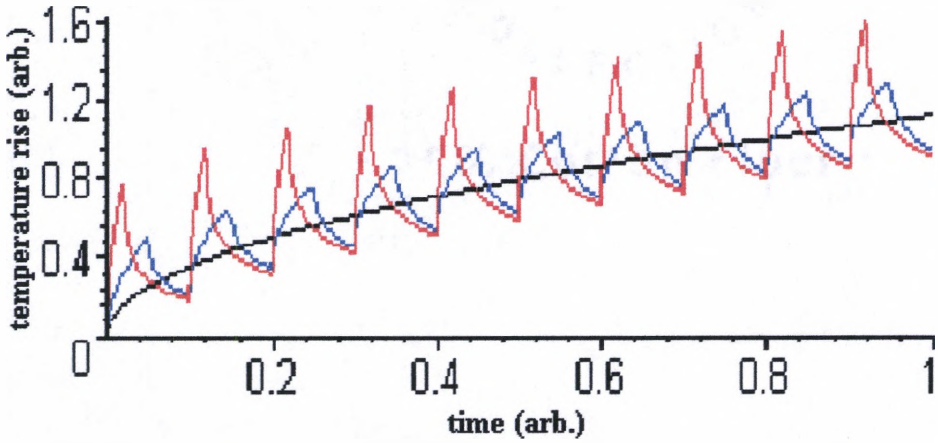

Figure 11 Surface temperature response for the transient heating cases shown in Figure 10.

In Figure 11, for both cases of the pulsed heating cycles (red and blue lines), it is noticed that the long decay tail of the temperature response does not have time to decay appreciably before the arrival of the next pulse. It can also be seen that all three heating cycles produce the same average temperature response in the material. This is due to all three cases satisfying

$$\int_0^T q_1(t)dt = \int_0^T q_2(t)dt = \int_o^T q_3(t)dt \qquad \text{Eq. 6}$$

where T is the time period of the entire series of pulses. It is therefore the entire heat absorbed over the full series of pulses which determines the average response of the system. This relationship becomes important, in aspects of non-destructive evaluation, as the use of successive pulses at high repetition rates may, even at low powers, induce a temperature response which eventually exceeds the damage

threshold if the entire heating cycle is applied for a long period of time. For Aluminum, the melting point is 933K[4] however, to ensure non-destructive testing, following the experimental results of previous authors[4] , a very modest temperature rise of less then 60 K, where no material damage has been observed[4], will be sought.

The temperature response examples shown in Figure 11, due to the heating cycles of Figure 10, particularly the examples using the heat applied in a series of pulses, were simulated using a repetition rate in which the temperature rise does not decay significantly before the arrival of the next pulse. To observe the change in the response due to various repetition rates, the pulse rate can be changed while maintaining a constant pulse width and amplitude. The heating cycles and temperature responses corresponding to these cycles can be seen in Figure 12 and Figure 13, respectively.

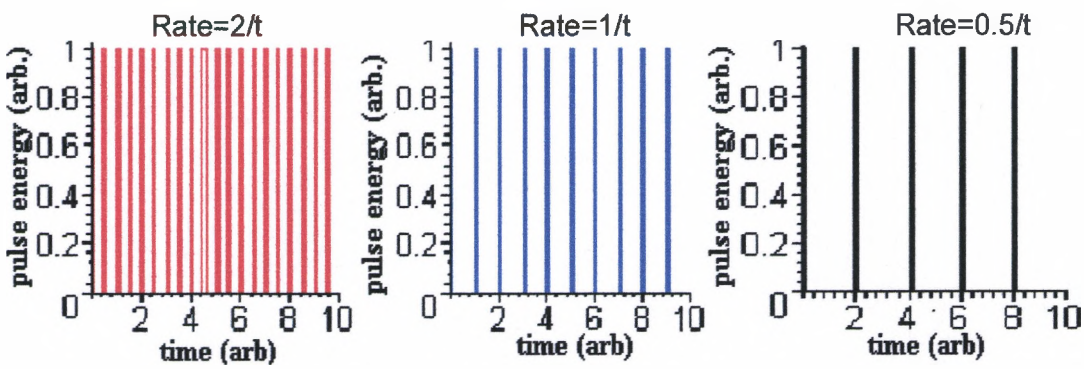

Figure 12 Transient heating cycles with various repetition rates.

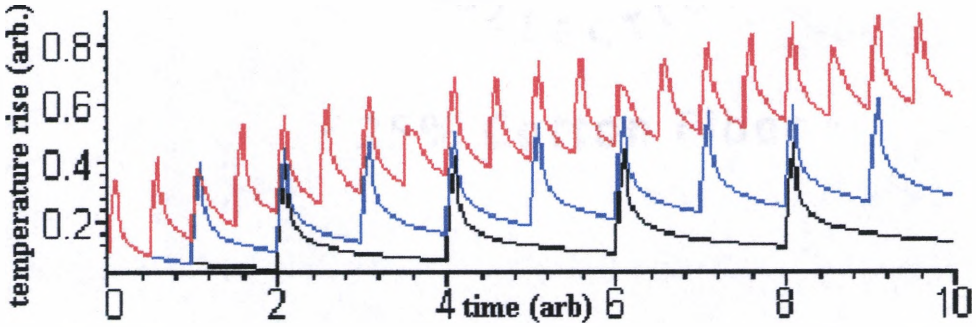

Figure 13 Surface temperature response for the transient heating cases shown in Figure 12.

Figure 13 indicates that the variation in the repetition rate creates a shift in the average temperature rise at the surface of the material. Specifically, the smaller repetition rate produces a slower average temperature rise due to the series of pulses. This is a logical result as it is obvious from Figure 13 that the response to each pulse, in the smaller repetition rate, is allowed to decay before the arrival of subsequent pulses.

Expanding on the behavior portrayed in Figure 13, an approximation of the temperature rise after any number of pulses, given the time dependence (pulse width, repetition rate), can be found. Assuming the temperature response is $T_0(z,t)$ due to a single pulse $q_0(t)$ which starts at time t_o, an identical second pulse $q_1(t)$ which occurs at time t_1 (Figure 14), has a temperature response which can be approximated as

$$T_1(z,t) \approx T_o(z,t_1) + T_1(z,t) \qquad \text{Eq. 6}$$

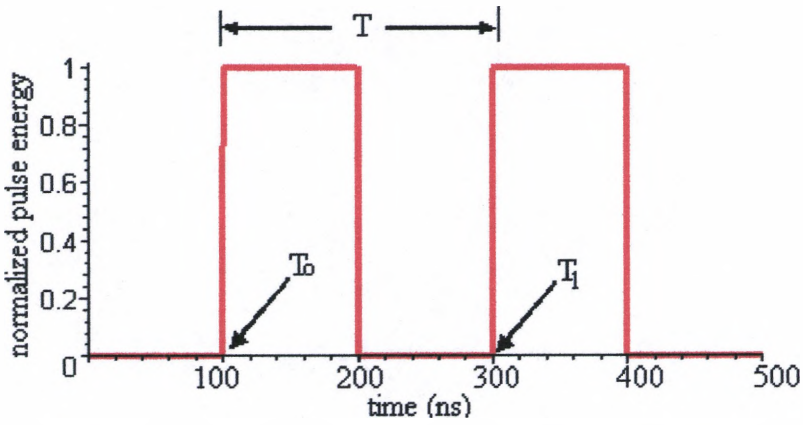

Figure 14 Diagram showing consecutive pulses, their starting times, and the separation.

Thus, from equation 6, the temperature rise due to the second pulse is approximated by simply considering only the single pulse with the addition of a DC term corresponding to the temperature of the material from the first pulse at the time when this second pulse occurs. It should be noted that this approximation will be most accurate when the slope of the decay of the previous pulse is smallest (thus when the pulse separation is large).

Using this approximation, the temperature rise due to n identical pulses separated by time T can be written simply as

$$T_n(z,t) = (n-1)T(z,t+T) + T(z,t) \qquad \text{Eq. 7}$$

where $T(z,t)$ is the response due to a single pulse. The validity of this approximation can be seen using a series of pulses (Figure 15) and the comparison between the actual and approximated temperature response of the nth pulse (Figure 16).

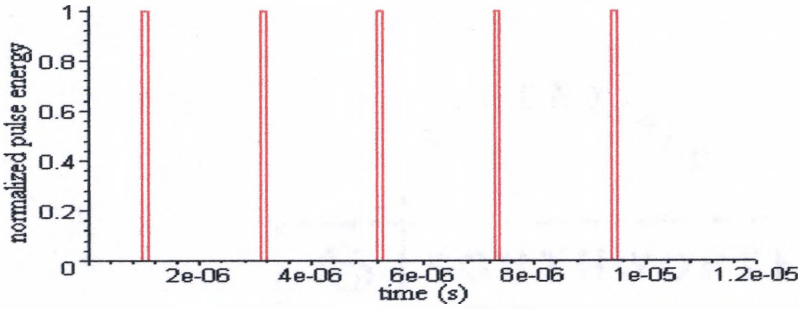

Figure 15 Series of 5 identical pulses.

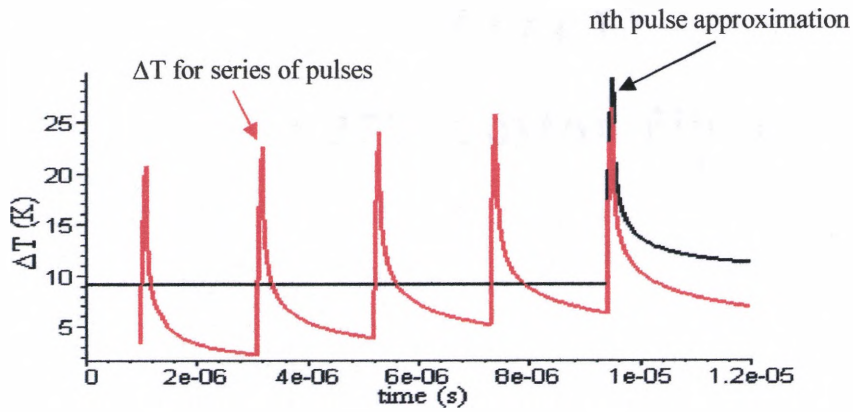

Figure 16 Temperature rise due to the pulses of Figure 15 (red line) and approximation of the nth pulse (black line).

The rationale for using this quick approximation for a series of pulses is to ensure the temperature rise of the material, for the purpose of non-destructive evaluation, does not exceed the melting point of the material. As mentioned previously, the melting point of Aluminum is 933K[4] and experimental observations have shown no damage with a temperature rise of 60K[4]. If the heating source is a laser operating with a pulse length of 100ns, an energy of 2.5mJ/pulse, and a repetition rate of 20 Hz then, using equation 7, the temperature rise after even 1000 pulses is still only approximately 35 K (Figure 17), well below the temperature where any damage would occur.

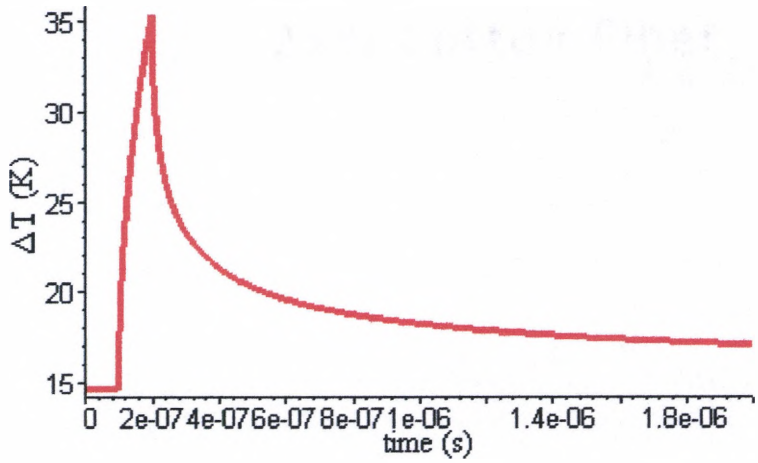

Figure 17 Temperature rise due to the 1000th pulse using a repetition rate of 20Hz, a pulse length of 100ns, and a pulse energy of 2.5mJ/pulse.

2.2.2 THERMOELASTIC EXPANSION/LASER INDUCED STRESSES

In the previous section the effects of surface heating due to the absorption of a laser pulse was discussed. The temperature rise of the heated material leads to a thermal expansion of this affected region[4]. Due to the heated portion being confined within a larger, unaffected region, this localized material expansion creates stress and strain fields within the material[4,28]. These stress and strain fields enable the propagation of elastic waves within the material.[4,28] The transition from the heating of a material into the propagation of elastic waves, via thermoelastic expansion will now be considered. Similar to the previous section for surface heating, a basic theoretical treatment of these laser induced stress/strain fields will allow for approximations to be made, based upon laser parameters, to ensure a non-destructive mechanism of elastic wave generation.

The localized temperature rise, induced by absorption of a laser pulse within a small region close to the surface of a material, produces temperature gradients which, due to thermal expansion, create strains in the material[28]. Depending on the properties of the surface heating (laser irradiation), the temperature gradients and

thus strain in the material may be, in the half-space situations depicted in Figure 18, one-dimensional or two dimensional. For uniform irradiation at the surface (z=0) of a half-space the strain is only in the z-direction (Figure 18a), while for a non-uniform irradiation temperature gradients are multidirectional leading to strains in both z and y[4,28] (Figure 18b).

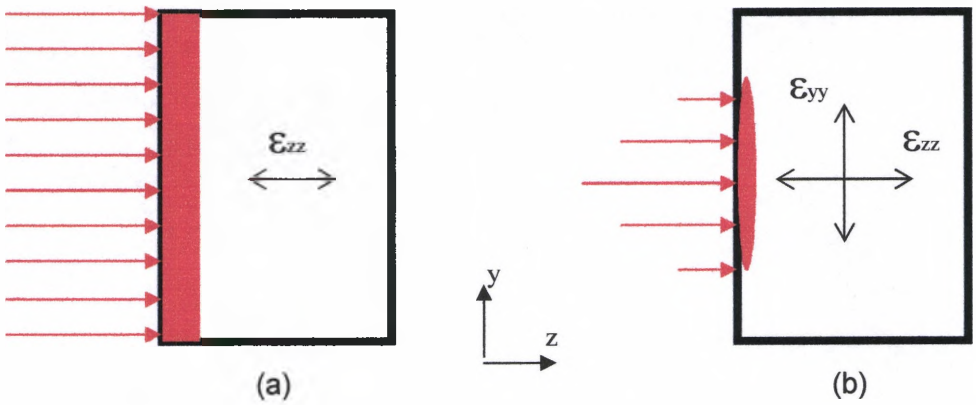

Figure 18 (a) Uniform irradiation leading to one-dimensional strains. (b) Non-uniform irradiation resulting in multidimensional strains in a half-space.

The one-dimensional treatment of this problem was first formulated by R. M. White[28]. Using the uniform irradiation depicted by Figure 18a, assuming the surface is originally stress free, the strain ε_{zz} can be expressed as[4,28]

$$\varepsilon_{zz} = \alpha T(z,t) \qquad \text{Eq. 8}$$

where α is the coefficient of linear thermal expansion and $T(z,t)$ is the temperature rise due to the absorption of the incident laser pulse.

Scruby et.al[4,16], presented a more realistic, three-dimensional treatment by considering the heated region as a center of expansion confined to a small volume of material V. If this center of expansion is within the bulk of the sample, this expanding volume can be treated as the insertion of extra volume ΔV into the material[4,16]. The strain in all three dimensions are then represented by[4,16]

$$\varepsilon_{xx} = \varepsilon_{yy} = \varepsilon_{zz} = \frac{1}{3}\frac{\Delta V}{V} = \alpha T(x, y, z, t) \qquad \text{Eq. 9}$$

and the local stress field produced can then be written as[4,16]

$$\sigma_{xx} = \sigma_{yy} = \sigma_{zz} = B\frac{\Delta V}{V} \qquad \text{Eq. 10}$$

where B is the bulk modulus. The expansion can thus be treated as the appearance of three mutually orthogonal "force dipoles" with strength equal to[4,16]

$$D_{xx} = D_{yy} = D_{zz} = B\Delta V \qquad \text{Eq. 11}$$

In most cases of an incident Q-switched laser pulse, the time period of absorption (e.g. 10-100ns) is small enough such that thermal conduction into the bulk of the material is on the order of μm[4] and, assuming the spatial diameter of the laser beam at the surface is on the order of mm's, many times larger than the several μm depth, the source of expansion can be considered as a thin disk at the surface[30]. A diagram showing this material expansion and the equivalent force dipoles is shown in Figure 19.

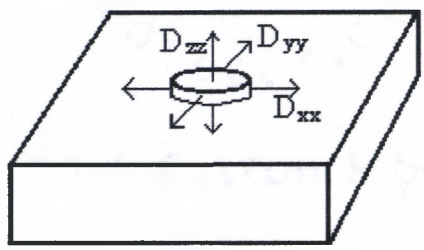

Figure 19 Center of expansion for source with finite thickness and resulting force dipoles.

If the thickness (depth) of the localized expanding source is considered to be negligible, and all energy is assumed to be confined to the surface (z=0), the boundary conditions, which state only stresses parallel to the surface exist[4,30] (ie.

$\sigma_{zz}, \sigma_{zx}, \sigma_{zy} = 0$), lead to the strength of the dipole D_{zz} also becoming inconsequential.

As was the case with the surface heating, it is helpful to estimate the stress induced by an incident laser pulse of finite time duration. Using equations 9 and 10, the stress can be written in terms of the temperature

$$\sigma = 3B\alpha T \qquad \text{Eq. 12}$$

Using the results of the previous section for a laser pulse width of 100ns and a laser power density of $1.4x10^{9}\,Wm^{-2}$, and using parameters for Aluminum[4], B=75.5 GPa and $\alpha = 2.31x10^{-5}\,K^{-1}$, the maximum stress due to the complete absorption of this pulse is on the order of $10^{8}\,Pa$, which is of the same order as the yield strength[4]. It thus becomes evident that the possibility of permanent surface damage can be achieved by the absorption of relatively low laser pulse energies using Q-switched lasers. Experimentally, surface damage such as melting, vaporization, plasma formation, and material ablation, has been shown to occur for laser power densities above $10^{7}\,Wcm^{-2}$ in Aluminum[4]. Therefore, considering the laser parameters which have been previously used, namely 100ns pulse width, 2.5mJ per pulse, and assuming a laser beam diameter of 3mm, the incident laser power density is approximately $3.5x10^{5}\,Wcm^{-2}$. Considering the reflectivity of the material is approximately 0.9, the absorbed power density is reduced again by an order of magnitude to $3.5x10^{4}\,Wcm^{-2}$. Thus using these parameters should ensure SAW generation in the non-destructive thermoelastic regime.

2.2.3 POINT-SOURCE MODEL FOR SURFACE DISPLACEMENT/SURFACE CENTER OF EXPANSION (SCOE)

In the previous sections, a basic theoretical foundation has been given for both the surface heating and the thermoelastic stress and strain due to absorption of

a laser pulse at the surface of a material. The transition from the stress and strain to actual elastic waveforms, in this case surface acoustic waves (SAW), requires a more elaborate derivation, however. While many previous laser generated ultrasound models and techniques have worked reasonably well under far-field approximations, for the purpose of this investigation it becomes necessary to understand the thermal energy and motion field properties of the material very near the laser generation source. This is because the use of a dual-laser measurement technique provides a unique opportunity to explore and understand the potential for crack detection using superimposed laser generation and detection beams (in contrast to previous work which has utilized separated beam measurement systems).

The first step in the development of theoretical surface waveform model, is to briefly present a method used by L.R.F. Rose[31] who rigorously derived an expression for surface displacement waveforms from a thermoelastic point-source. Rose[31] set out to systematically derive the point-source representation for a surface center of expansion (SCOE) model for laser generated ultrasonics originally suggested, based on intuitive arguments, by Scruby et. al.[16]. The basic approach was to represent a volume source of expansion as a point source expansion of material, which can later be integrated over a volume. The entire derivation is rather involved and will only be briefly outlined in the following section.

Rose began his derivation using a representation theorem for a point force in a half-space where, the displacement $u_n (n = 1,2,3)$ can be written as[32]

$$u_n(x,t) = \int_V c_{ijkl}\varepsilon_{kl}(\xi,t) * \frac{\partial G_{ni}}{\partial \xi_j}(x;\xi,t)\,dV(\xi) \qquad \text{Eq. 13}$$

where c_{ijkl} are the elastic stiffness coefficients, ε_{kl} is the (stress-free) strain representing the source, and $G_{ni}(x;\xi,t)$ is the Green function for the displacement at x and t, due to an impulsive point-force parallel to the x_i axis at point ξ and time t[31]. For simplification, in the case of an isotropic material, the above can be rewritten as[31]

$$u(x,t) = M(t) * g(x,0,t) \qquad \text{Eq. 14}$$

where, since the strain is related to the induced temperature rise by $\varepsilon = \alpha T$ [31],

$$M(t) = E(1-\nu)^{-1}\alpha \int_V T(\xi,t)dV(\xi) \qquad \text{Eq. 15}$$

where E is Young's modulus and ν is the Poisson ratio. In equation 14, the Green function is now represented by[31]

$$g_n(x,\xi,t) = \frac{\partial}{\partial \xi_i} G_{ni}(x,\xi,t) \qquad \text{Eq. 16}$$

Further, since the temperature rise can be written in terms of the energy absorbed from an incident laser pulse, Rose simplified the equation to[31]

$$u(x,t) = \Gamma q(t) * g^H(x,0,t) \qquad \text{Eq. 17}$$

where q(t) is the normalized laser pulse shape and[31]

$$\Gamma = E\alpha\kappa Q[K(1-2\nu)]^{-1} \qquad \text{Eq. 18}$$

where κ is the thermal diffusivity, K is the thermal conductivity, and Q is the total heat input due to the laser pulse. In equation 17, the superscript H represents the Heaviside Green function in lieu of the delta function. The determination of g^H is rather complex thus only a brief explanation of the method used will be given here.

In the case of a laser pulse incident normal to the surface of a half-space defined by z=0 (Figure 20), the resultant elastic field will be axially symmetric to the optic axis[31], and thus the equations of motion can be derived in terms of two

potentials $\phi(r,z,t)$ and $\psi(r,z,t)$[5,31]. The potentials can be related to the displacements of interest, surface displacements (z=0), by the relation[31]

$$u_r = \frac{\partial \phi}{\partial r} + \frac{\partial^2 \psi}{\partial r \partial z} \qquad \text{Eq. 19}$$

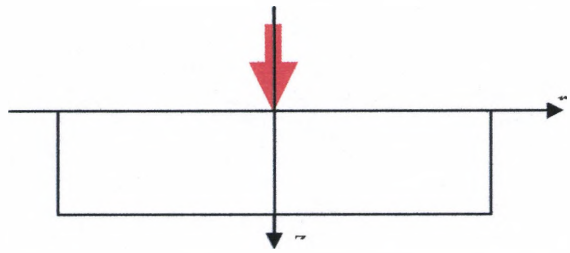

Figure 20 Diagram showing laser pulse incident on surface of half-space.

Assuming the source point ξ, for now, lies somewhere within the defined half-space, at the point r=0 and z=d, the equations specifying $g^H(x,\xi,t)$ can be written as[31]

$$\frac{\partial^2 \phi}{\partial z^2} + \frac{1}{r}\frac{\partial}{\partial r}\left(r\frac{\partial \phi}{\partial r}\right) - \frac{1}{c_L^2}\frac{\partial^2 \phi}{\partial t^2} = \frac{\Lambda}{2r}\delta(r)\delta(z-d)H(t) \qquad \text{Eq. 20}$$

$$\frac{\partial^2 \psi}{\partial z^2} + \frac{1}{r}\frac{\partial}{\partial r}\left(r\frac{\partial \psi}{\partial r}\right) - \frac{1}{c_T^2}\frac{\partial^2 \psi}{\partial t^2} = 0 \qquad \text{Eq. 21}$$

with the conditions of an unconstrained surface[31]

$$\sigma_{zz} = \sigma_{zr} = 0, \quad \text{on } z = 0, \quad t \geq 0 \qquad \text{Eq. 22}$$

and[31]

$$\phi = \frac{\partial \phi}{\partial t} = \psi = \frac{\partial \psi}{\partial t} = 0, \quad \text{for } t < 0 \qquad \text{Eq. 23}$$

where c_L and c_T are the longitudinal and transverse wave speeds, respectively.

To derive the formal solution for the above equations, a double Hankel-Laplace transform is utilized followed by taking the limit $d \to 0$ to represent the

surface center of expansion SCOE[31]. The inversion procedure is accomplished using the Cagnaird-de Hoop technique[31,32]. For points on the surface (z=0), the result derived by Rose is[31]

$$u_z(r,0,t) = -\frac{1}{8c_T^2}\Lambda\Gamma Sq(t) * \frac{H(t - s_R r)}{\left(t^2 - s_R^2 r^2\right)^{1/2}} \qquad \text{Eq. 24}$$

where[31]

$$S = \frac{(1-\nu)(2-\chi)^3}{\left[\chi^2 - \nu\chi^2(2-\chi) + \chi(2-\chi)\right]} \qquad \text{Eq. 25}$$

and[31]

$$\chi = c_R^2 / c_T^2 \qquad \text{Eq. 26}$$

The quantity c_R is the Rayleigh wave speed and $s_R = c_R^{-1}$.

To determine the Green's function for surface displacement, as indicated by Scala and Doyle[33] it is appropriate to use the time derivative of Rose's derivation (equation 24) thus, the Green's function can be expressed as[34]

$$g(r,t) = \frac{2M}{\pi\mu V_L^2}\frac{\partial}{\partial t}\left[\frac{H(t - s_R r)}{\left(t^2 - s_R^2 r^2\right)^{1/2}}\right] \qquad \text{Eq. 27}$$

where $V_L = \sqrt{(\lambda + 2\mu)/\rho}$, λ and μ being the Lame constants and ρ the material density. The factor M in equation 27 is related to S in equation 25 by S=16M. This expression, given by equation 27, represents the approximate thermoelastic surface displacement due to the absorption of an impulsive laser pulse, at an infinitesimally thick ring of radius r. To represent the more realistic situation of a finite duration laser pulse and an extended thermoelastic source, this equation can be integrated spatially and convoluted with a laser pulse of finite temporal width[35].

2.2.4 NUMERICAL MODELING OF NEAR-FIELD THERMOELASTIC SURFACE DISPLACEMENT

With the establishment of the Green's function for a thermoelastically induced surface displacement, discussed in the previous section, an attempt to model the near-field thermoelastic source can now be carried out. Numerical evaluation of this derived function is, however, not easily implemented as the occurrence of multiple singularities complicates the modeling effort. A method used to simplify these complications has been derived by previous authors[35] for the modeling of a laser source expanded, using cylindrical lenses, into a line on the surface of a material. Using this method of simplification for a laser line source, a numerical model for a circular, Gaussian laser source has been developed.

Having previously shown the Green's function for a SCOE point source to be[34]

$$g(r,t)=\frac{2M}{\pi\mu V_L^2}\frac{\partial}{\partial t}\left[\frac{H(t-s_R r)}{\left(t^2-s_R^2 r^2\right)^{1/2}}\right] \qquad \text{Eq. 28}$$

it becomes desirable to attempt to model the surface displacement due to an extended source subject to a laser pulse of finite width. Evaluating the derivative in equation 28, the Green's function can be expressed as

$$g(r,t)=\frac{2M}{\pi\mu V_L^2}\left[\frac{\delta(t-s_R r)}{\left(t^2-s_R^2 r^2\right)^{1/2}}-\frac{H(t-s_R r)t}{\left(t^2-s_R^2 r^2\right)^{3/2}}\right] \qquad \text{Eq. 29}$$

which shows the presence of multiple singularities at $t=s_R r$. These singularities complicate the task of accurately modeling surface displacements and thus, further analytical simplification is needed to ease the computing task.

A method of analytical simplification has been derived by Royer and Chenu[35] for the purpose of modeling a laser line source on the surface of a half-space. In this case, the extended line source is considered as a superposition of point sources in

the y-direction extending from –d to +d (Figure 21). The observation point is perpendicular to the line source (x-axis), and the propagation distance $r = \sqrt{y^2 + x^2}$

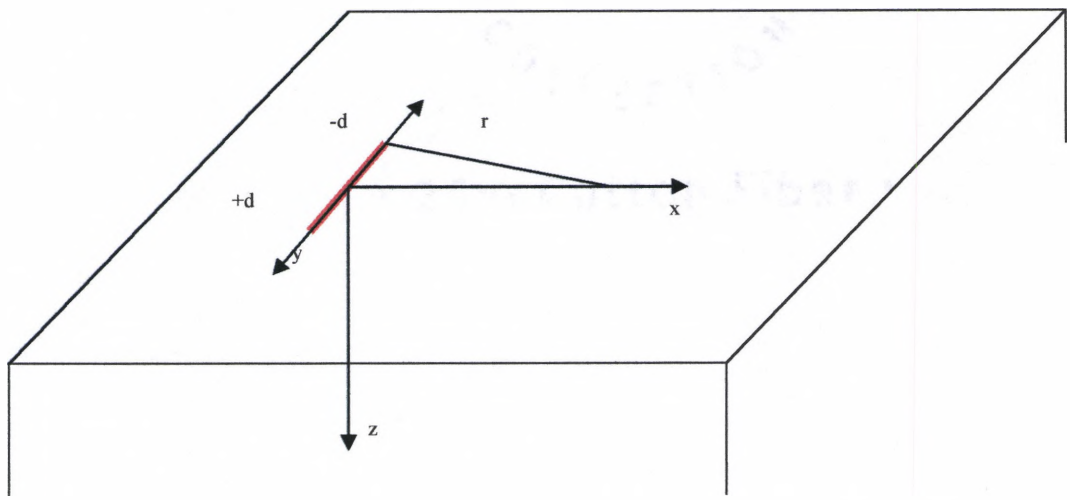

Figure 21: Geometry of laser line source on half-space according to derivation of Royer + Chenu[35].

For the calculation of the surface displacement at the observation point x, the time convolution of the Green function with the laser pulse temporal profile is[35]

$$u(x,t) = \frac{2\Gamma M}{\pi \mu V_L^2} q(t) * \frac{\partial f}{\partial t} \qquad \text{Eq. 30}$$

where $\Gamma = (3\lambda + 2\mu)\frac{\alpha}{\rho C}Q$, C being the specific heat and Q the total energy absorbed. The function f(x,t) is the summation of point sources along the line using the SCOE function derived by Rose, and is written as[35]

$$f(x,t) = \int_{-d}^{d} w(y) \frac{H(t - s_R r)}{\left(t^2 - s_R^2 r^2\right)^{1/2}} \qquad \text{Eq. 31}$$

where w(y) is the light intensity distribution along the line source[35].

Using this formulation Royer and Chenu showed that this function can be simplified to the form[35]

$$\frac{\partial f}{\partial t} = \frac{\sqrt{\pi}}{s_R a}\left[\delta(t - s_R x) + \frac{tL(\xi)}{s_R^2 a^2} H(t - s_R x)\right] \qquad \text{Eq. 32}$$

where a is the half-width of the Gaussian intensity profile, the function $L(\xi)$ is given by[35]

$$L(\xi) = [I_1(\xi) - I_0(\xi)]e^{-\xi} \qquad \text{Eq. 33}$$

where $I_1(\xi)$ and $I_0(\xi)$ are modified Bessel functions and the quantity ξ is given by[35]

$$\xi(t) = \frac{t^2 - s_R^2 x^2}{2 s_R^2 a^2} \qquad \text{Eq. 34}$$

The derived equation for the line source (equation 30) provides a computationally easier form than that of the point source expression (equation 28) shown earlier, which is complicated by the presence of multiple singularities. Using this expression for the line source, a Gaussian generation spot can now be analyzed.

Utilizing the simplified equation for the line source (equation 30), a Gaussian spot can be represented by a series of Gaussian line sources weighted and distributed along the x-axis (Figure 22). The equation for the surface displacement in this case is written as

$$u(x,t) = \frac{2\Gamma M}{\pi \mu V_L^2} q(t) * \int_{-a}^{+a} w(X) \frac{\partial}{\partial t} f(x - X, t)\, dX \qquad \text{Eq. 35}$$

where the weighting function $w(X)$ is represented by

$$w(X) = \frac{1}{a\sqrt{\pi}} \exp\left(\frac{-X^2}{a^2}\right) \qquad \text{Eq. 36}$$

where a is again the half-width of the Gaussian light intensity distribution.

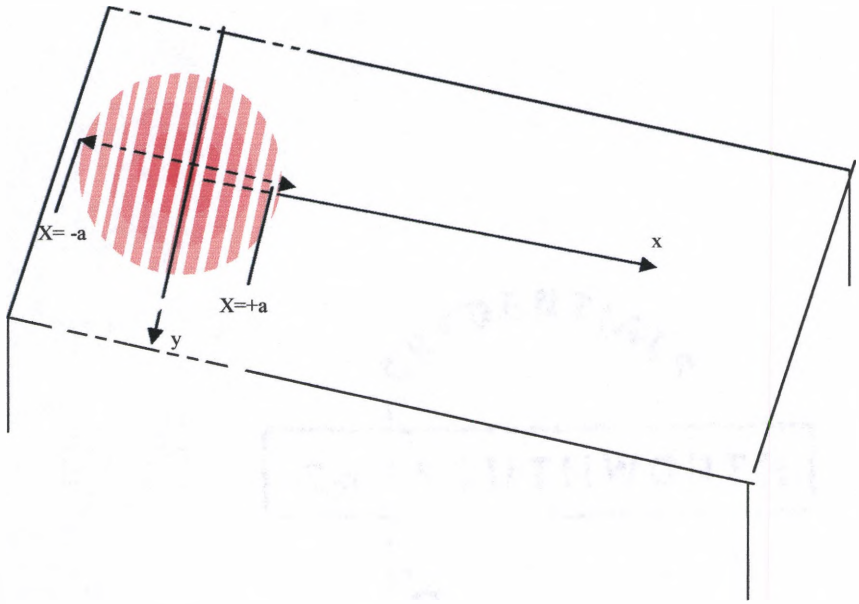

Figure 22 Geometry for Gaussian spot represented by a series of shifted and weighted line sources.

To investigate the behavior of this model, a numerical program (Appendix A) was developed to evaluate equation 35. The primary features of this equation are evident in the expression involving the time derivative of $f(x,t)$. This expression, given in equation 32, contains two essential parts; a delta function and a Heaviside component which includes the $L(\xi)$ function, given by equation 33. Observation of the Dirac and Heaviside components shows both are non-zero only, and starting at, $t = s_R x$, respectively. To observe the contributions of these parts to the overall displacement waveforms, equation 32 can be separated into two distinct functions, denoted $D(x,t)$ and $H(x,t)$, to represent the Delta function and Heaviside function components. The separated functions can thus be written as

$$\frac{\partial D}{\partial t} = \frac{\sqrt{\pi}}{s_R a}\left[\delta\left(t - s_R x\right)\right] \qquad \text{Eq. 37}$$

$$\frac{\partial H}{\partial t} = \frac{\sqrt{\pi}}{s_R a}\left[\frac{tL(\xi)}{s_R^2 a^2}\hat{H}\left(t - s_R x\right)\right] \qquad \text{Eq. 38}$$

where the Heaviside function itself is now denoted as $\hat{H}$ in order to distinguish between the step function and the entire $H(x,t)$ component.

Equations 37 and 38 can then be inserted into Equation 35 as follows,

$$u(x,t) = \frac{2\Gamma M}{\pi\mu V_L^2} q(t) * \int_{-a}^{+a} w(X)\frac{\partial}{\partial t}\left[D\left(t - s_R\left[x - X\right]\right) \text{ or } H\left(t - s_R\left[x - X\right]\right)\right]dX \qquad \text{Eq. 39}$$

For a simple analysis of the displacement contributions, numerical evaluations using arbitrary parameters were conducted. In these simulations, q(t) was modeled as a normalized Gaussian function. For numerical purposes, the delta function is also represented by a normalized Gaussian function of finite width. The results of several simulations, using variations in the spatial observation point x, and plotted vs. time can be seen in Figure 23. These figures show the waveform components separately in Figure 23a, and combined Figure 23b, at various distance from the source center given as fractions of the source radius a.

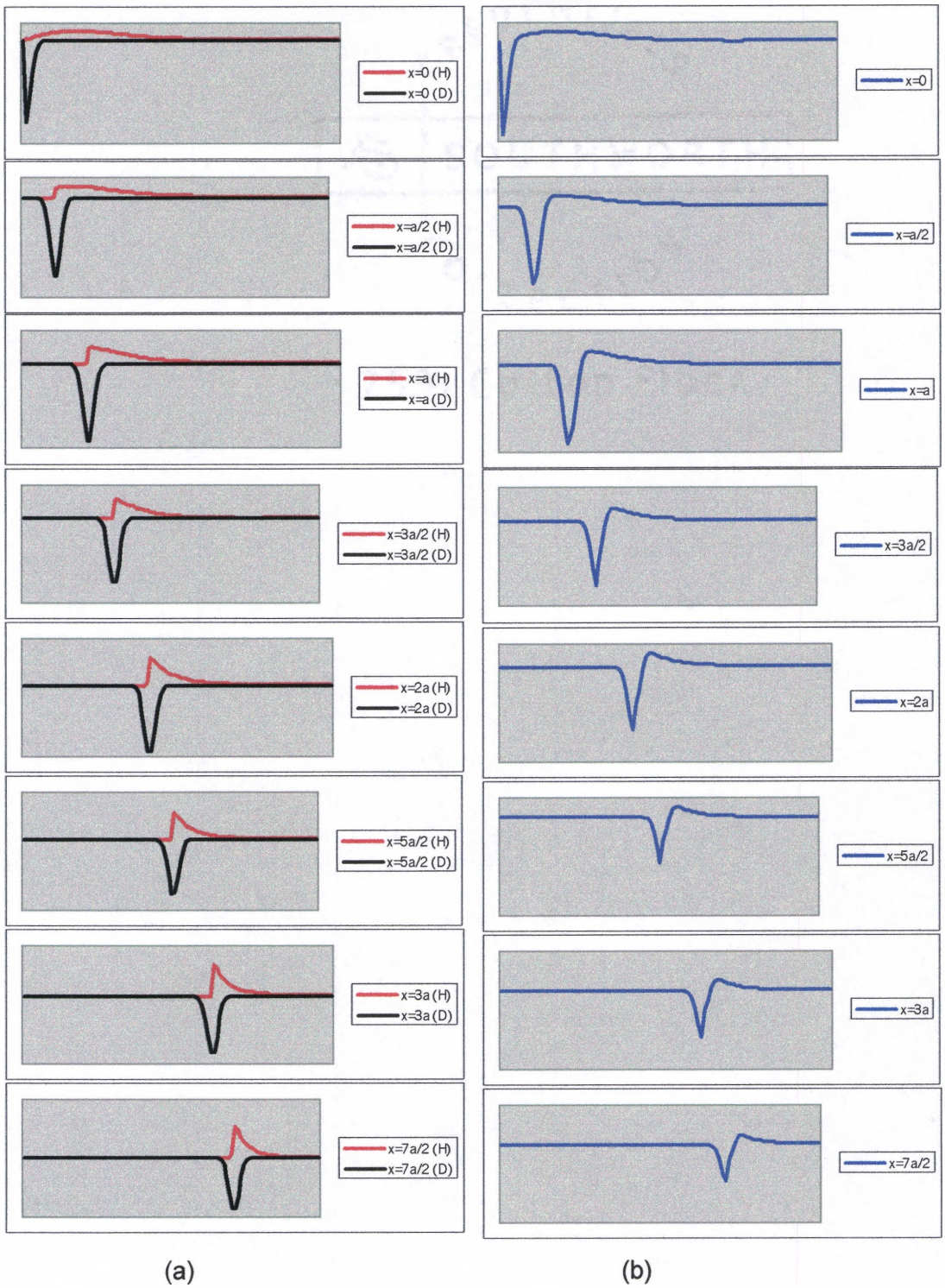

Figure 23 (a) H and D components of the surface displacement plotted separately at various distances with respect to the source center. (b) H and D components combined for total surface displacement indicated by equation 34.

Viewing the waveform contributions of the separated parts (Figure 23a), it is noticed that the D(x,t) component (black line) varies little in shape with distance. The H(x,t) component however, is temporally broad in the very near-field and becomes more narrow as the distance from the source is increased. From the combined waveforms (Figure 23b) it can be seen that the near-field waveform is primarily a monopolar depression followed by a broad upward displacement. As the distance from the source is increased, and the H(x,t) function narrows, the waveform begins to resemble a more bi-polar shape. This result, and the waveforms shown in Figure 23b, are similar in shape to the modeling and experimental results and obtained by Royer and Chenu[35] for a laser line-source.

2.3 DETECTION OF SURFACE ACOUSTIC WAVES USING HETERODYNE INTERFEROMETRY

Heterodyne techniques in interferometry allow for the detection of very small changes in optical path length[23,24,25]. In this discussion the change in path length is a result of a surface displacement due to traveling SAW's. Heterodyne interferometry involves, much like standard interferometric techniques, the interference of two beams. In the heterodyne arrangement, however, a frequency shift is typically introduced into the reference beam signal. A schematic of a typical heterodyne interferometry system, used for detection SAW's, can be seen in Figure 24.

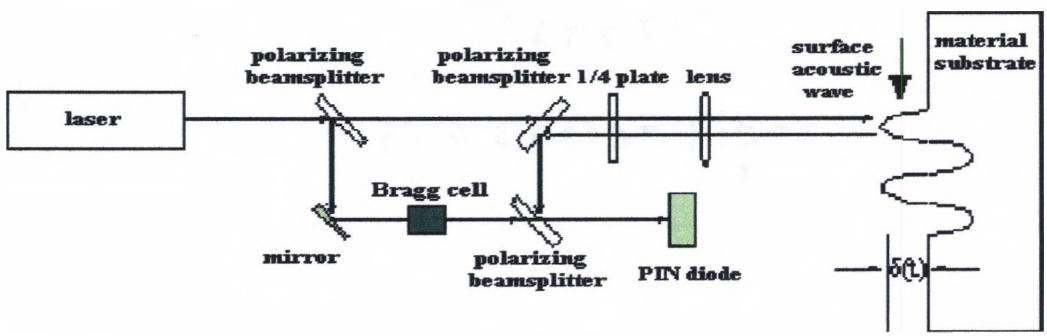

Figure 24 Diagram of heterodyne interferometry system used for SAW detection.

The theory for heterodyne interferometers involves the interference of two beams whose electric fields can be described by[25]

$$\begin{aligned} E_1(t) &= a_1 \cos(2\pi v_1 t + \phi_1) \\ E_2(t) &= a_2 \cos(2\pi v_2 t + \phi_2) \end{aligned} \qquad \text{Eq. 40}$$

where a_1, a_2 are the amplitudes, v_1, v_2 are the frequencies, and ϕ_1, ϕ_2 are the phases of the respective fields. The intensity detected by an ideal square-law detector is[25]

$$\begin{aligned} I(t) &= [E_1 + E_2]^2 \\ &= \frac{1}{2}a_1^2 + \frac{1}{2}a_2^2 \\ &+ \frac{1}{2}\left[a_1^2 \cos(4\pi v_1 t + 2\phi_1) + a_2^2 \cos(4\pi v_2 t + 2\phi_2)\right] \\ &+ a_1 a_2 \cos[2\pi(v_1 + v_2)t + (\phi_1 + \phi_2)] \\ &+ a_1 a_2 \cos[2\pi(v_1 - v_2)t + (\phi_1 - \phi_2)] \end{aligned} \qquad \text{Eq. 41}$$

Using the valid assumption that a practical detector cannot detect the higher frequencies $2v_1, 2v_2$, and $(v_1 + v_2)$[25,26], equation 41 can be simplified to

$$I(t) = A + B\cos[2\pi\Delta v t + \Delta\phi] \qquad \text{Eq. 42}$$

where $A = \frac{1}{2}a_1^2 + \frac{1}{2}a_2^2$, $B = 2\left(\frac{1}{2}a_1^2 + \frac{1}{2}a_2^2\right)^{1/2}$, $\Delta v = v_1 - v_2$, and $\Delta\phi = \phi_1 - \phi_2$.

The output thus contains an ac component with a frequency equal to that of the induced frequency shift Δv whose phase is $\Delta\phi$. If the out of plane surface displacement is $\delta(t)$, then the change in optical path length is $2\delta(t)$, and the time dependant phase of the detected intensity can therefore be described by[3]

$$\Delta\phi(t) = \phi_o + \frac{4\pi}{\lambda}\delta(t) \qquad \text{Eq. 43}$$

where ϕ_o is the nominal phase difference between the reference and probe beams and λ is the wavelength of the laser source. Using equations 42 and 43, the actual surface displacement can be found by a phase-demodulation of the acquired signal.

2.4 LASER ULTRASONIC CRACK DETECTION TECHNIQUES

The incorporation of non-contact laser technology in ultrasonic NDE, specifically the detection of surface-breaking cracks, has emerged in the last decade[3,4,11-16]. A recent technique, termed near-field scanning interferometery (NFSI)[3,11,12,15], involves the use of a contact transducer for the generation of surface acoustic waves and a non-contact laser interferometer for the detection surface wave fields and their interaction with defects. This NFSI technique has also shown the ability to not only detect/locate surface-breaking cracks but to image, based on a near-field intensification of ultrasonic displacement fields, the defect on the surface of a material. Another laser-based method, the scanning-laser source (SLS), uses the laser detection and the laser generation of SAW's to provide crack detection/characterization capabilities[17,18]. An overview of these techniques, as well as a combination of the two which is developed in this work, will be given here.

2.4.1 NEAR FIELD SCANNING INTERFEROMETRY (NFSI)

In previous experimental work[3,11,12,15], an ultrasonic contact transducer was used to generate Rayleigh waves on a sample surface and a laser heterodyne interferometer (Polytec OFV301) was used to detect out-of-plane displacement levels. By positioning the transducer such that Rayleigh waves propagated towards a free-boundary (edge or crack), the interferometric probe could then be scanned in the vicinity of the free-boundary to observe the elastic-wave/boundary interaction. A schematic of this method is shown in Figure 25.

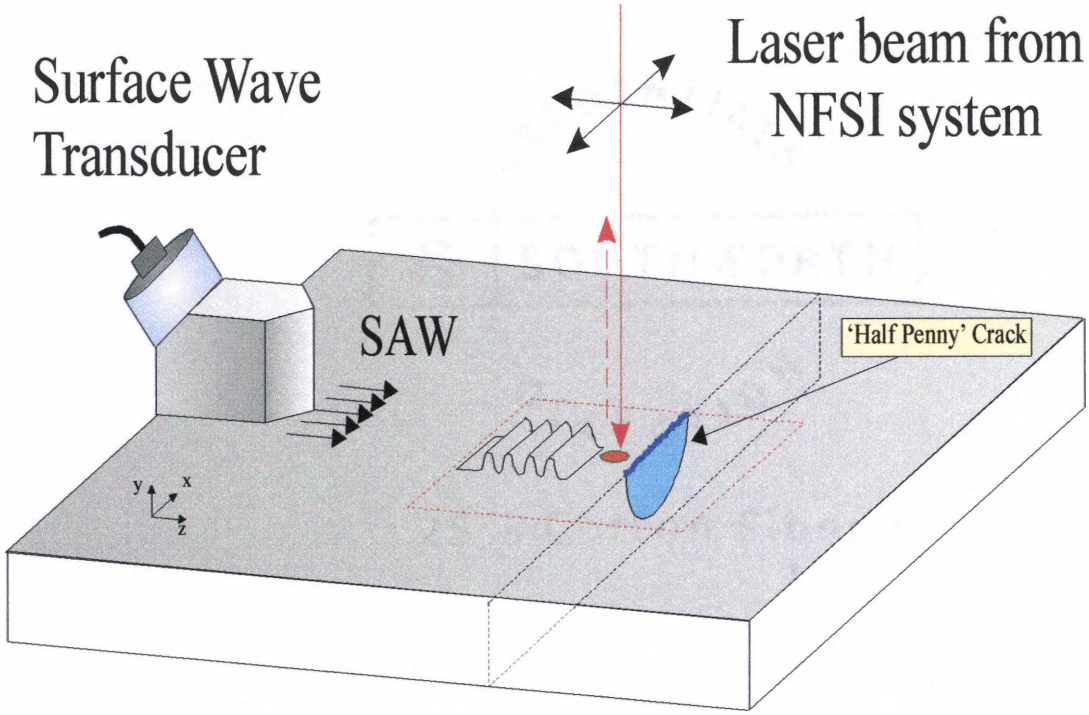

Figure 25 Diagram of crack imaging concept using a surface wave transducer for excitation.

In figure 26, a diagram is used to show the detection laser approaching a crack and the incident and reflected SAW's which are detected. As is shown in the diagram, when the detection beam is situated between the SAW generating transducer and a surface-breaking crack, the first detected signal will be the incident waves directly from the transducer. As the SAW's propagate some distance Δz past the detection laser to the surface crack, they are reflected backward and are again measured by the laser detection process. In the typical voltage vs. time output of the interferometric receiver, the detected incident and reflected surface displacements will be separated by the time it takes for the SAW to propagate past the laser probe, to the crack, and back, a distance of $2\Delta z$. As the detection laser is scanned closer to the crack, these signals are shifted closer together in time. In the region very near the crack, the incident and reflected waves are superimposed. This superposition of

waves, along with other near-field scattering processes, result in a significant signal amplification in the immediate vicinity of the surface-breaking defect[3].

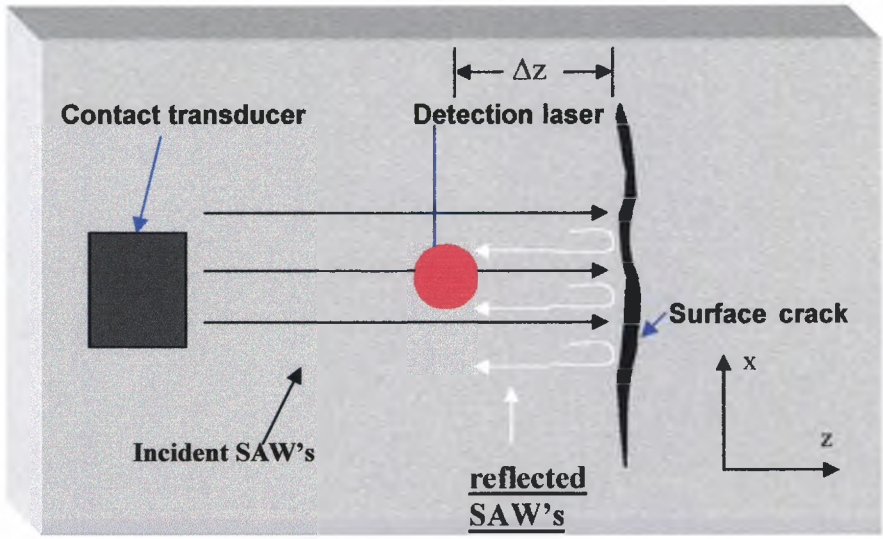

Figure 26 Diagram showing positioning of laser interferometer and the incident and reflected waves generated by the transducer and reflected from the crack, respectively.

An example of the detected SAW amplitude vs. the detection laser position is shown in Figure 27. Three distinct positions of the detection laser, relative to the transducer and the crack, are also shown schematically in Figure 27. These positions are labeled and the corresponding charactersitic amplitudes are labeled in the amplitude vs. position diagram. These figures show that when the detection beam is between the transducer and the crack the detected amplitude remains at a steady value. As the detection laser approaches the crack, an intensification of the measured signal occurs. When the laser crosses the crack, the amplitude drops significantly as little energy is transmitted through the defect.

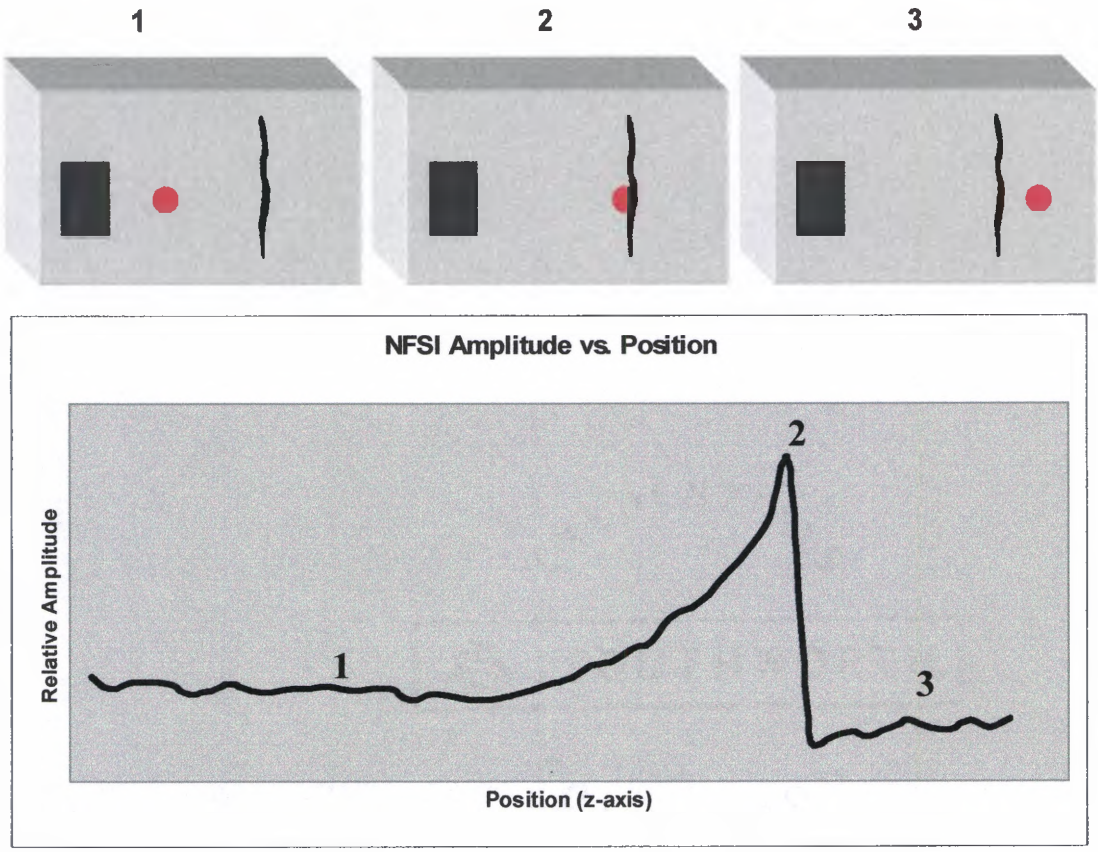

Figure 27 Example of detected amplitude vs. position using the NFSI technique.

Modeling of this observed near-field intensification has been achieved by Blackshire[3] using a wave superposition model and by Aldrin et.al.[19] using Finite-Element and Boundary-Element models (BEM and FEM). The results of these models, courtesy of the respective authors, are shown in Figure 28.

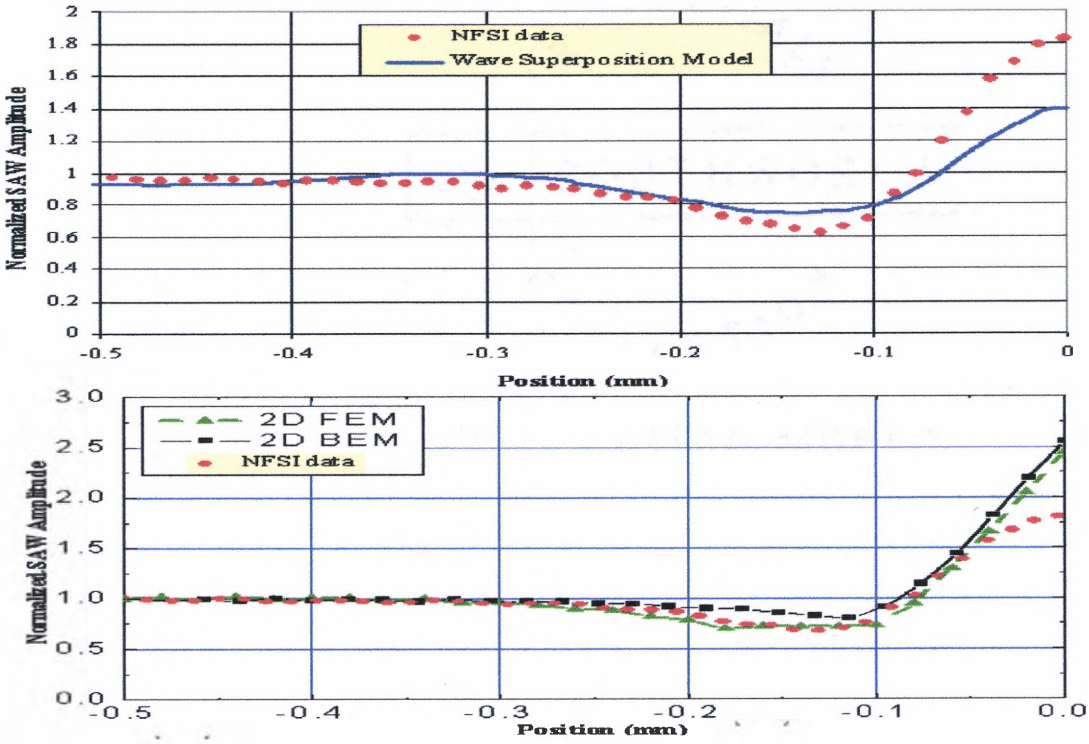

Figure 28 Wave-superposition model results[3] (above) and BEM and FEM modeling of elastic wave intensification at a free-boundary[19] (below).

The wave-superposition model showed reasonable agreement with experimental results, but under-estimated the intensification. The FEM and BEM modeling results were also in reasonable agreement with the experimental results, but over-estimated the near-field intensification. Additional experimental and modeling studies are currently underway in an attempt to understand these observed differences.

In addition to crack detection/location capabilities, the NFSI technique was also developed into a point-by-point, two-dimensional, surface-crack imaging system[3,11,12,15]. Exploiting this observed near-field intensification of the SAW amplitude in the vicinity of surface-breaking defects, a point-by-point raster scanning of the detection laser was used allowing for grey-scale images to be produced based

upon the detected amplitude at each point in the measurement[3,11,12,15]. An example of this crack imaging capability provided by the NFSI technique is shown in Figure 29.

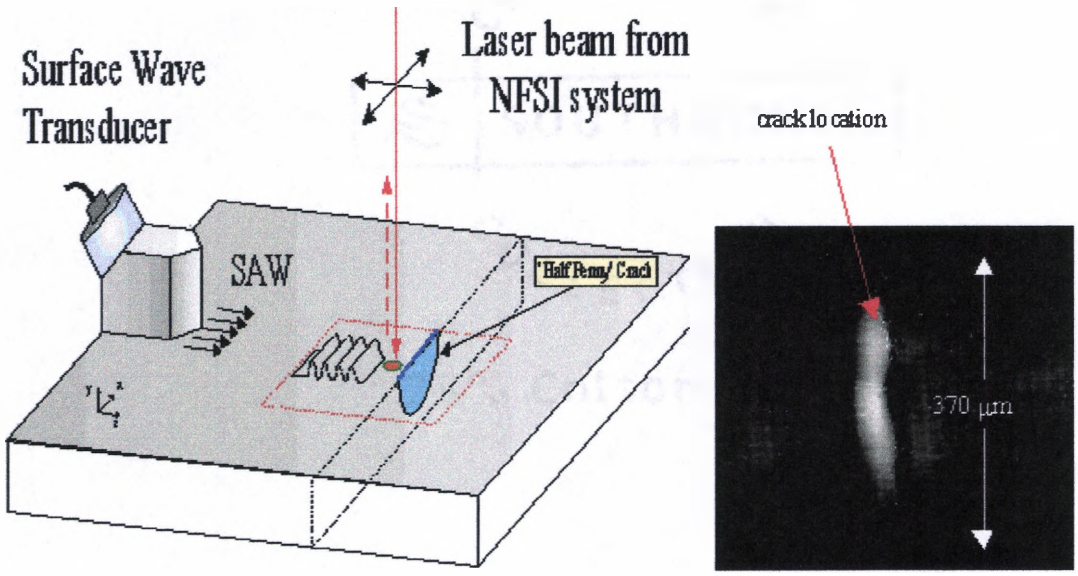

Figure 29 NFSI schematic (left) and image produced using this technique (right)[3].

2.4.2 SCANNING LASER SOURCE (SLS) TECHNIQUE

Another approach for the detection of surface-breaking cracks termed the scanning laser source (SLS) has been developed by Kromine et. al[17]. In this method, the ultrasonic surface wave source involves a pulsed laser, usually expanded by a cylindrical lens into a line, which is scanned across a material surface. The detector in the SLS technique is typically held stationary on the material surface, however, and uses either a contact transducer or laser interferometric probe beam. A schematic representation of this method is shown in Figure 30.

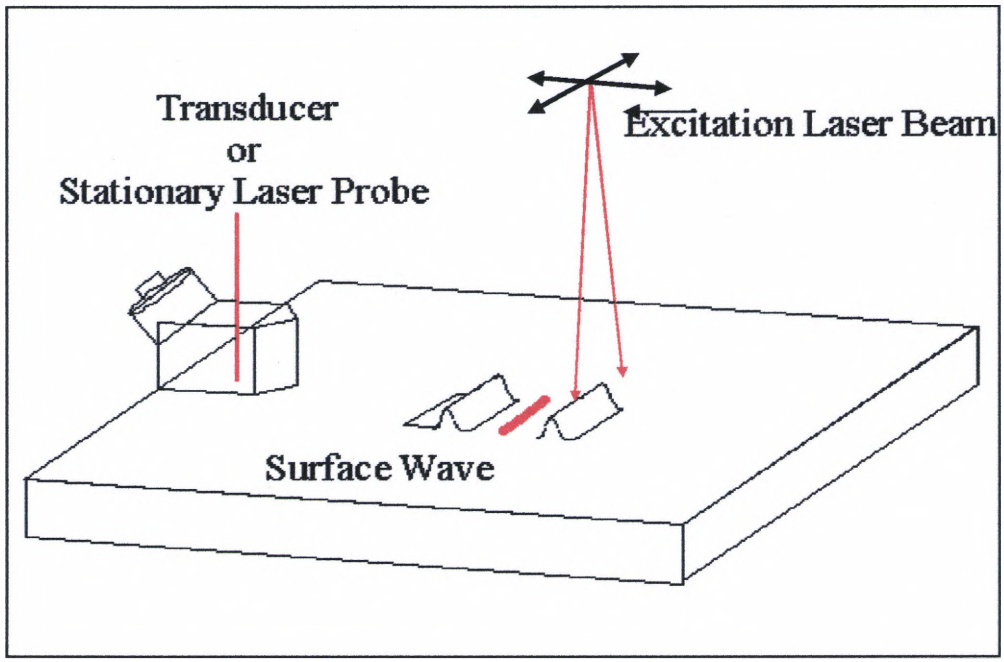

Figure 30 Schematic of Scanning Laser Source (SLS) crack measurement concept.

The use of a cylindrical lens to create a line source is implemented in this technique to optimize the directionality of the generated SAW energy[17]. Figure 31 shows the primary direction of energy propagating from both a line source and a Gaussian or circular generation spot. From the figure it can be seen that, for a measurement where the excitation laser is to be scanned exclusively in the +x and -x directions, the use of a laser line source would optimize the SAW energy propagating in these directions. The Gaussian or circular source on the other hand emits energy equally in all radial directions and thus is not optimized for any preferential scanning direction.

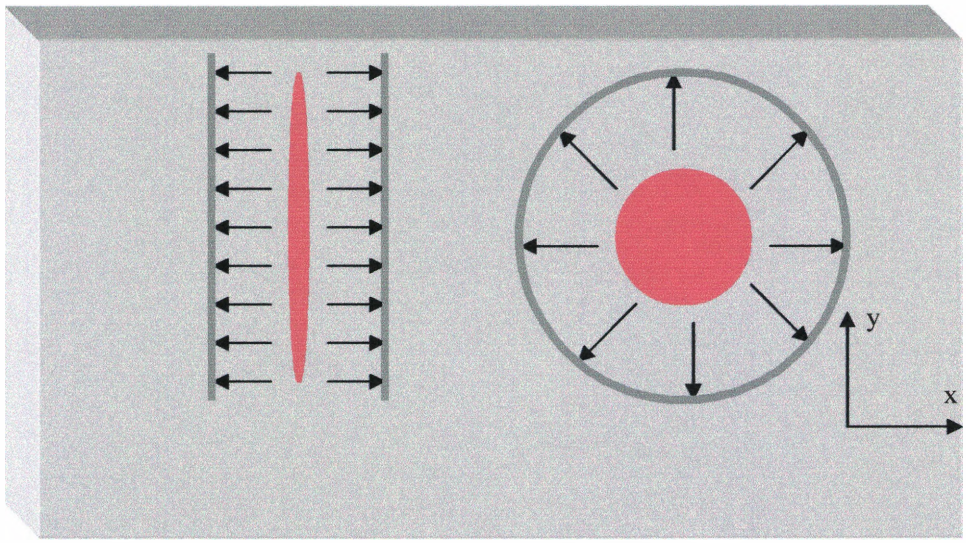

Figure 31 Directionality of SAW's generated with both a line source (left) and a Gaussian or circular spot (right).

In figure 32, the basic concept for crack detection using this SLS technique is shown. This diagram shows a laser line source used for the generation of SAW's and a laser probe for detection. As shown previously in Figure 31, the laser line source emits energy primarily along the x-axis, equally in both the +x and –x directions. As shown in Figure 32, the detector would first receive the initial wave that propagated in the –x direction, towards the detector. The wave from the laser line source that initially propagates away from the detector (+x direction) and towards a surface-breaking crack, located a distance Δx from the excitation source, is reflected and then propagates back towards the detector (-x direction). This reflected wave, since it has traveled a distance Δx to the crack and Δx back to the source, would trail the initial detected wave by a distance of 2Δx. As the excitation laser is moved closer to the crack, this distance Δx approaches zero and thus, both the reflected and incident waves approach identical arrival times at the detector. When the excitation source is

at the crack, the incident and reflected waves are superimposed and thus an intensification of the detected signal is observed.

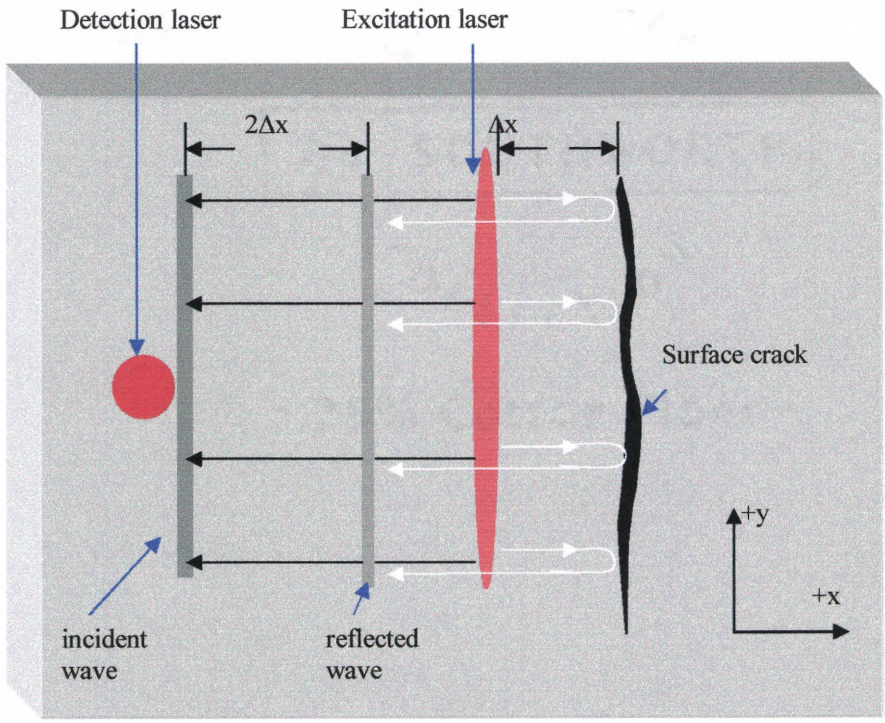

Figure 32 Diagram depicting incident and reflected waves propagating towards the detector in the SLS crack detection technique.

For a qualitative example of the crack detection capabilities of this technique, measurements taken by scanning a Gaussian beam over a surface-breaking crack and detecting with a laser interferometer are shown in Figure 33. In this figure, three primary regions of interest are labeled and correspond to the beam positioning diagrams also shown in Figure 33.

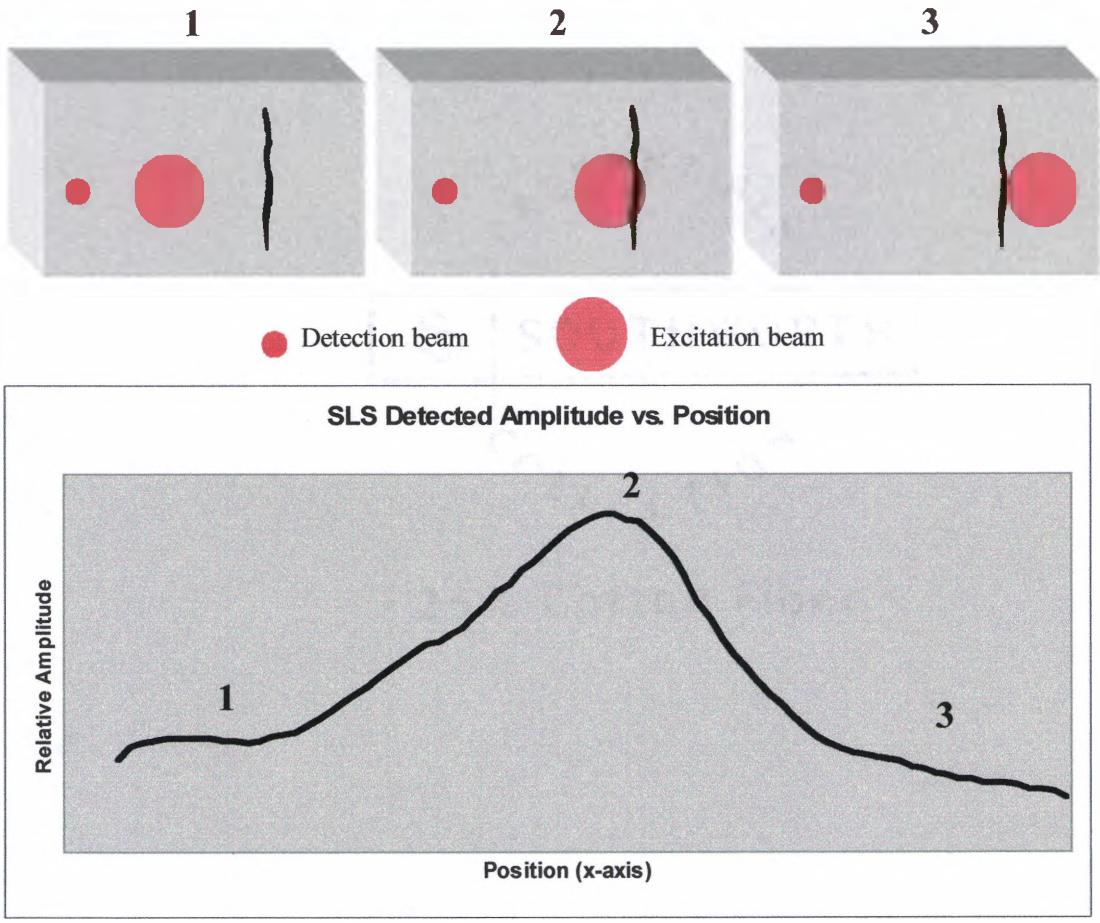

Figure 33 Beam positioning diagrams (above) and detected relative peak-to-peak amplitude vs. position for this SLS technique.

As shown in Figure 33, the detected amplitude in region 1, before the excitation beam is near the crack, remains virtually unchanged. As the beam approaches and reaches the crack (region 2), a dramatic increase in the detected peak-to-peak amplitude is observed. In region 3, where the source and receiver are on separate sides of the crack, a reduction of detected amplitude, below the initial levels of region 1, is observed due to little or no energy propagating through or around the defect.

In the work of Kromine et. al.[17] results similar to those shown in Figure 33 were reported. The increase of the signal near the crack was attributed not only to the superposition of the incident and reflected waves, but also to as the change in the material conditions at the defect in which the thermoelastic laser source induces the ultrasonic waves[17]. Successful modeling of this SLS technique using a mass-spring lattice model (MSLM)[20,21] has been reported[22].

2.4.3 DUAL-BEAM SCANNING

In this thesis work, a combination of both the NFSI technique and the SLS method was developed. A pulsed laser source with a Gaussian spatial distribution is used for the thermoelastic generation of SAW's. For detection, a laser heterodyne interferometer system is used, which ultimately provides for a completely non-contact NDE measurement capability. Unlike the NFSI and SLS techniques, however, the dual-beam scanning configuration developed in this thesis utilizes–thermoelastic near-field effects (i.e. generation and detection lasers are closely positioned), while scanning both beams across the surface of a material. As will be discussed in the later chapters, the surface displacements in the very-near field of the thermoelastic source were observed to be much larger than the far-field waveforms. Thus, near-field detection allows for lower energy pulses to be used while maintaining the signal-to-noise levels needed for useful measurements to be carried out.

The ability to scan both the source and receiver at a fixed, closely positioned separation distance provides several unique advantages. The first, as mentioned previously, is the large amplitude displacements detected in the generation near-field. Traditionally in ultrasonics, the generation near-field, which is comprised of complicated interference waveforms, has been considered unusable, in some cases referred to as the 'dead zone'[4]. For this reason, traditional contact transducer and

laser generated ultrasonic measurements have typically been carried out using far-field detection methods, where the waveforms appear less complicated and more consistent[4]. As will be shown in later chapters, however, scanning both laser ultrasound beams at a fixed separation distance does indeed provide consistent detected waveforms, since the source-receiver separation remains unchanged, and thus the large amplitude waveforms in the near-field can be exploited.

Another interesting and potentially useful aspect of a dual-beam scanning approach is the ability to detect SAW intensification at a crack in a manner similar to the NFSI and SLS techniques. Referring back to Figures 27 and 33, which showed characteristic amplitude vs. position diagrams for the NFSI and SLS techniques, respectively, Figure 34 provides an example of a crack measurement generated using the dual-beam scanning system. Because the dual-beam scanning system takes measurement aspects from both the SLS and NFSI techniques, the measurement result shown in Figure 34 shows a peak-to-peak amplitude intensification similar to the SLS technique at position 2, and an intensification similar to the NFSI technique at position 5.

The reason behind this can be explained as follows. As both laser beams approach and reach the crack (positions 1 and 2), the excitation beam interacts with the crack in a manner similar to the SLS measurement approach. At positions 3 and 4, the beams are separated by the crack, and thus little surface acoustic wave energy is detected. As the detection beam crosses the crack (position 5) there is a sharp increase in the detected signal, and then a decay as this beam is moved further away (position 6). This detected intensification at position 5 is due to a measurement approach that is similar to the NFSI technique. Therefore, in this dual-beam scanning configuration, characteristics of both the NFSI and SLS crack detection techniques are realized in the actual measurement results. Further, as will

be shown in later chapters, differences in the waveform behavior at each of these characteristic intensifications can be discriminated from one another by applying an appropriate analysis procedure. This ultimately provides sharp, highly resolved images of the surface-breaking cracks to be made.

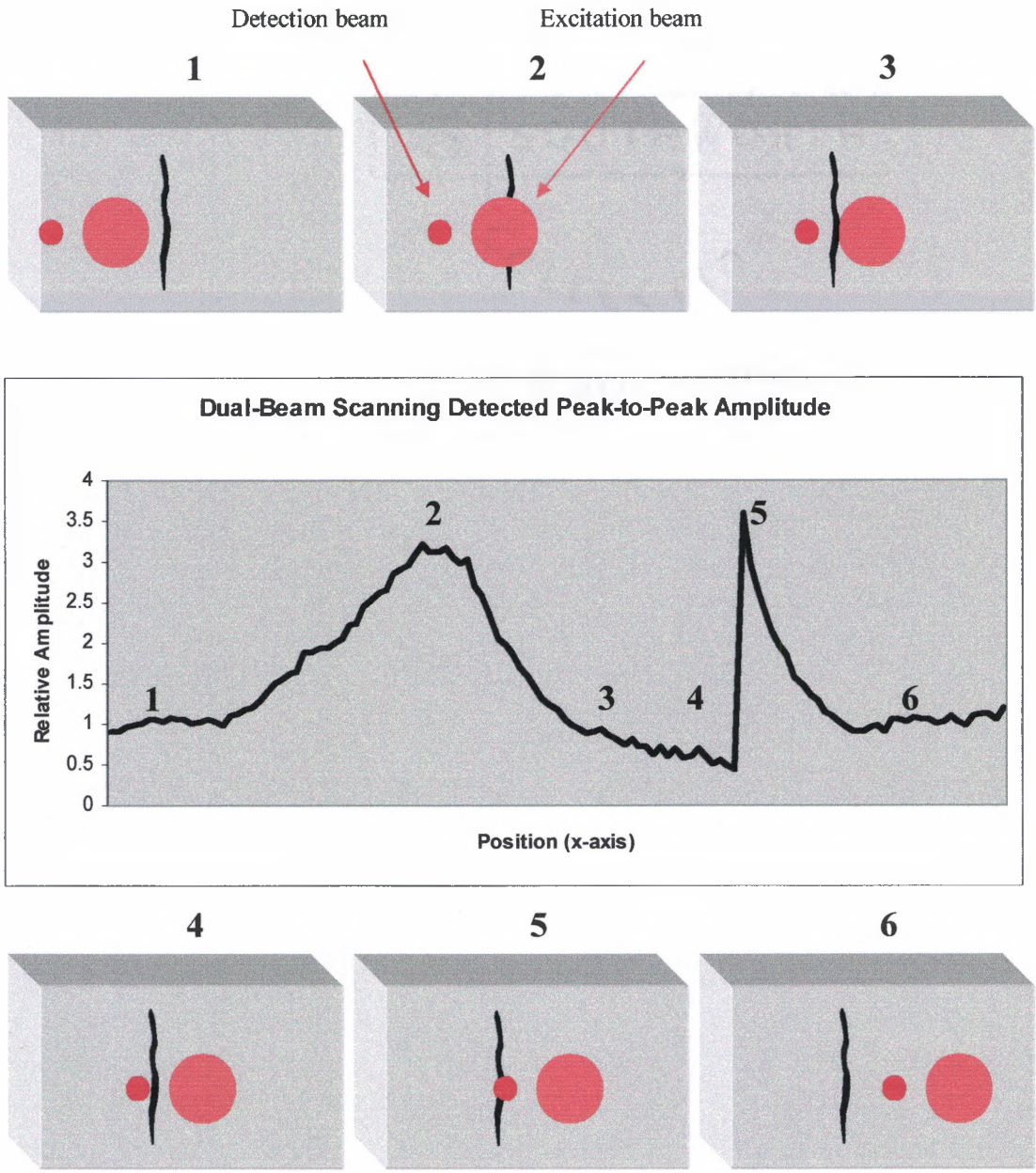

Figure 34 Beam positioning diagrams (above and below) and detected relative peak-to-peak amplitude vs. position (middle) for the dual-beam scanning technique.

CHAPTER III

EXPERIMENTAL PROCEDURE AND EQUIPMENT

In this section, a general description of the equipment used (i.e. the generation and detection laser systems) will be given. Measured and calculated characteristics of the excitation laser which are important for the purpose of laser ultrasound generation will also be presented. Finally, the incorporation of both laser generation and laser detection devices into a completely automated, dual-beam scanning system will be discussed.

3.1 THE EXCITATION LASER

The excitation laser used was a Q-switched Alexandrite laser (Light Age, Inc. Model 101 PAL). A schematic of the laser cavity can be seen in Figure 35. Although the system allows for wavelength variability, in all cases it was operated at λ=753 nm. The repetition rate of this laser was set to 20Hz by the manufacturer, and verified by observing the pulses on an oscilloscope. The maximum output energy was measured in terms of power, and then calculated, based upon this repetition rate, to be ~30mJ/pulse.

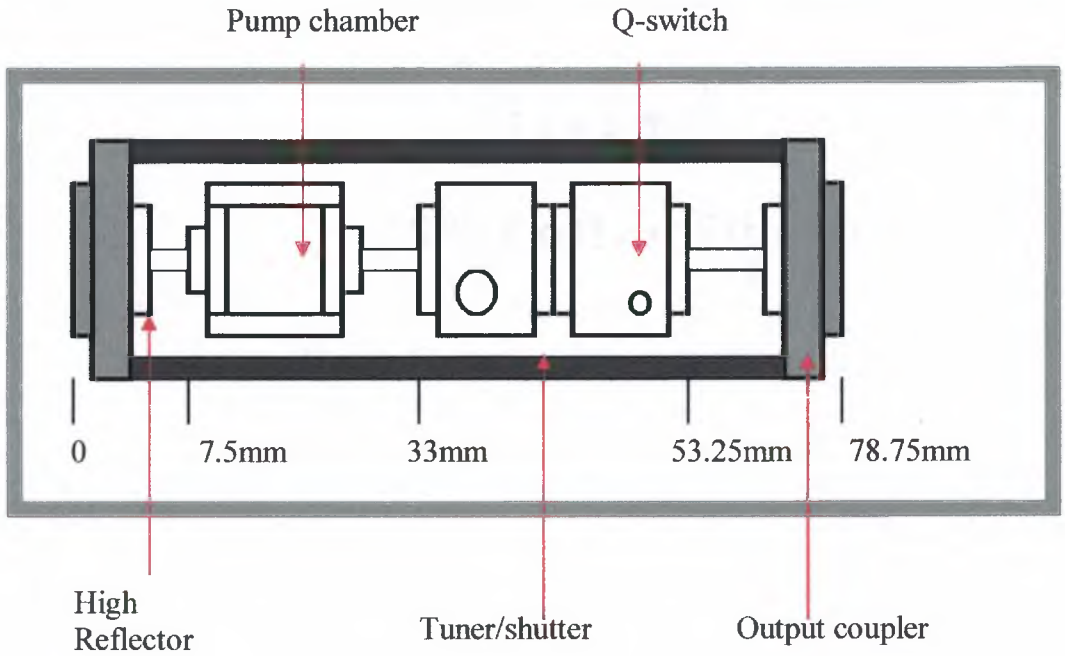

Figure 35 Diagram of laser cavity and components[36].

The temporal properties of this laser, measured using a PIN diode, can be seen in Figure 36 and Figure 37 for both the long pulse and Q-switched operating modes, respectively.

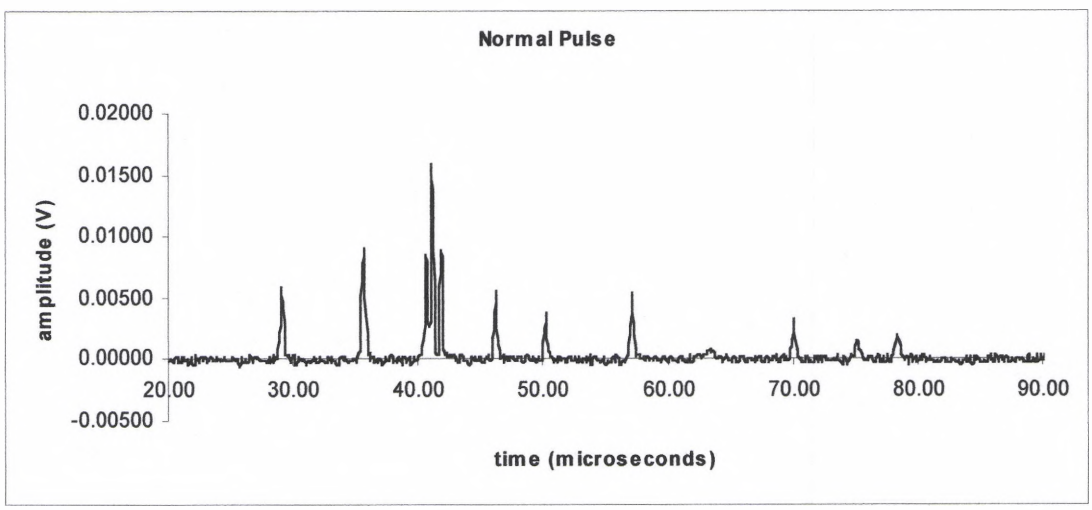

Figure 36 Temporal profile of laser pulse in normal (long pulse) operating mode.

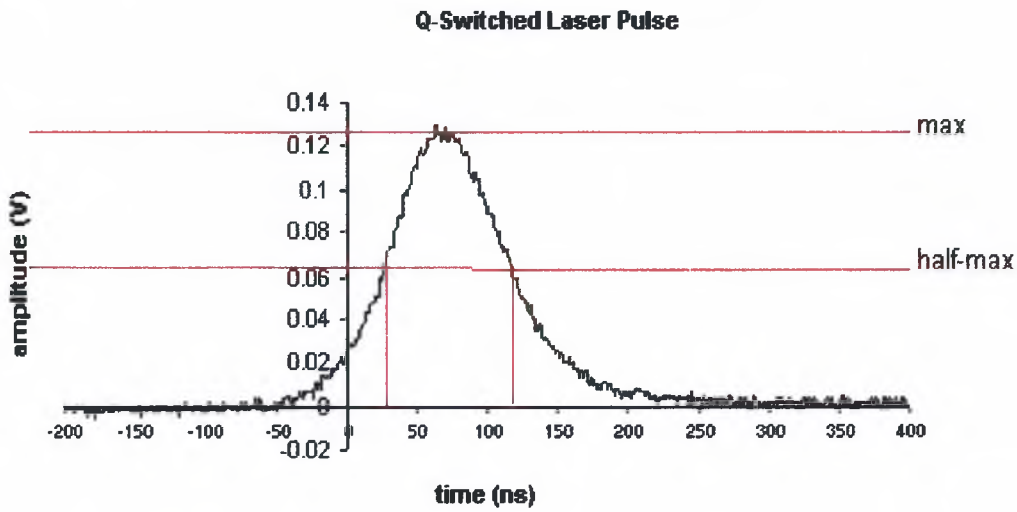

Figure 37 Temporal profile of laser pulse in Q-switched operating mode.

In the normal pulse operating mode, (Figure 36), multiple pulses are detected over a period of 30 to 50 microseconds. These multiple pulses, due to relaxation oscillations, were also observed to be inconsistent from pulse to pulse. The Q-switch pulse (Figure 37) however, was measured and displayed a consistent pulse shape with a full-width half-max (FWHM) of approximately 100ns. Due to this consistency, and a relatively short pulse, it is the Q-switched operating mode which is most commonly used for the laser generation of ultrasound[4].

3.2 DETERMINING LASER SPOTSIZE

For the determination of various excitation laser spotisizes, the raw beam emerging from the laser cavity was first measured. The technique used for this measurement was indirect and made under the assumption that the intensity distribution of the beam was Gaussian. This assumption should, however, be valid based upon the laser specifications and observations made using laser burn papers.

The raw beam laser spotsize was measured using a single razor blade placed on a translation stage. The blade and stage were closely positioned in front of

a power meter and systematically moved perpendicular to the beam as to gradually intercept the laser energy (figure 38).

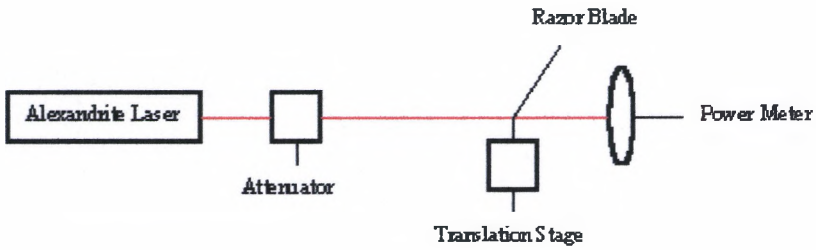

Figure 38 Raw beam intensity measurement for the determination of laser spotsize.

The basis for this measurement was based on the following analysis: Consider a Gaussian amplitude distribution for a beam with diameter b given by

$$A = \exp\left(\frac{-4x^2}{b^2}\right) \qquad \text{Eq. 44}$$

The intensity, the measurable quantity, is simply $I = A^2$. The entire intensity would therefore be measured by, theoretically, by integrating over x from –infinity to +infinity. Since a detector has finite dimensions, this integral must be bounded with finite limits (Figure 39) thus, the maximum detectable intensity can be written as

$$E = \int_{-w/2}^{w/2} I(x)dx \qquad \text{Eq. 45}$$

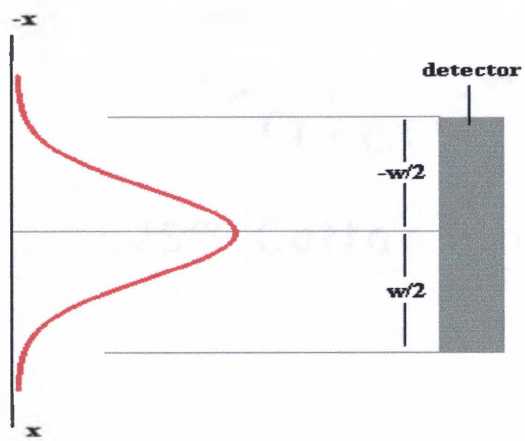

Figure 39 Diagram showing finite limits of detectable intensity.

The action of a razor blade placed into the beam path (Figure 40) can then be treated as a variable in the upper boundary of the integral.

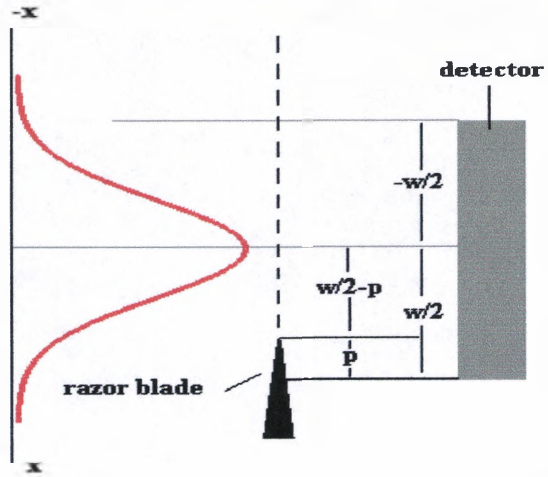

Figure 40 Diagram showing action of razor blade on boundary of detector.

Inserting this action into the integral now gives the available intensity for detection as

$$E = \int_{-w/2}^{w/2-p} I(x)dx \qquad \text{Eq. 46}$$

Evaluating this integral produces the following expression

$$E = \frac{b}{8}\sqrt{\pi}\sqrt{2}\left[\operatorname{erf}\left(\frac{\sqrt{2}(w-2p)}{b}\right)+\operatorname{erf}\left(\frac{\sqrt{2}w}{b}\right)\right] \qquad \text{Eq. 47}$$

A plot of this expression, from p=0 to p=b, is shown in Figure 41.

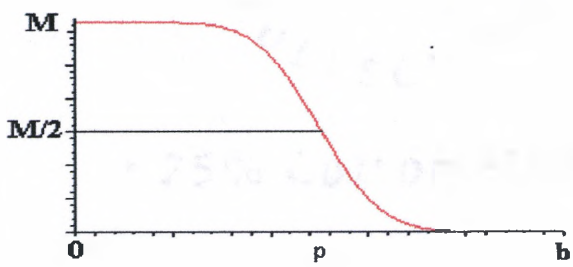

Figure41 Plot of equation 47 from p=0 to p=b. M and M/2 refer to relative intensities.

Using data obtained in this manner, a relation can then be made between intensity values at various positions of the razor blade and the actual beam waist. For instance, if two points are chosen at 90% and 10% of the maximum measured intensity (Figure 42a), then the separation of these respective positions is proportional to the beam diameter of a Gaussian beam (Figure 42b).

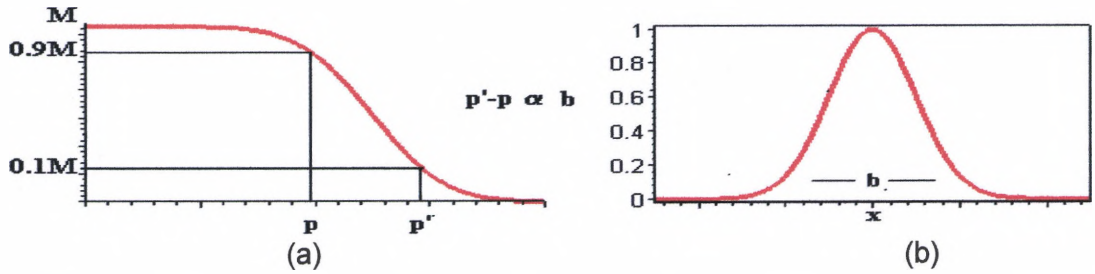

Figure 42 (a) Diagram showing separation between measured values. (b) Gaussian beam diameter.

The proportionality constant for the separation between the intensity values can be found numerically. For the case of figure 42 above, the relation is

$$1.56\left(p'_{10\%}-p_{90\%}\right)\cong b \qquad \text{Eq. 48}$$

Using this procedure, two separate sets of measurements were taken at various distances from the laser output coupler. An attenuator was used to ensure the maximum detected power was, for simplicity, 100mW. The results of these measurements, analyzed in the above manner, are displayed in Table 1.

	set 1		set 2
Position (m)	diameter in mm	Position (m)	diameter in mm
0.10	2.66	0.25	2.67
0.25	2.66	0.38	2.84
0.41	2.95	0.51	2.81
0.56	3.06	0.64	3.04
0.71	3.12	0.76	3.14
0.86	3.11	0.89	3.35

Table I Measured raw beam diameters at various distances from output coupler.

To determine beam diameters with the addition of lenses added to the system, a theoretical Gaussian beam propagation technique was used. As is well known for Gaussian beams, the q-transformation through an optical system described by an ABCD matrix, is given as[26]

$$q = \frac{Aq_o + B}{Cq_o + D} \qquad \text{Eq. 49}$$

and the relationship of this parameter with the wavefront radius of curvature $R(z)$ and the beam waist $\omega(z)$ can be expressed as[26]

$$\frac{1}{q(z)} = \frac{1}{R(z)} - i\frac{\lambda}{\pi\omega^2(z)} \qquad \text{Eq. 50}$$

where, with initially plane wavefronts, $q_o = -i\frac{\pi\omega_o^2}{\lambda} = -iZ_R$ [26]. Inserting this value into equations 49 and 50, and separating into real and imaginary parts allows for $R(z)$ and $\omega(z)$ to be written in terms of the ABCD matrix as follows

$$R(z) = \frac{B^2 + Z_R^2 A^2}{DB + Z_R^2 AC} \quad \text{and} \quad \omega^2(z) = \frac{\lambda}{\pi}\left(\frac{B^2 + Z_R^2 A^2}{Z_R(AD - BC)}\right) \qquad \text{Eq. 51}$$

Since in most optical systems, the determinant of the ABCD matrix is unity (i.e. AD-BC=1), the expression for the beam waist can be simplified to

$$\omega^2(z) = \omega_o\left(A^2 + \left(\frac{B}{Z_R}\right)^2\right) \qquad \text{Eq. 52}$$

Using the equation for the beam waist provided by equation 52, an attempt to fit a theoretical Gaussian propagation function to the measured spotsize at various positions was conducted. Due to complications within the cavity (various optical elements, thermal lensing, etc.) the precise location and size of the beam waist are not known, thus these parameters were adjusted in order to find agreement with the

measured results. Figure 43 shows a comparison of the theoretical fit with the measured spotsize data.

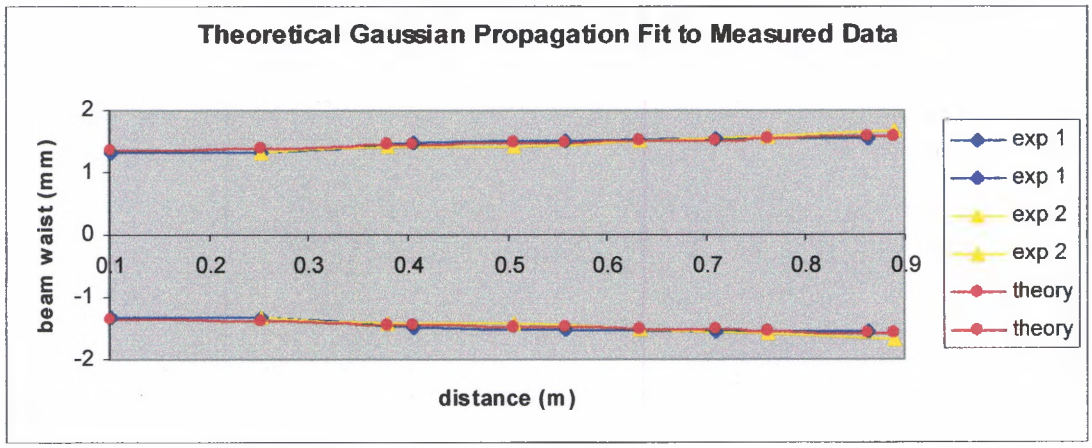

Figure 43 Experimental spotsize data with theoretical Gaussian propagation fit.

With the theoretical raw beam propagation parameters, the beam diameter in a system with various lenses can then be approximated by appropriately altering the ABCD matrix and re-evaluating equation 52. This approximation was made for the following configurations, shown in Figure 44.

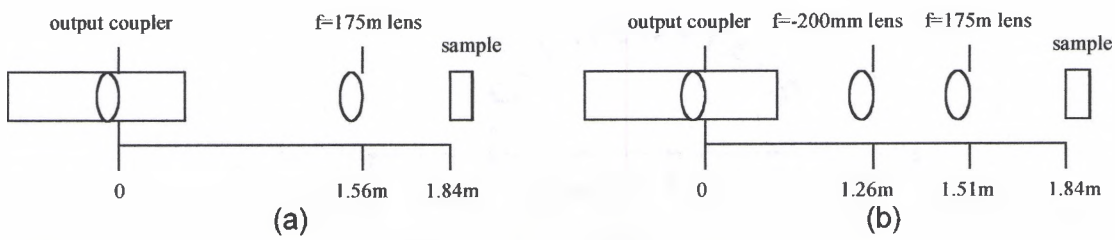

Figure 44 Diagrams for two lens setups used for varying laser spotsize.

The results for all three systems (raw beam, and setups A and B), produce the following beam diameters at a distance of 1.84m from the output coupler, shown in table 2.

Configuration	Beam Diameter
raw beam	3.29mm
A	1.70mm
B	0.94mm

Table II Theoretical beam diameters for the previously mentioned configurations.

These approximations for the beam diameters at the sample (1.84mm from the output coupler), rounded to the nearest mm, will now be referred to simply as the 3mm, 2mm, and 1mm beams.

3.3 THE DETECTION LASER

For detection of laser generated ultraound, a commercially available 1mW, cw He-Ne heterodyne laser interferometer (Polytec OFV303) was used. Details of heterodyne interferometry, and its use in detecting out-of-plane displacements, have been discussed previously in chapter 2. This interferometer is capable of detecting out-of- plane surface displacements with sub nanometer resolution in a range of 25 kHz to 20 MHz. The interferometer provides, through its demodulating unit, a voltage vs. time signal which has been calibrated, by the manufacturer, to 75nm/V. A digital image of the Polytec laser head and demodulating unit is shown in Figure 45.

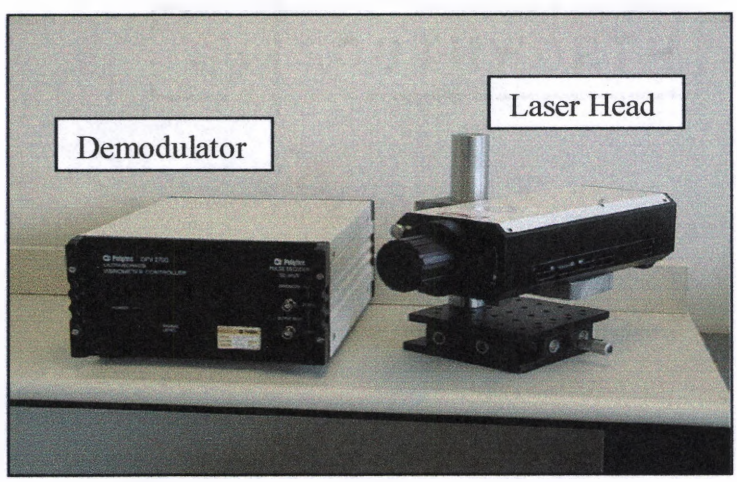

Figure 45 Polytec laser head and demodulating unit.

3.4 DUAL-BEAM SCANNING ULTRASOUND SYSTEM

A complete all optical, automated, dual-laser beam, remote generation and detection of SAW's, system has been developed for the purpose of detection, characterization, and imaging of surface breaking defects in aerospace and industrial materials. A schematic of this system can be seen in Figure 46.

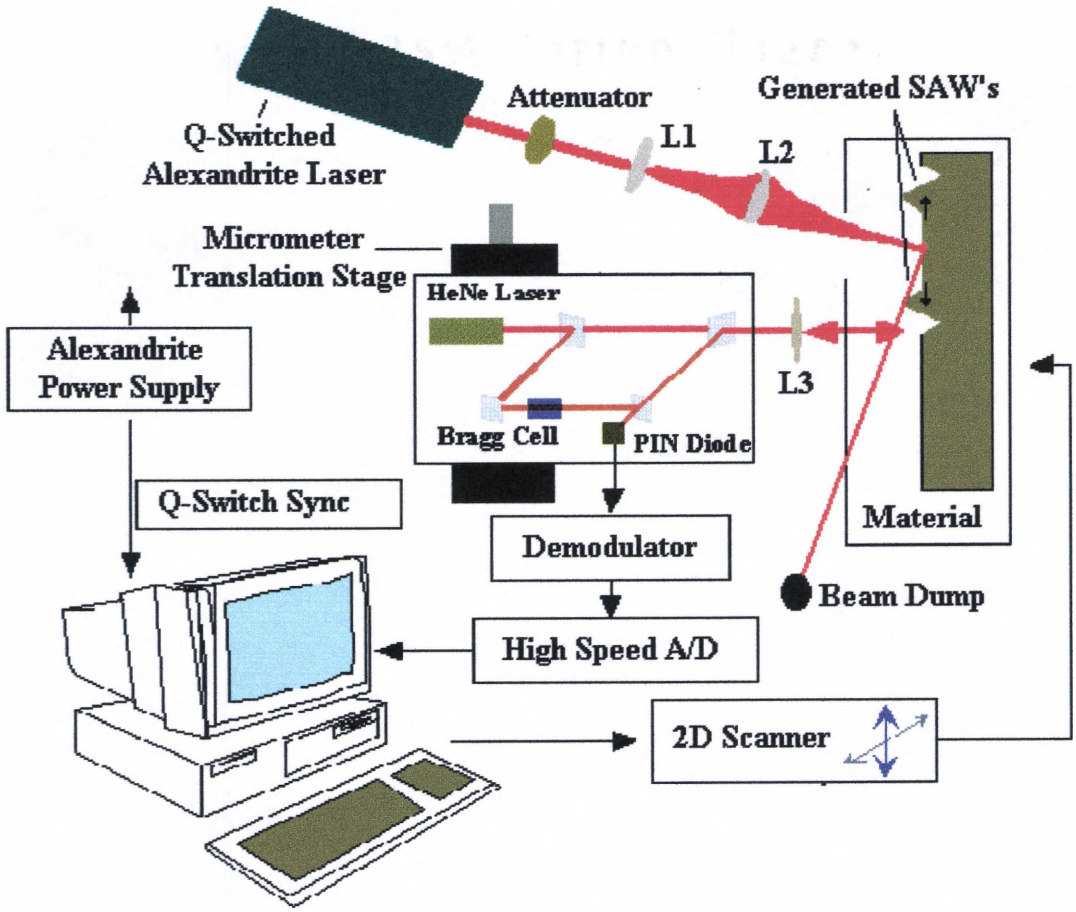

Figure 46 Non-Contact laser ultrasound generation and detection system.

In addition the diagram provided by Figure 46, digital images of the system are shown in Figures 47 and 48.

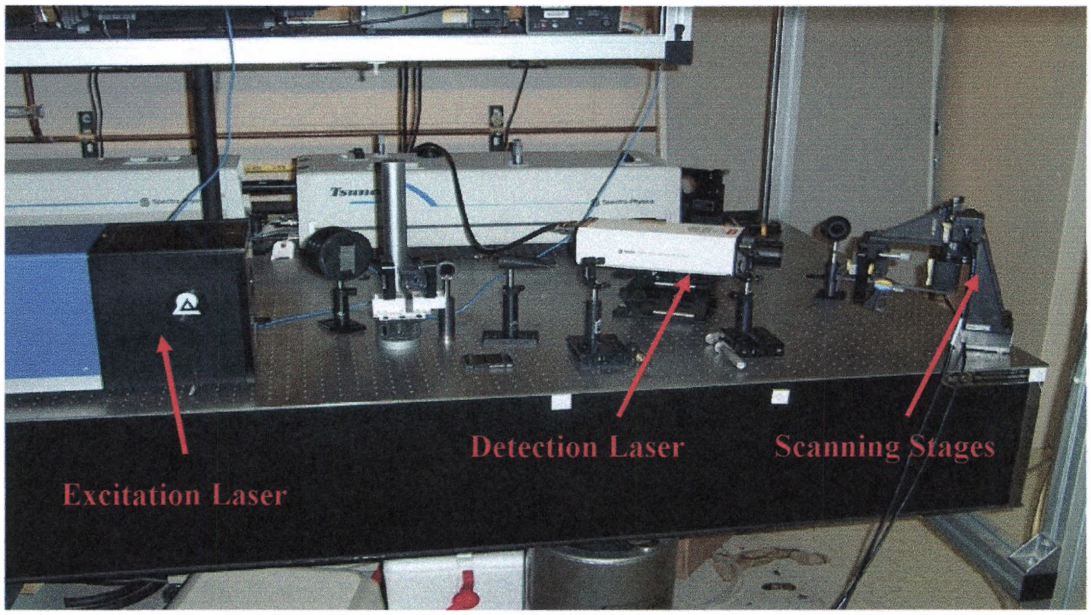

Figure 47 Digital image #1 of experimental setup.

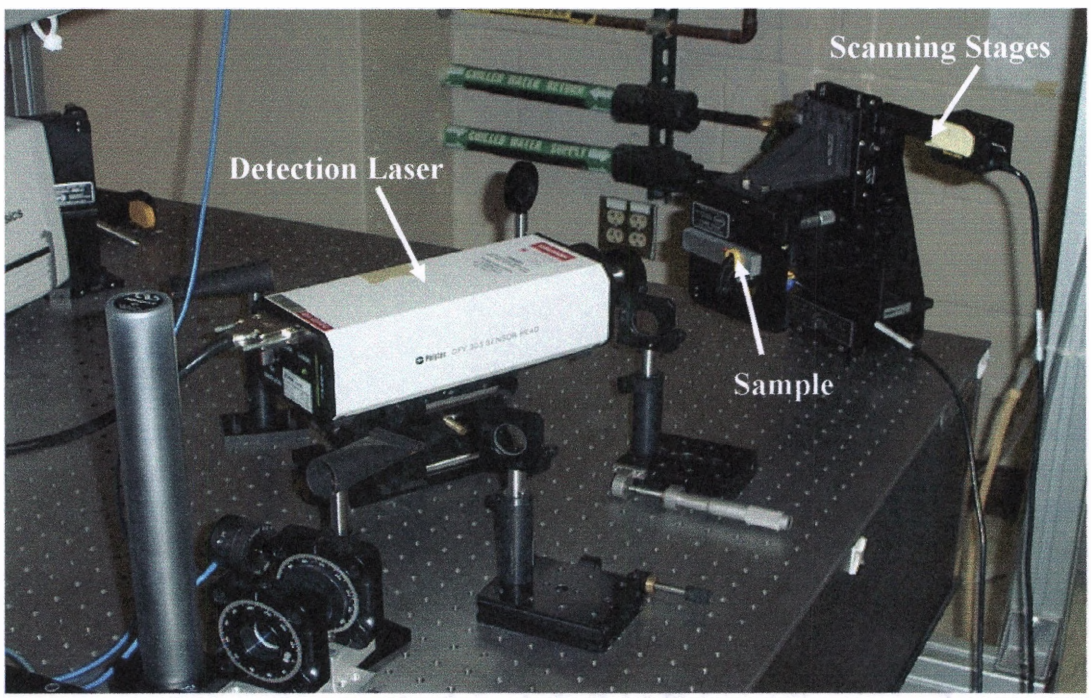

Figure 48 Digital image #2 of experimental setup.

For automated control of this system, a Labview computer program was developed. Details of this program can be found in Appendix B. The program is first triggered by the Q-switch signal sent from the Alexandrite laser power supply. Using this trigger, the program captures, through a high-speed A/D board, the time-vs-displacement demodulated voltage signal from the Polytec interferometry system.

For variations in the source-reciever separation, a manually controlled micrometer precision translation stage is placed under the Polytec laser head (Figure 46). Alternate generation beam spotsizes can by controlled by using a variety of lenses and lens positioning (L1 and L2). The detection laser head is positioned 12.5cm from the sample and focused down (L3) to a spotsize of approximately 10microns on the sample surface.

For one or two-dimensional scanning capabilities, a motor driven Melles Griot scanning stage, controlled by the computer program, was positioned under the material sample. This scanning of the sample provides the relative dual-beam raster scanning. This two-dimensional scanning system allows for an ultrasonic image to be created by monitoring, point-by-point, displacement amplitudes on the surface of the material. For this 2-D imaging configuration, a user defined scanning area and number of points to be captured is entered into the program, along with the desired number of traces to be averaged at each point. Both the single oscilloscope traces and averaged waveforms are displayed in the front panel (shown in Figure 49) as the measurement is being taken. For the image development, the peak-to-peak amplitudes are stored as greyscale values in a matrix with dimensions depending on the selected number of points to be captured. The image, along with each averaged waveform captured at every point is stored in a file allowing for further analysis to be carried out at a later time.

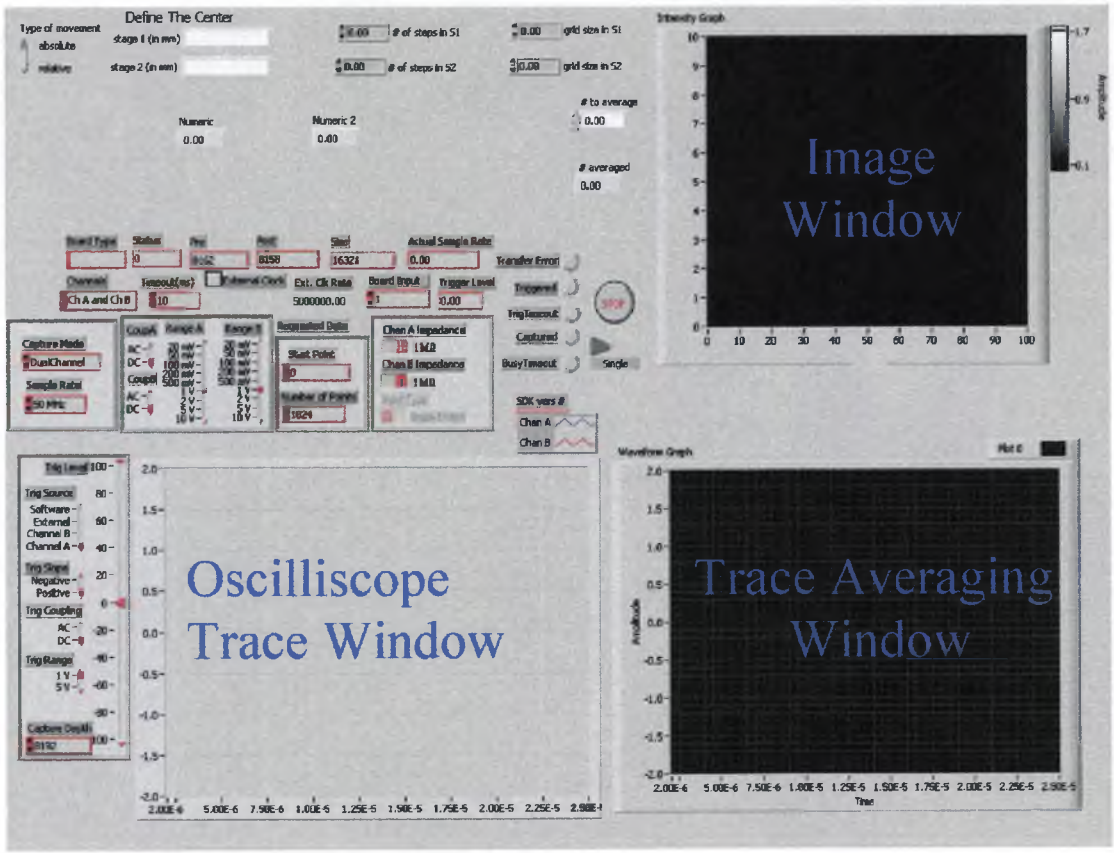

Figure 49 Front panel display of automated scanning system.

CHAPTER IV

RESULTS AND DISCUSSION

The ultimate goal of this thesis was to develop a fully non-contact NDE capability for imaging surface-breaking cracks using laser ultrasonic techniques. Before this could be accomplished, however, two important aspects of the experimental technique needed to be explored in more detail. In particular, the laser-induced thermelastic SAW generation process needed to be studied for near-field effects occurring within and in the immediate vicinity of the laser generation beam position. The influence and effectiveness of utilizing a laser-induced displacement field at a free-boundary also needed to be studied.

The first experimental study of the thesis, therefore, involved the characterization of the near-field displacements by the alexandrite laser generated thermoelastic source. Experimental observations of these near-field measurements lead to a modification being made to the previous numerical model presented in Chapter 2. The next series of measurements were conducted to characterize the SAW interaction with free-boundaries. These experiments were conducted using the ideal free-boundary provided by the edge of a material. Systematic measurements were then taken using the edge boundary, and then validated using a surface-breaking crack, in order to determine the ideal scanning parameters (generation spotsize and source/receiver separation) which should be used to detect the free-boundary intensification. A time-gated analysis algorithm was then developed to

reduce waveform noise in crack imaging measurements. Lastly, a qualitative comparison to the NFSI crack imaging technique was made for several different surface-breaking cracks.

4.1 MEASURING NEAR-FIELD THERMOELASTIC WAVEFORMS

As mentioned previously, traditional contact-transducer and laser-generated ultrasonic techniques have primarily focused on the reflection and scattering of ultrasonic fields under far-field conditions and approximations. In this thesis effort, however, an attempt was made to exploit large displacements occurring in the near-field of the ultrasonic generation region. It therefore becomes important to investigate these near-field waveforms, and how they develop into the more familiar far-field SAW's.

As mentioned in Chapter 2, the thermal expansion of a material that is induced by an incident laser pulse is the primary mechanism involved in the generation of elastic waves. This thermoelastic mechanism acts as the source of the surface acoustic waves (SAWs), which can be monitored to locate and characterize surface-breaking cracks. For the purposes of creating an optimized thermoelastically generated SAW, it becomes important to understand the material behavior at the source. Specifically, measurements of the displacement field characteristics in the immediate vicinity of the generation laser, and the dependence of these fields on the distance from the source epicenter, provide useful information.

With this in mind, a series of measurements were made to investigate the waveforms/surface displacements in the region inside and near the laser excitation source. The measurements were carried out using the basic setup described in Chapter 3. Variations in lens choice and position permitted the measurement to be repeated using three different excitation beam diameters; 1mm, 2mm, and 3mm. The

attenuator permitted the pulse energy incident on the sample to be controlled, and was adjusted for the varying laser spotsizes in order to maintain an incident laser power density of approximately 0.1MW/cm² for each measurement. For the 3mm-beam diameter, there were no lenses present in the setup. The various spotsizes were adjusted using the setups described in chapter 3. For all three measurements, the interferometry probe beam was initially placed at the center of the excitation source on the sample. Using a precision translation stage the separation distance between the excitation and detection beams could be controlled, which permitted displacement measurements to be taken at various points inside and outside the excitation laser spot. At each measurement position, 100 pulses were averaged and stored on a digital oscilloscope. The results of these measurements, displayed in a cascaded form are shown in figures 50, 51, and 52. In figures 51 and 52, the waveforms which occur at distances away from the epicenter are significantly reduced in amplitude, compared to the more near-field displacements, and are therefore magnified (indicated by arrows) for visual clarity.

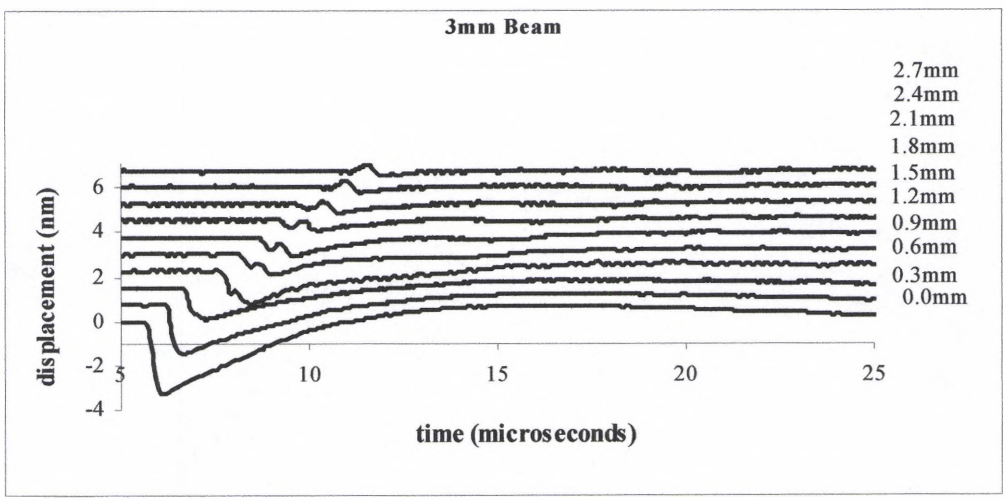

Figure 50 Displacement at various probe positions away from the excitation source center for a 3mm diameter excitation laser beam (separation distances are listed on the right of the plot).

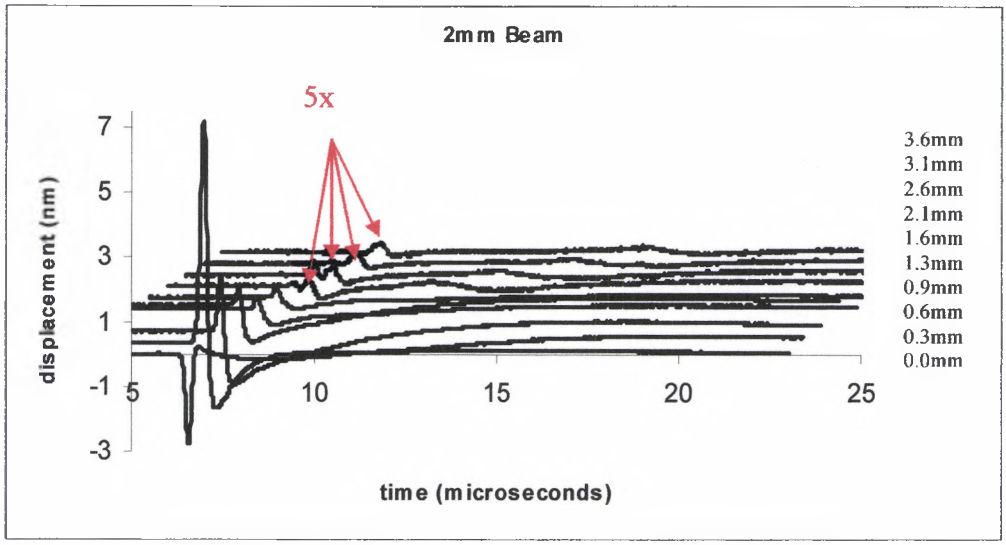

Figure 51 Displacement at various probe positions away from the excitation source center for a 2mm diameter excitation laser beam (separation distances are listed on the right of the plot).

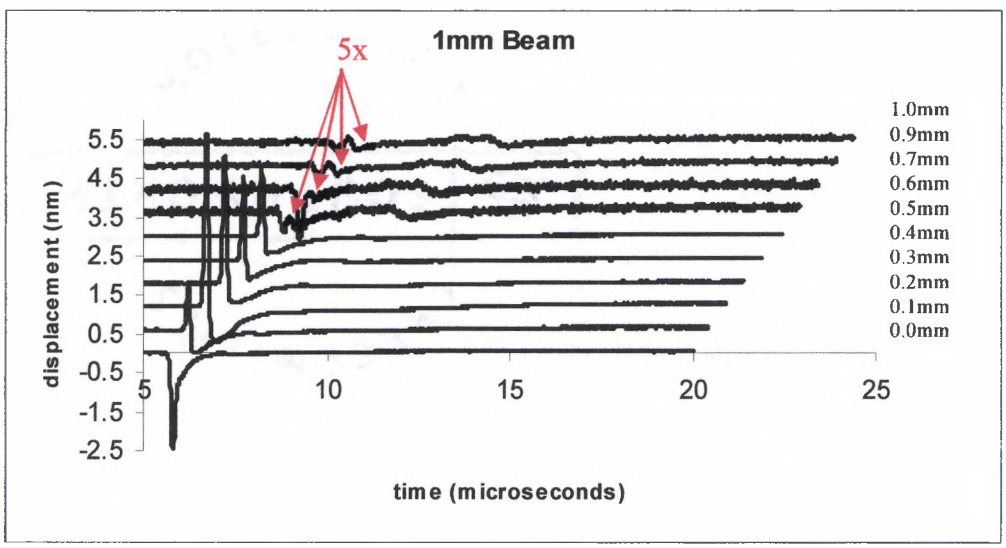

Figure 52 Displacement at various probe positions away from the excitation source center for a 1mm diameter excitation laser beam (separation distances are listed on the right of the plot).

Observation of the displacement waveforms in Figures 50, 51, and 52 shows a large, primarily monopolar, depression of the sample surface at the excitation epicenter, which is consistent with descriptions provided by previous authors[33-35,37,38]. As the probe is moved away from the epicenter (1mm and 2mm beam diameter measurements) a large initial upward displacement is observed followed by a negative displacement. In the 3mm beam diameter measurement this initial large positive "spike" is not observed. As the probe is moved further out from the epicenter a smaller positive displacement can be observed emerging from inside the depression in all of the measurements. This small displacement waveform begins to dominate as the probe/epicenter distance is increased causing the depression to be reduced. These localized displacement waveforms are due to a superposition of longitudinal, transverse/shear, and Rayleigh waves which, due to the short propagation distances from the epicenter, have not separated in time or distance[33].

Due to the amplitude differences in the previously shown cascaded plots of Figures 50-52, certain features of the waveforms, especially in the region where the smaller positive going displacement begins to emerge, is not evident. For this reason, the same data is presented in Figures 53, 54, and 55, at several source-receiver separations, with each separation point plotted in its own amplitude window.

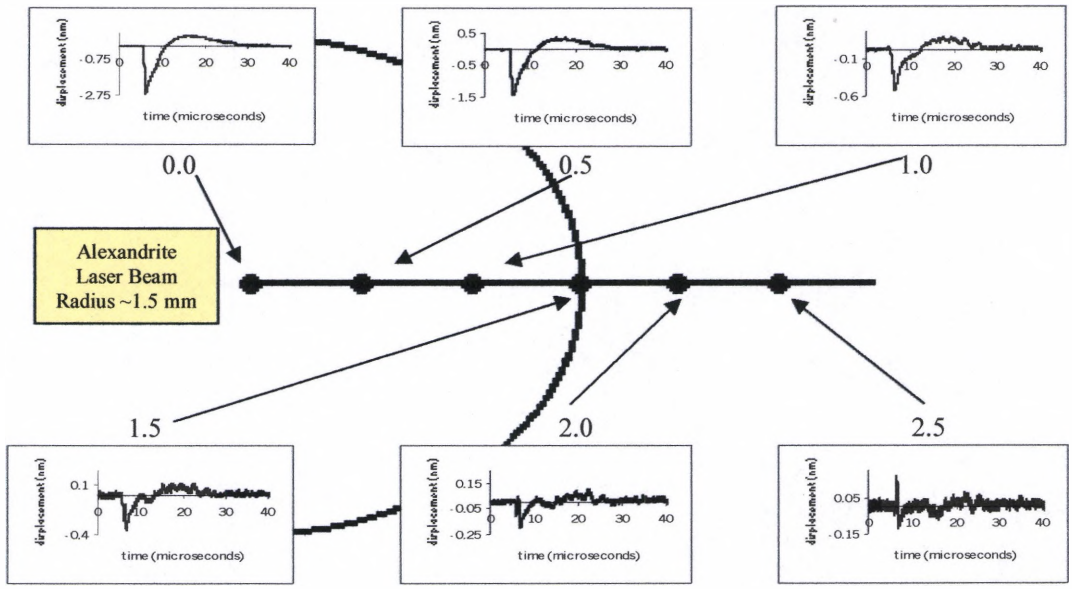

Figure 53 Interferometric displacement waveforms measured at different positions relative to the excitation beam epicenter for a 3mm diameter excitation beam.

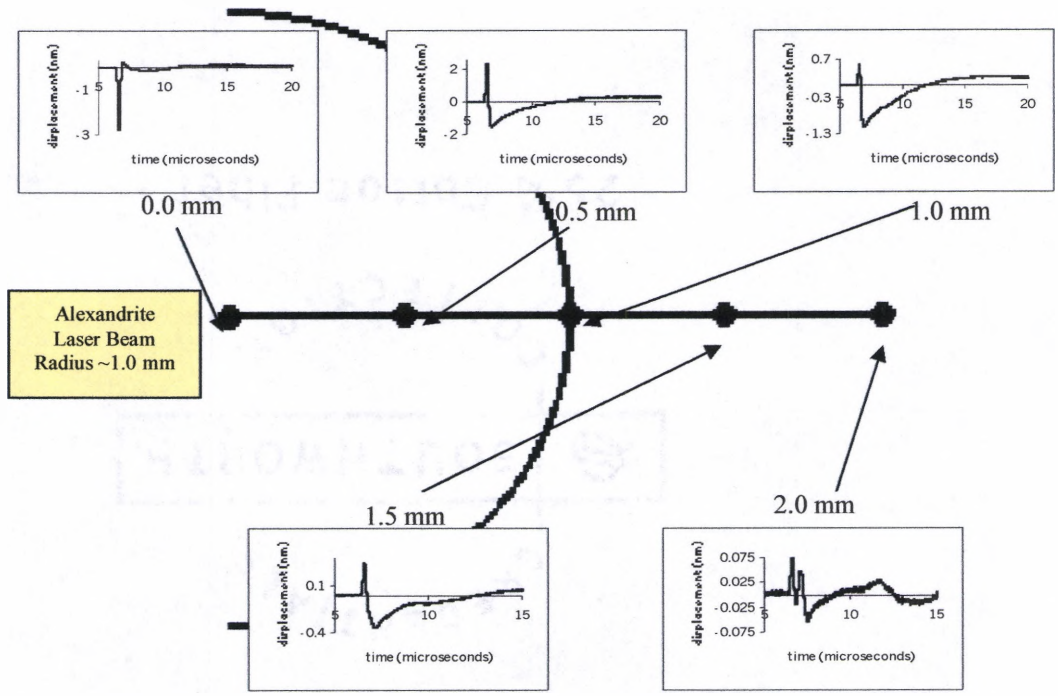

Figure 54 Interferometric displacement waveforms measured at different positions relative to the excitation beam epicenter for a 2mm diameter excitation beam.

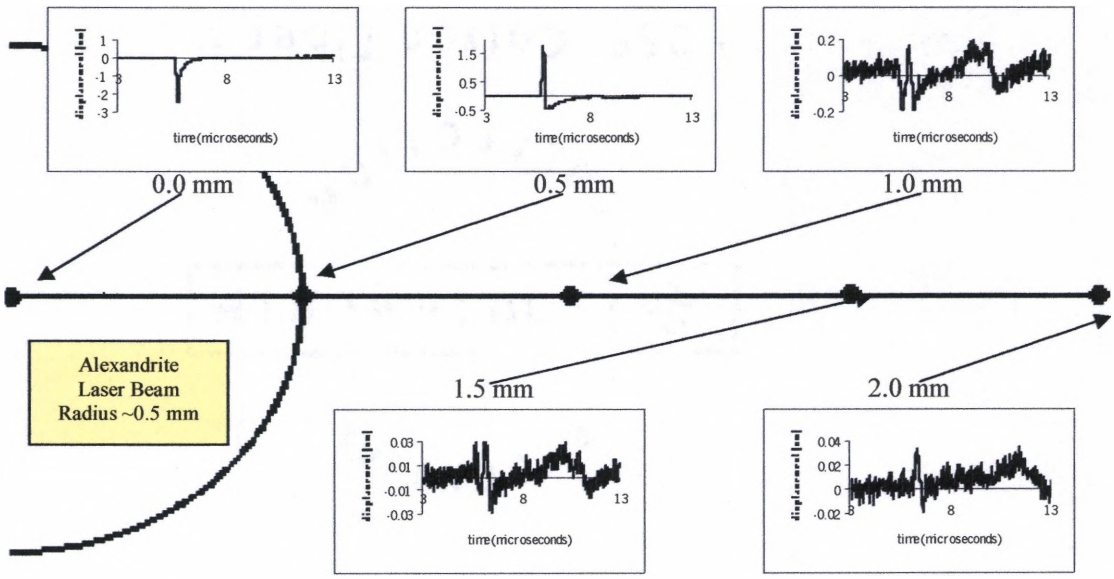

Figure 55 Interferometric displacement waveforms measured at different positions relative to the excitation beam epicenter for a 1mm diameter excitation beam.

4.2 MODIFICATIONS TO THE NUMERICAL MODEL

In light of the experimental waveforms displayed in Figures 50-55, an attempt to adjust the numerical model mentioned previously was undertaken. As was indicated in Chapter 2, the displacement waveforms obtained by the numerical model showed agreement with previous theoretical and experimental results obtained by Royer and Chenu[35] for a laser line source. However, comparison of the theoretical model to the near-field waveforms shown in the previous section shows a significant disagreement, specifically with the position in time of the emerging upward going displacement. A cascaded plot of the experimental waveforms, using the 3mm diameter excitation beam, is again shown in Figure 56.

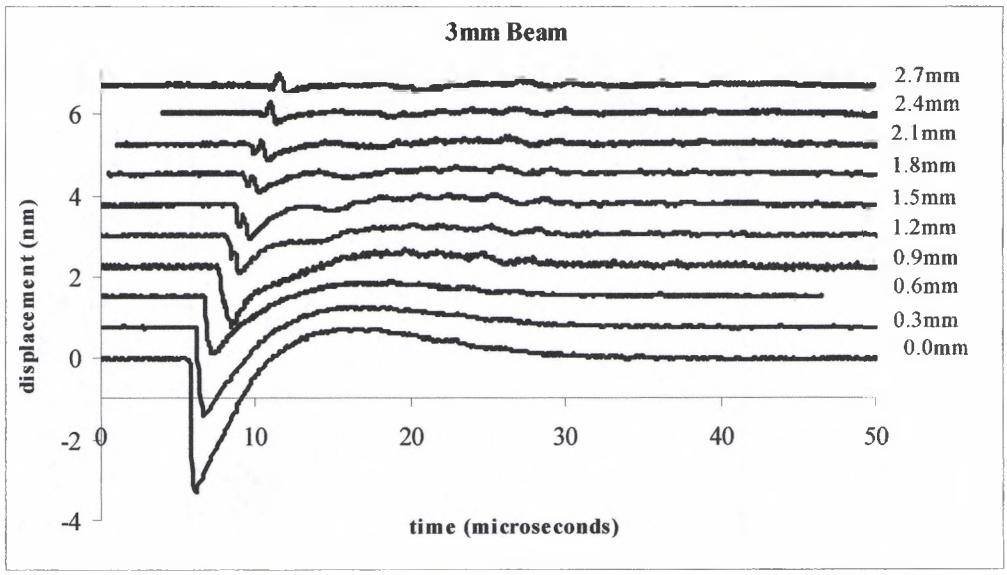

Figure 56 Measured waveforms at various source-receiver separations for the 3mm diameter excitation beam.

These measured waveforms show that as the broad upward displacement, which is visible at the source epicenter, decays with distance, the smaller, upward displacement emerges from within the negative depression, at an earlier relative time than is indicated by the theoretical model. This behavior was not observed in the work of Royer and Chenu[35] for the laser line source.

In the laser-line source modeled and measured waveforms[35] the width of the line source, in the observation direction x, was approximately of 0.4 mm in diameter. For the measured waveforms of Figure 56, a 3 mm diameter excitation beam was used for excitation. This variation in width, as well as the obvious shape difference, coupled with the use of pulse width of ~100 ns, compared to 40 ns for the line source data, may cause significant broadening of the initial downward pulse and thus, the secondary upward pulse appears to emerge from within this region.

Numerically, the superposition of SCOE point sources in the perpendicular y-axis direction, are taken into account by the equation df/dt given by Equation 32.

The superposition of line sources (of infinitesimal width) in the parallel x-axis direction are, however, taken into account by the summation or integration of the numerical program. While the precise numerical techniques used by Royer and Chenu[35] are not known, the technique used for the model presented here can be examined.

In the equation representing the summation of weighted and shifted line sources, namely

$$u(x,t)=\frac{2\Gamma M}{\pi\mu V_L^2}q(t)*\int_{-a}^{+a}w(X)\frac{\partial}{\partial t}f(x-X,t)dX \qquad \text{Eq. 53}$$

the primary quantity responsible for the resultant waveforms is the function df//dt, which is again

$$\frac{\partial f}{\partial t}=\frac{\sqrt{\pi}}{s_R a}\left[\delta(t-s_R x)+\frac{tL(\xi)}{s_R^2 a^2}H(t-s_R x)\right] \qquad \text{Eq. 54}$$

It is in this function (Equation 45) where a possible numerical error may occur.

In the model presented in Chapter 2, the delta function of Equation 54 is represented by a normalized Gaussian function of finite width. This finite width is used to ensure that, numerically, there exists a point where the function $\delta(t-s_R x)$ is nonzero. Obviously, as the width of the normalized Gaussian function approaches zero, a true delta function is approached. Numerically, however, using limited floating-point representation, the quantity $t-s_R x$ may not equal precisely zero depending on the time intervals and parameters used in the simulation. Thus, in representing the Delta function by a Gaussian function, a difficulty arises in the temporal positioning of the waveform components given by the previously mentioned equations D(x,t) and H(x,t), where

$$\frac{\partial D}{\partial t} = \frac{\sqrt{\pi}}{s_R a}\left[\delta(t - s_R x)\right] \qquad \text{Eq. 55}$$

$$\frac{\partial H}{\partial t} = \frac{\sqrt{\pi}}{s_R a}\left[\frac{tL(\xi)}{s_R^2 a^2}\widehat{H}(t - s_R x)\right] \qquad \text{Eq. 56}$$

In a true delta function, the quantity of Equation 55 is only nonzero at precisely $t = s_R x$, and in Equation 56, the function starts at $t = s_R x$. When the delta function is represented as a Gaussian however, the maximum occurs at $t = s_R x$ while the precise start, where the function is zero, is at $-\infty$. A plot of both Equations 55 and 56 can be seen in Figure 57 at a distance of 3a/2 from the source center.

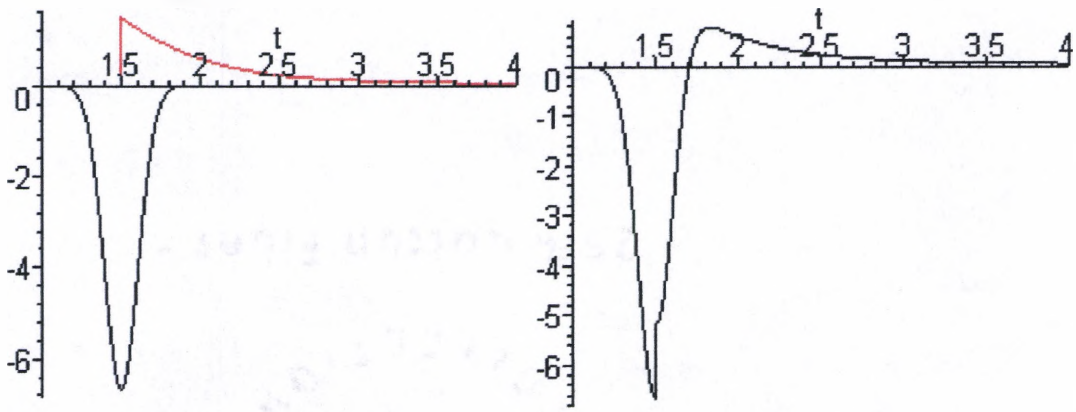

(a) (b)

Figure 57 Time derivatives of D(x,t) and H(x,t) functions where D(x,t) is a normalized Gaussian both (a) separately and (b) combined.

Figure 57 shows that the H'(x,t) function begins at the maximum of the Gaussian distribution. Using this formulation, the modeling results of Chapter 2, were obtained. Since the true delta function and the Heaviside Function, for practical purposes, become non-zero at the same instance, an assumption that a temporal

shift in one of the components can be made. If the start of the Gaussian distribution is taken to be the 1/e value, and with representation being

$$\delta(t) = \underset{w\to 0}{Lim}\frac{1}{w\sqrt{\pi}}\exp\left(\frac{-t^2}{w^2}\right) \qquad \text{Eq. 57}$$

then a shift, earlier in time, of the H function by w can be made

$$\frac{\partial H}{\partial t} = \frac{\sqrt{\pi}}{s_R a}\left[\frac{tL(\xi)}{s_R^2 a^2}\hat{H}(t - s_R x)\right] \Rightarrow \frac{\sqrt{\pi}}{s_R a}\left[\frac{tL(\xi)}{s_R^2 a^2}\hat{H}(t - s_R x + w)\right] \qquad \text{Eq. 58}$$

Using this shifted function, the plots of Figure 57 are reproduced in Figure 58.

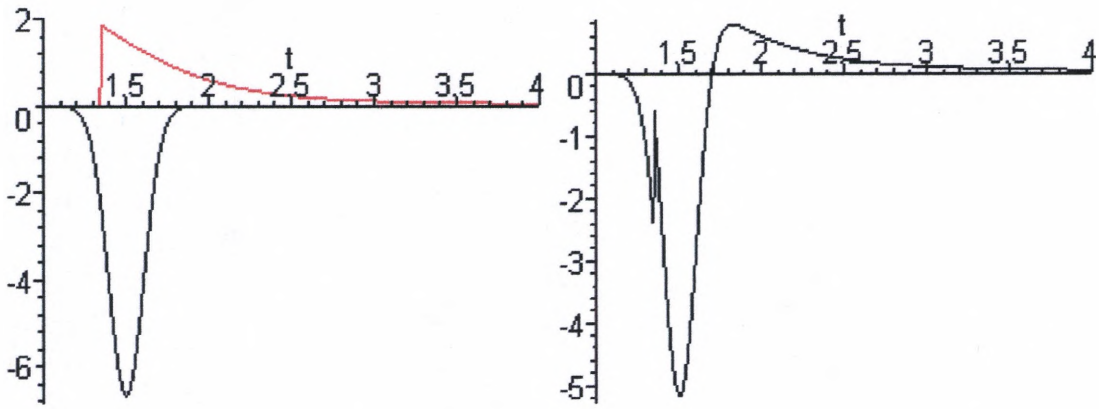

(a) (b)

Figure 58 Time derivatives of D(x,t) and H(x,t) functions where D(x,t) is a normalized Gaussian and H(x,t) is shifted by the half-width of D(x,t) for both (a) separate and (b) combined.

It can now be seen using this temporal shift that a sharp peak emerges from within the depression. Using this shifting technique, the entire displacement (Equation 53) was re-evaluated and is displayed along with measured waveforms in Figure 59.

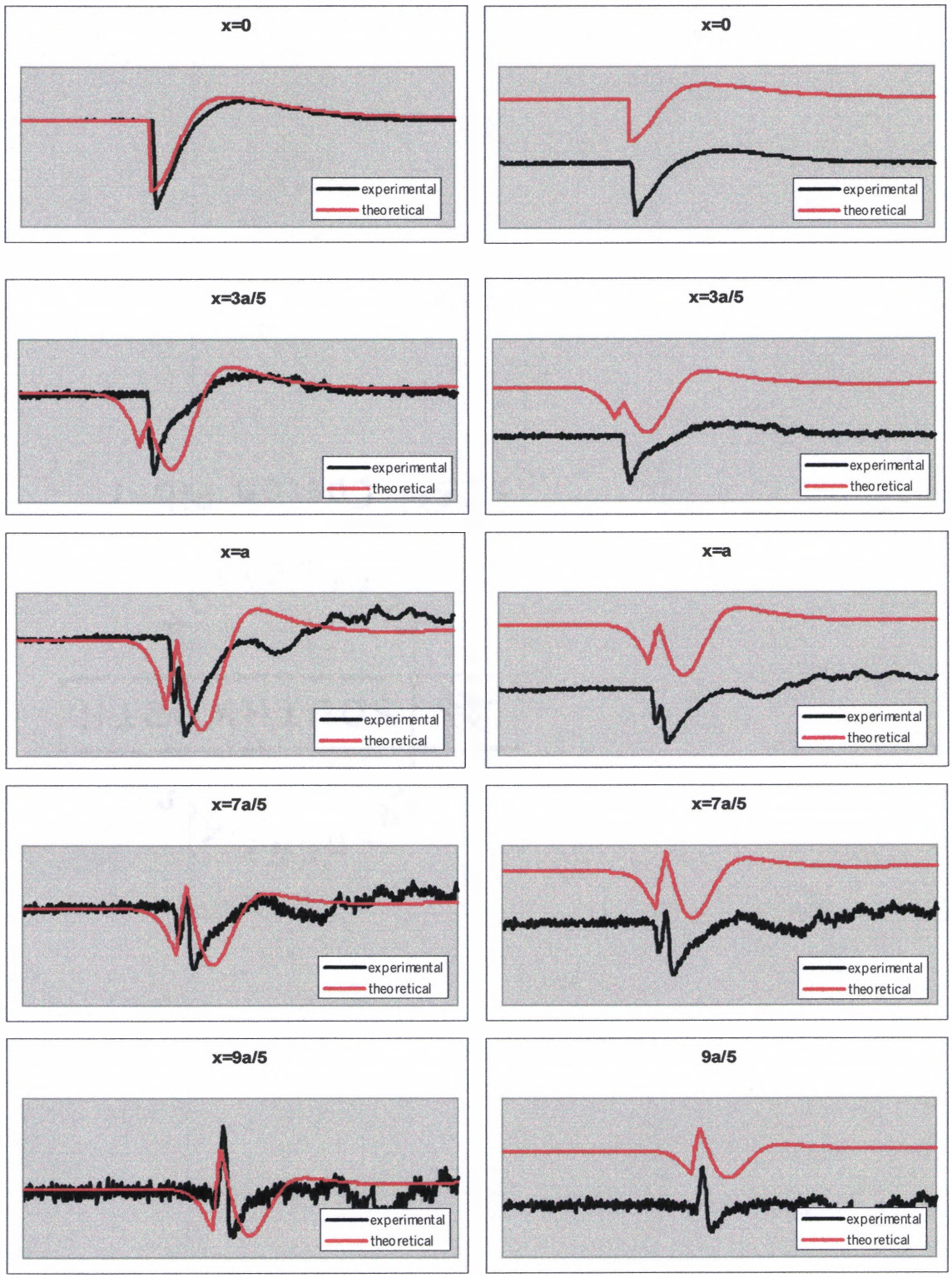

Figure 59 Experimental and theoretical waveforms at various source-receiver separations displayed in both overlap (left) and offset (right) forms.

The comparison of experimental and theoretical waveforms shown in Figure 59 indicates that the presence of this temporal shift does indeed produce waveforms which are more agreeable with those observed experimentally. While the present state of this numerical model uses arbitrary parameters, future work to develop a more complete model, which uses actual parameters, could benefit from the above experimental results and numerical modeling considerations.

4.3 NEAR-FIELD INTERACTION WITH FREE-BOUNDARIES

In order to study the ultrasonic wave/free-boundary interaction process for a laser generated ultrasonic SAW, a stationary excitation beam (3 mm in diameter) from the alexandrite laser was placed 10 mm from the edge of a polished titanium sample. For this measurement, the laser power density incident on the sample was set to 0.35 MW/cm². The detection laser beam was positioned at the excitation source epicenter, and was systematically translated towards the edge while capturing, point-by-point, 100 signals and storing the average onto a digital oscilloscope. A schematic of this measurement is shown in Figure 60.

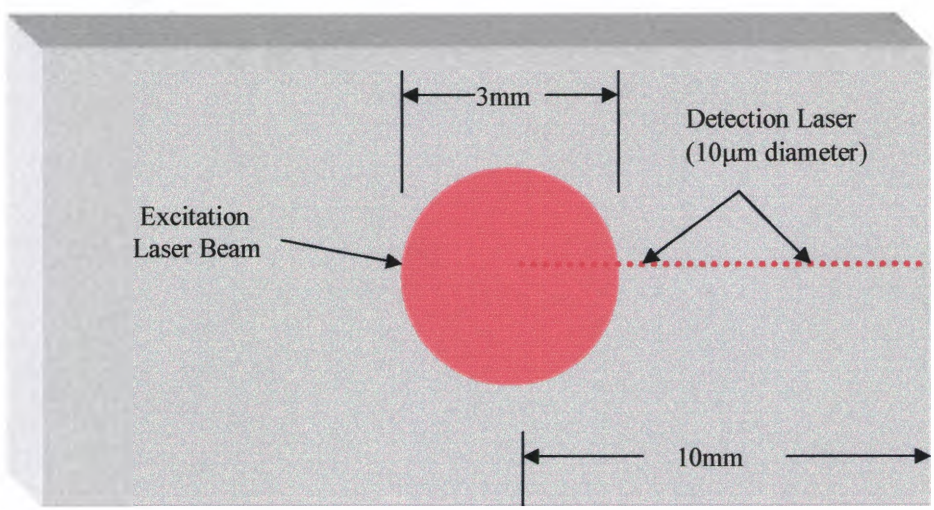

Figure 60 Schematic of SAW/edge interaction measurement.

The captured displacement waveform signals are presented in Figure 61 for both displacement vs. time (with spatial steps progressing vertically), and displacement vs. position (with time steps progressing vertically). In Figure 61a, the signals captured at each position are shown progressing vertically. Thus, the lowest trace is when the detector is at the excitation source epicenter and the highest trace is at the edge. Observation of these plots shows a smaller vertical displacement emerging from within the larger source depression and eventually becoming the dominant waveform. As the detector moves closer to the edge, this waveform, as well as the reflected waveform can be observed. When the detector moves to the edge, this incident and reflected wave begin to overlap in time and eventually superimpose where an intensification of the measured displacement at the edge is observed.

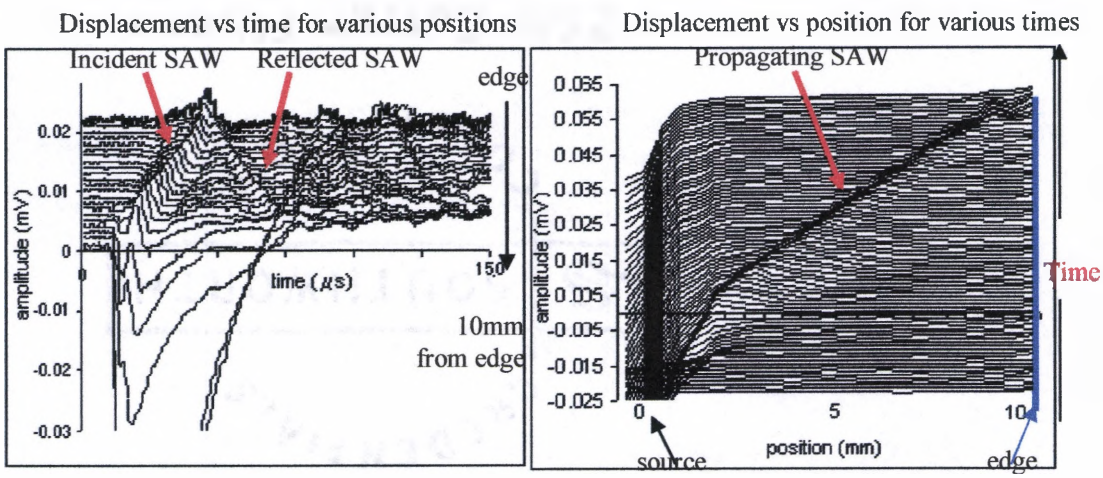

Figure 61 a) Plots of displacement vs time at positions approaching the edge in 0.5mm increments, and b) the same data, plotted as displacement vs. position at increasing time steps.

Using the same data set, a plot of the displacement vs. position at increasing time steps was generated, and this is shown in Figure 61b. Analyzing the data in this manner allows for a different visual representation of what is occurring on the sample surface. Although the actual spatial steps are rather course, 0.5mm/step, this plot shows the material surface is at its zero motion position until the arrival of the pulse, which results in a dramatic depression of the surface (mainly cut off to put emphasis on traveling wave). As time progresses from this initial pulse arrival (increasing time depicted vertically in Figure 61b), a propagating wave emerges from this source and travels towards the edge (right on the plot). By analyzing the data in this spatial instead of time manner, a grey scale sequence of images can be produced to represent this phenomena (Figure 62).

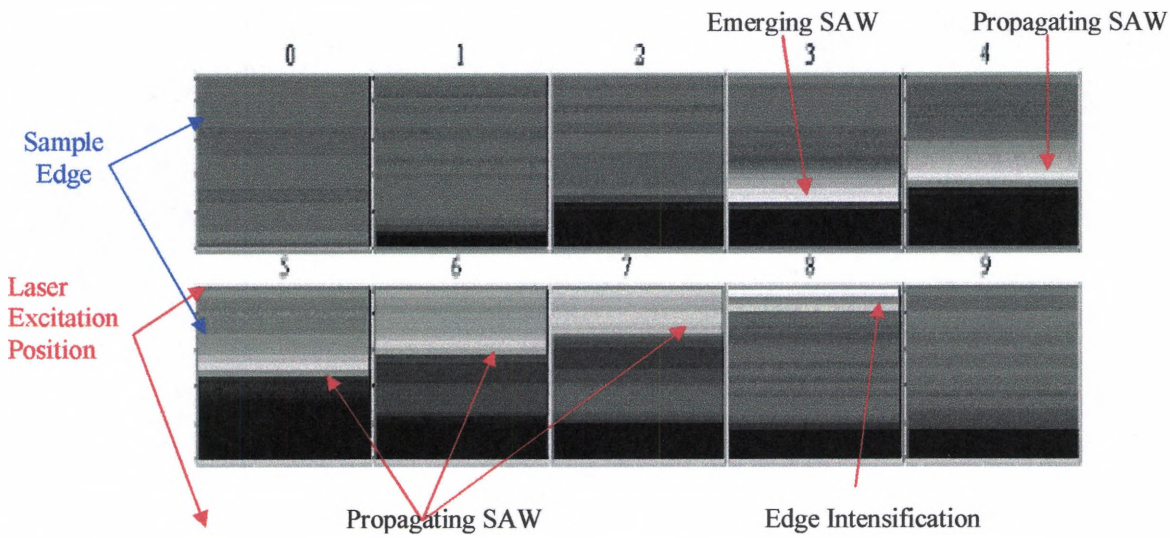

Figure 62 One-dimensional time sequence of displacement vs. position images.

The sequence of pseudo-images depicted in Figure 62, although only representative of a one-dimensional measurement, clearly show that the arrival of the laser pulse (frame 1 and 2) causes a depression of the surface which is represented by the black portion at the bottom of the figure. As time increases (frames 3-7) a positive displacement can be seen emerging from the depression and

propagating, vertically in the figures, towards the edge. At frame 8, this traveling wave reaches the edge where it is intensified (becomes brighter).

Contrary to traditional ultrasonic methods, which utilize contact transducers for the generation of ultrasound, the laser generation of ultrasound allows for the source itself to be scanned across a material surface. It then becomes desirable to investigate the interaction of this thermoelastic source with a free-boundary and how this interaction differs from that of a stationary source where traveling waves interact with a boundary. For this comparison, a 1mm diameter excitation beam is used. The excitation beam is, as before, originally positioned 10 mm from the edge of a titanium sample. In each measurement the detection laser beam is originally placed at the epicenter of the thermoelastic source. In the first measurement (Figure 63a) the source is kept stationary and the detection beam is scanned towards the edge. For the second measurement (Figure 63b) the detector is kept stationary and the generation beam is scanned towards the edge. For both cases, 100 signals were captured, averaged, and stored at each position.

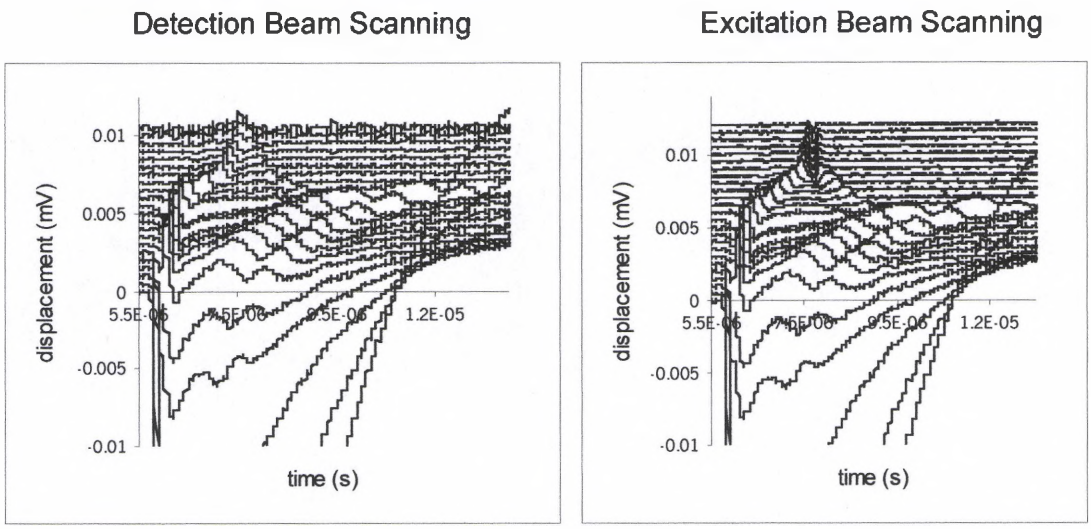

Figure 63 (a) Displacement vs. time for successive positions approaching the edge. (b) Displacement vs. position for successive time steps.

The waveforms shown in Figure 63 indicate a different behavior of the surface displacement approaching the edge depending on whether the detection or excitation beam is scanned. To further emphasize this unique behavior, the same data showing only the portion in the immediate vicinity of the edge, is presented in Figure 64a and Figure 64b. From these figures it becomes more evident that the detection laser approaching the edge, monitoring the SAW's emanating from a stationary source, detects positive surface displacement intensification. In the other case, as the source approaches the edge, the stationary interferometric probe detects a negative intensification which appears to occur before the edge and then decays at the edge.

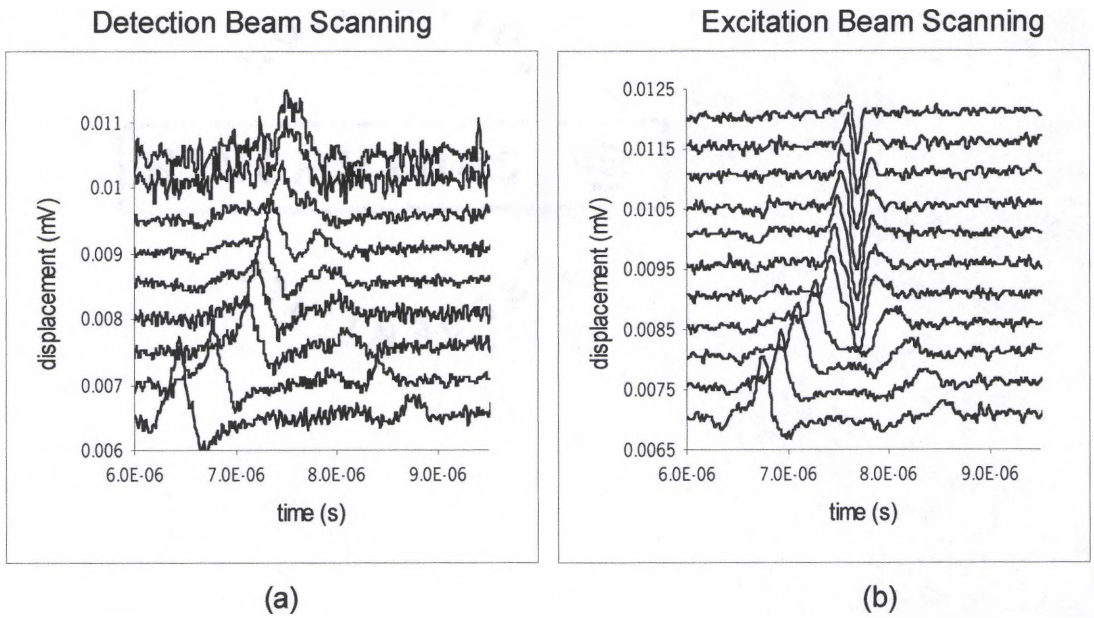

Figure 64 (a) Displacement vs. time for successive positions close to the edge. (b) Displacement vs. position for successive time steps close to the edge.

Analysis of these measurements, in terms of the intensification at the edge, requires some manipulation due to the initial starting position of the detector relative to the source. As was seen previously in the near-field of the thermoelastic source,

the displacements detected when the source-receiver separation is small results in near-field waveforms which are much greater in amplitude at the center, and decay dramatically as this separation is increased. For analytical comparison, this natural decay was removed according to an $r^{-\gamma}$ data fit, where r is the beam seperation and γ is used as a variable near-field decay constant in accordance with ref [33]. An example of this data fit and decay removal can be seen in Figure 65 for the case of the detection laser scanning and the source stationary. Using this decay removal technique, the relative peak-to-peak intensifications for both the detector scans only and the source scanning only, is shown in Figure 66.

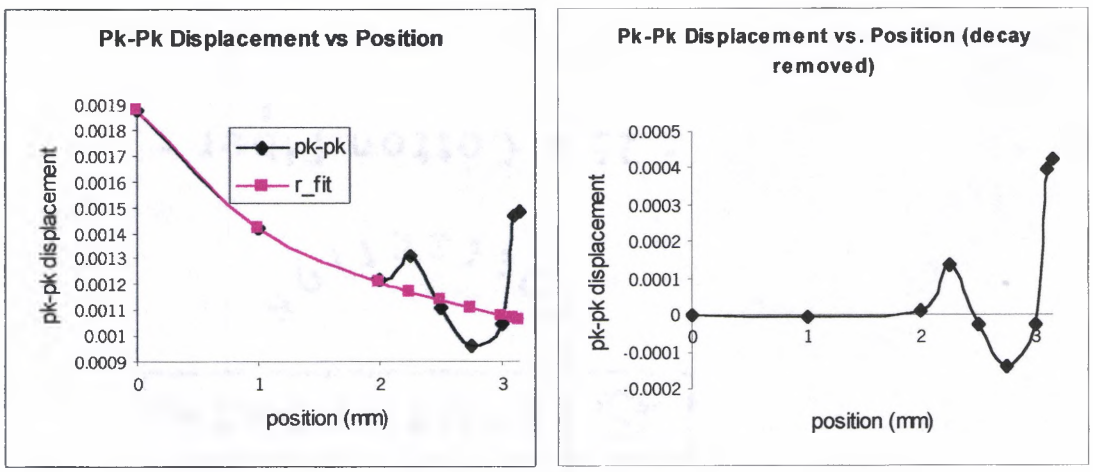

(a) (b)

Figure 65 (a) The peak-to-peak displacement vs. position for the detection beam scanning towards the edge and the decay data fit. (b) The peak-to-peak displacement vs. position with this decay removed.

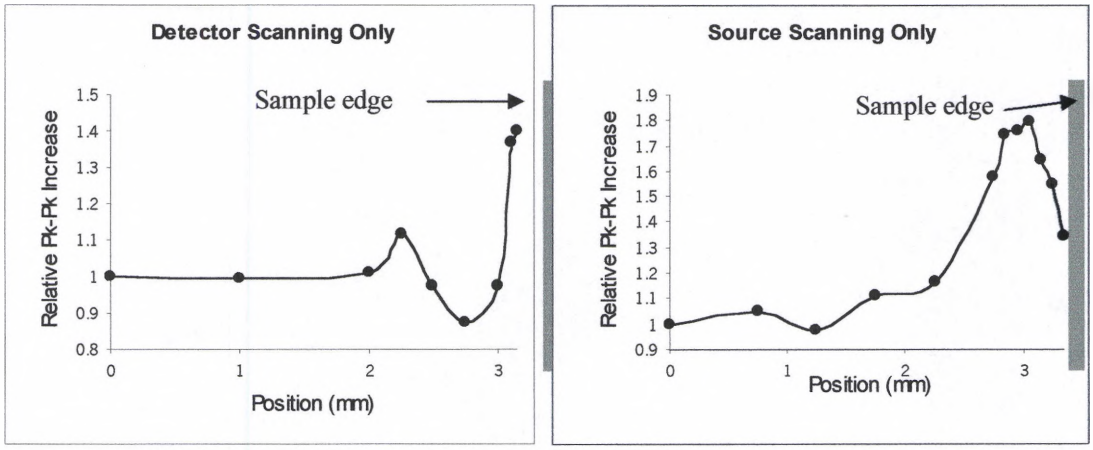

(a) (b)

Figure 66 (a) Relative peak-to-peak intensification vs. position for the detector scanning. (b) Relative peak-to-peak intensification vs. position for the source scanning.

Viewing the relative peak-to-peak intensifications shown in Figure 66, the unique behavior of each case (source or receiver scanning) becomes clear. The behavior of this near-boundary intensification for a stationary source and a scanning detector is primarily an intensification which is a maximum at the edge of the sample. This result is similar to that of the NFSI technique which involved a similar experimental method. For the measurement with the source scanning and the detector stationary, the intensification is seen to be broader and peaking before the edge and decreasing again at the edge. This result is similar to those reported using the SLS method which again, utilized a similar experimental configuration.

While both measurements shown above produce an intensification at a boundary (in this case an edge), there are additional considerations which need to be considered for crack imaging purposes. Clearly, the measurement in which the excitation beam is scanned towards the edge produces not only a broader intensification but also one which does not occur precisely at the edge. The effect of

this broadening and offset intensification will amount to lower resolution and precise location difficulties when images are produced. The measurement in which the detection beam is scanned towards the edge does produce a sharper and ideally located intensification, however, in both these single beam scanning techniques, the natural near-field decay requires additional data manipulation to truly isolate the intensification which occurs at a boundary that is some distance away from the large amplitude thermoelastic near-field.

4.4 DUAL BEAM SCANNING AND THE EFFECTS OF SPOTSIZE AND BEAM SEPARATION ON THE RELATIVE FREE-BOUNDARY INTENSIFICATION

In addition to the two measurement configurations discussed in the previous section, a third measurement option involves scanning both the generation and detection beams together at a fixed distance from one another. The availability of this dual scanning configuration provides a remedy for the problem of the near-source decay, which was observed in the previous measurements, where only one beam was scanned. As a result, the amplitude of the detected surface displacement should remain constant, provided the area over which the beams are scanned is uniform and free of defects. Using this method, therefore, any change in the detected signal should be due to a direct change in the material properties. Thus for imaging capabilities the additional data processing of fitting a decay curve can be omitted from the signal analysis.

For this dual-beam system, where both excitation and detection lasers are scanned towards the edge of a polished titanium material sample (2.5cm x 1cm x10cm), the source receiver separation was kept at a fixed distance while the sample was scanned under the beams (Figure 67). The detection beam was placed 3mm from the center of a 3mm diameter excitation beam, and the detection beam was positioned closer to the edge during the scan. The results of this scan (Figure 68)

show a relative peak-to-peak displacement intensification at the edge of approximately 2x, compared to the nominal peak-to-peak displacement level away from the edge.

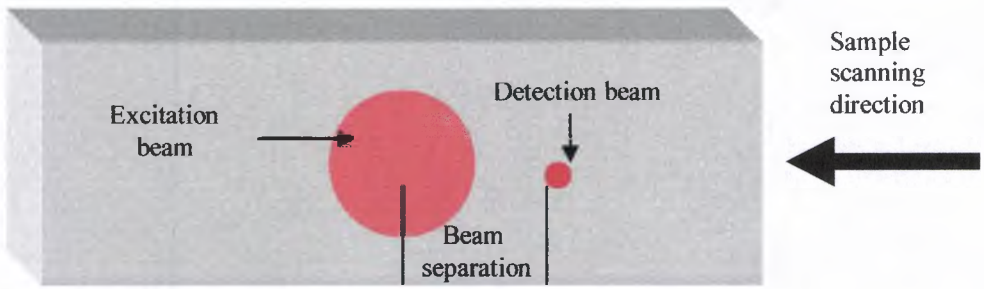

Figure 67 Beam placement and sample scanning direction for dual beam scanning system.

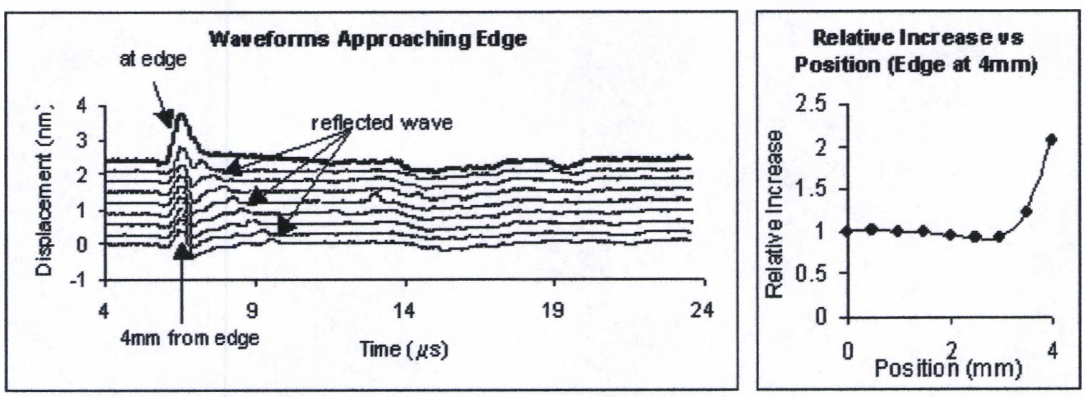

Figure 68 (a) Waveforms approaching the edge for the dual beam scanning system. (b) Relative pk-pk intensification approaching the edge.

From Figure 68a, it can be seen that the initial waveform seen 4mm from the edge does not change dramatically in shape or amplitude until the system is very near the edge of the sample. The only significant change in the signal, before the intensification, is the shift in time of the reflected wave as the beams approach the edge. At the edge, the superposition of the reflected and incident waves as well as

the intensification of the signal can be observed. The relative intensification (Figure 68b) is seen to be similar to the measurement where the source is left stationary. Due to the lack of natural near-field decay, however, the result was obtained without the complication of fitting a decay curve.

To examine the effects of source/receiver separation and excitation beam spotsize on the near-field displacement intensification levels for this dual beam scanning system, a systematic investigation was carried out. In each measurement, the beams were scanned towards the edge using various generation and detection laser separation distances. The effect of this dual laser beam system approaching the edge on the detected waveforms for the 3mm beam can be seen in Figures 69 through 75. These cascaded plots show the waveforms detected by the laser interferometer at various positions relative to the edge. The positions corresponding to the displayed waveforms are, starting with the lowest waveform and progressing vertically, 5.0, 3.0, 2.0, 1.5, 1.0, .8, .7, .6, .5, .4, .3 .2, .1, and 0mm from the edge, with the highest waveform representing the detector at the edge.

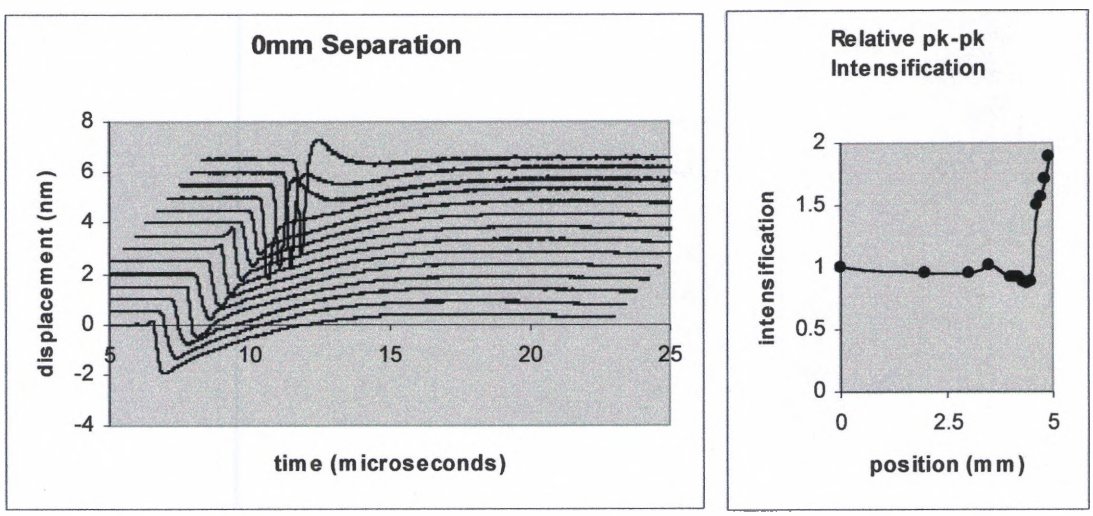

Figure 69 (a) Waveforms approaching edge and (b) relative pk-pk intensification with the receiver at the source center.

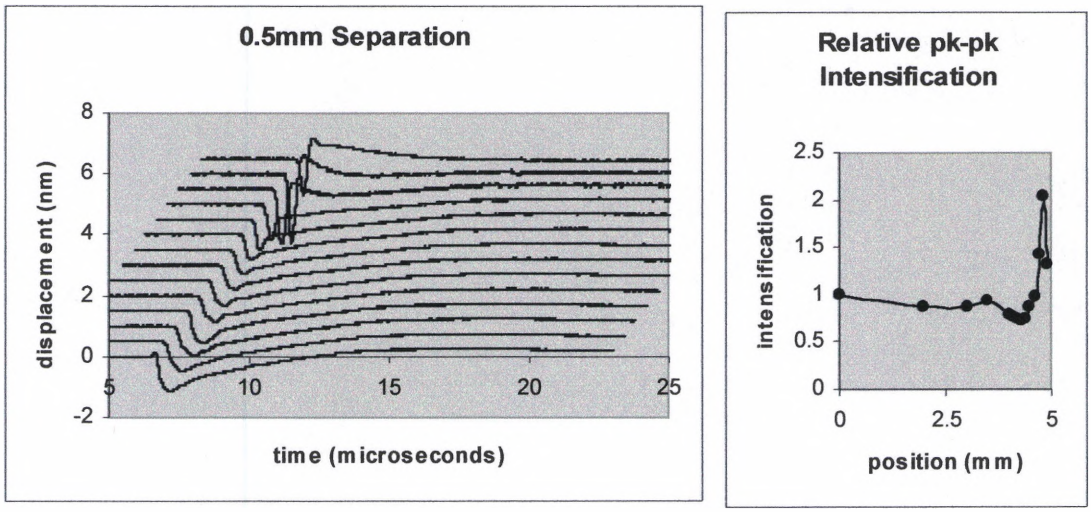

Figure 70 (a) Waveforms approaching edge and (b) relative pk-pk intensification with a source-receiver separation of 0.5mm.

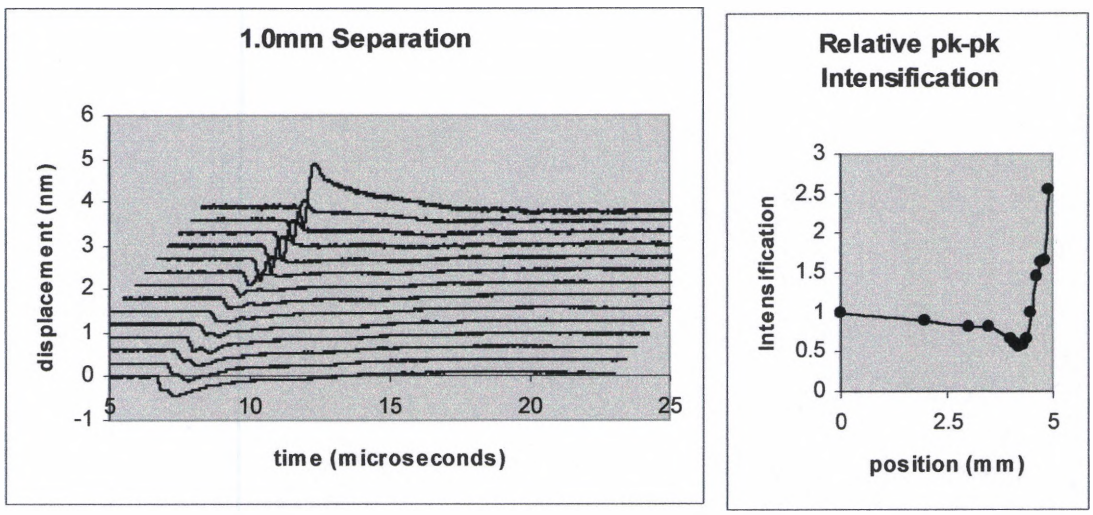

Figure 71 (a) Waveforms approaching edge and (b) relative pk-pk intensification with a source-receiver separation of 1.0mm.

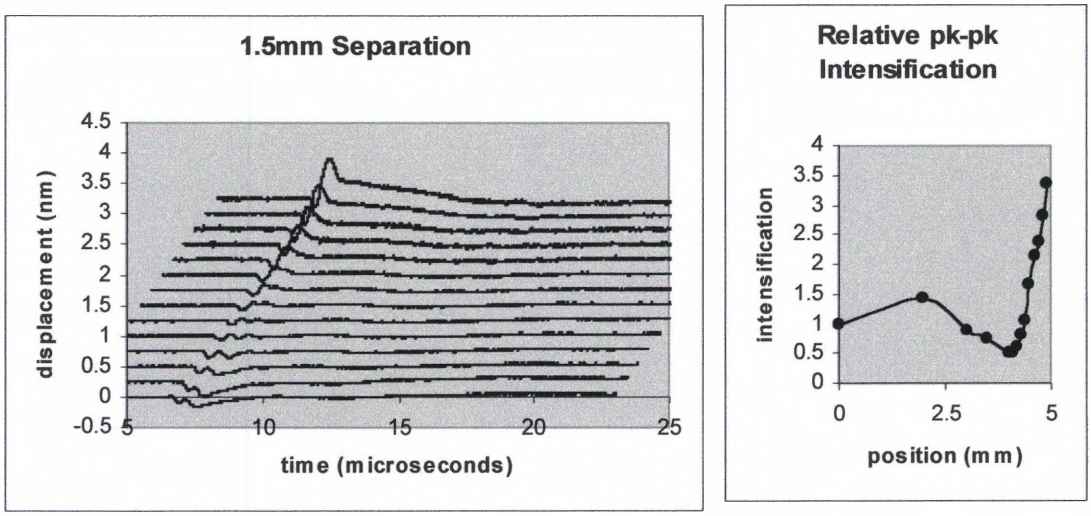

Figure 72 (a) Waveforms approaching edge and (b) relative pk-pk intensification with a source-receiver separation of 1.5mm.

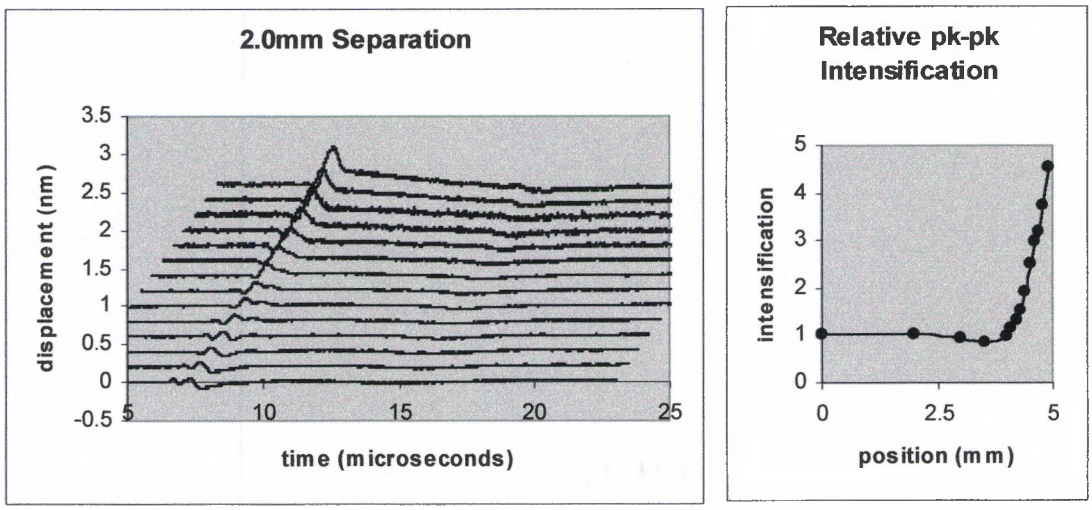

Figure 73 (a) Waveforms approaching edge and (b) relative pk-pk intensification with a source-receiver separation of 2.0mm.

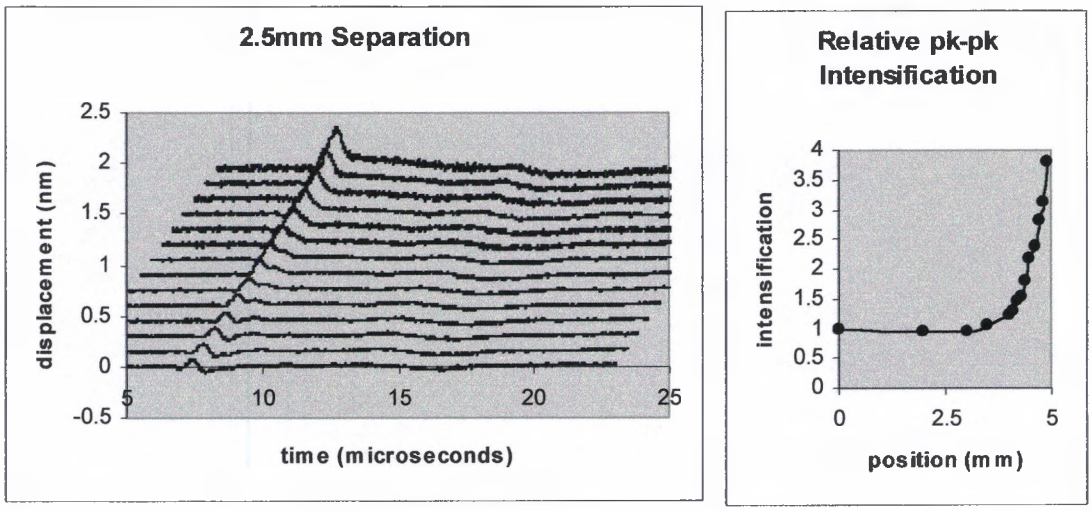

Figure 74 (a) Waveforms approaching edge and (b) relative pk-pk intensification with a source-receiver separation of 2.5mm.

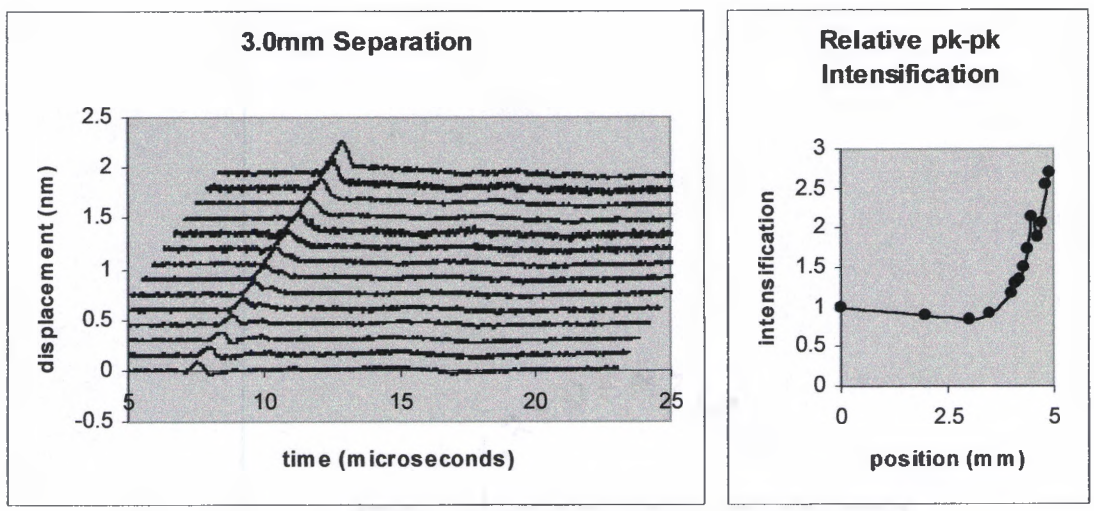

Figure 75 (a) Waveforms approaching edge and (b) relative pk-pk intensification with a source-receiver separation of 3.0mm.

The intensification vs. position analysis carried out for these measurements indicated that although the largest absolute magnitude peak-to-peak signal occurs when the detection beam is at the source epicenter, the largest relative intensification does not occur at this position. Because of image contrast arguments, the relative amplitude increase is actually more important for imaging cracks. From the measurement results, the largest relative increase occurred at a beam separation of 2.0mm. In these waveforms it is clear that although the 0.0mm separation displays a large intensification, compared to its original magnitude, the relative increase is not as dramatic as the 2.0mm separation which, at 5mm away from the edge is very small.

In order to understand the effect generation beam spotsize, the above measurement and analysis was repeated for both a 2mm and 1mm diameter excitation beam. The results of these measurements, plotted in terms of the peak-to-peak intensification vs. beam separation for all three spotsizes, are shown in Figure 76.

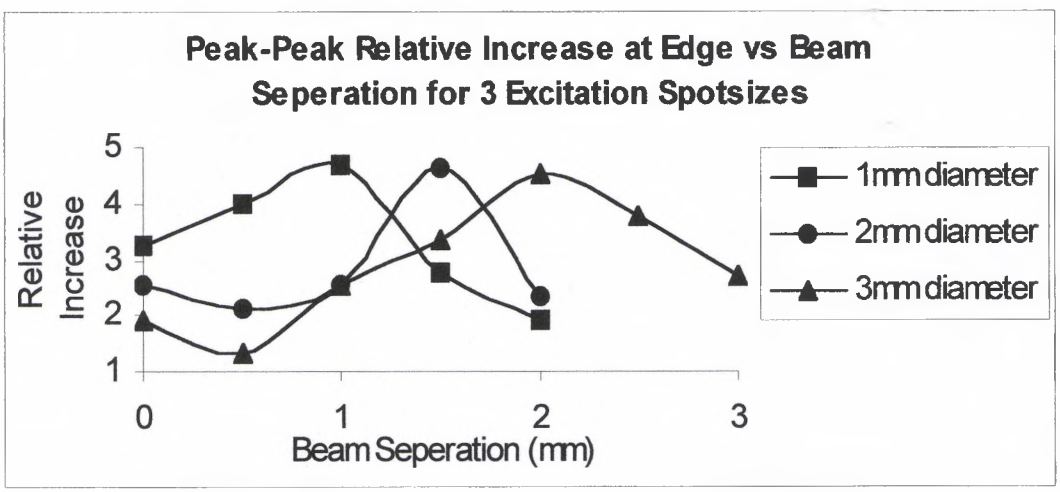

Figure 76 Relative increase of peak-to-peak surface displacement at edge versus surface displacement several mm away from edge.

The measurements indicate an optimal beam separation which varies dependant on the excitation laser spotsize. Although the beam separations measured could be refined by taking smaller interval steps, in each case the optimum separation, as indicated by Figure 76, occurs when the detection laser is placed at a position approximately 0.5 mm beyond the excitation beam radius. Thus, for this dual beam scanning system, in order to obtain the highest contrast between a uniform surface and a surface defect, the detection beam should be placed somewhere just outside the excitation laser beam.

In light of the previous results, a comparison can now be made between the variations in scanning technique (ie. scanning one or both beams). Figure 77 shows the comparison, for the case of a 1mm diameter excitation beam, for the three scanning techniques. From this comparison it becomes evident that scanning both excitation and detection beams at a fixed and optimized separation produces a relative intensification at a free-boundary which exceeds that of either single-beam scanning configuration.

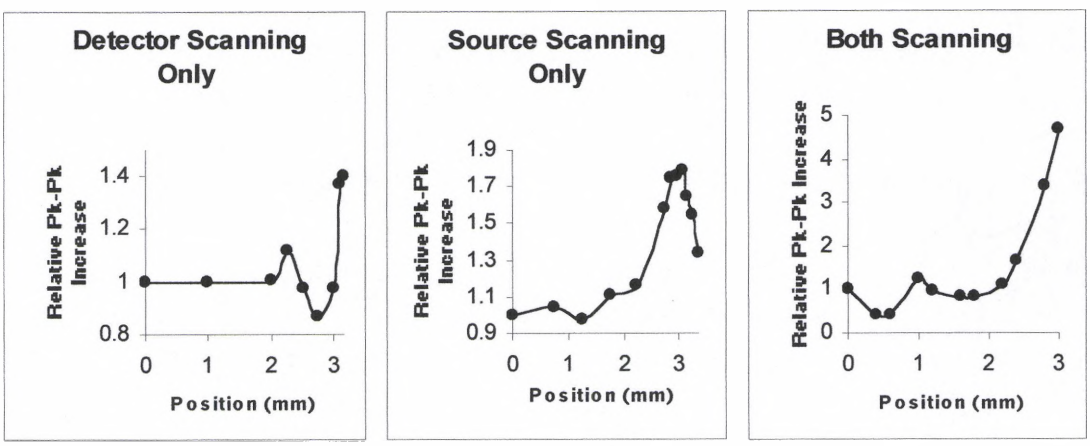

Figure 77 Comparison of scanning techniques for 1mm beam.

In order to validate the conclusions derived from measurements conducted at the ideal free-boundary (a sample edge), the previous measurements were also carried out using a through-the-thickness crack in an Aluminum sample. The excitation beam diameter used was 3mm and the laser power density incident on the sample was approximately 0.1MW/cm². The positioning of the beams and the direction of the scan are shown in Figure 78. The beam separation was varied from 0mm to 3mm in 0.2mm intervals and the beams were scanned towards the edge in 0.05mm increments. The relative pk-pk intensification observed as the detection laser beam approaches and crosses the crack are shown in Figure 79 and the actual waveforms both away from the crack and at the crack are shown in Figure 80.

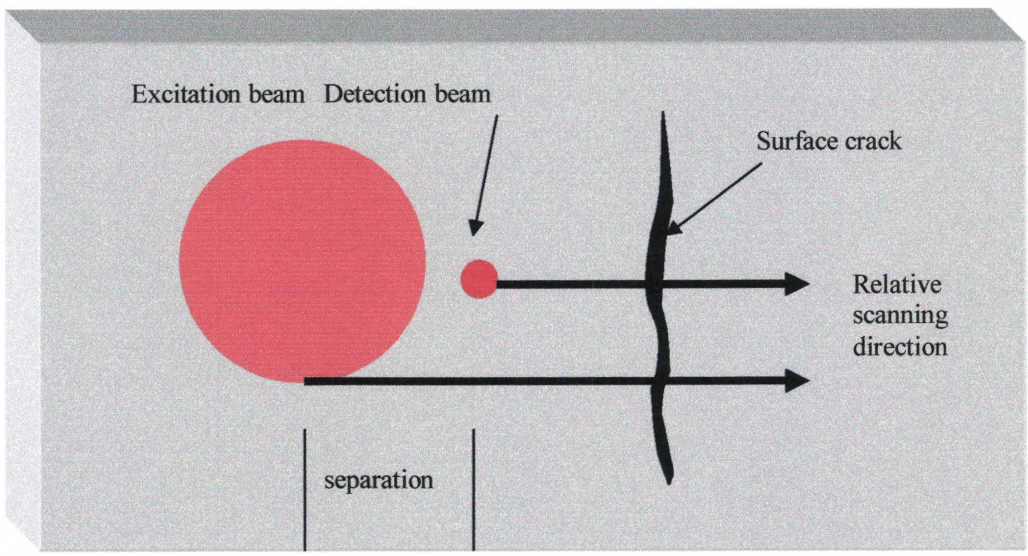

Figure 78 Diagram of scanning system configuration. Arrows show the relative motion of beams while the stage is scanned in the opposite direction.

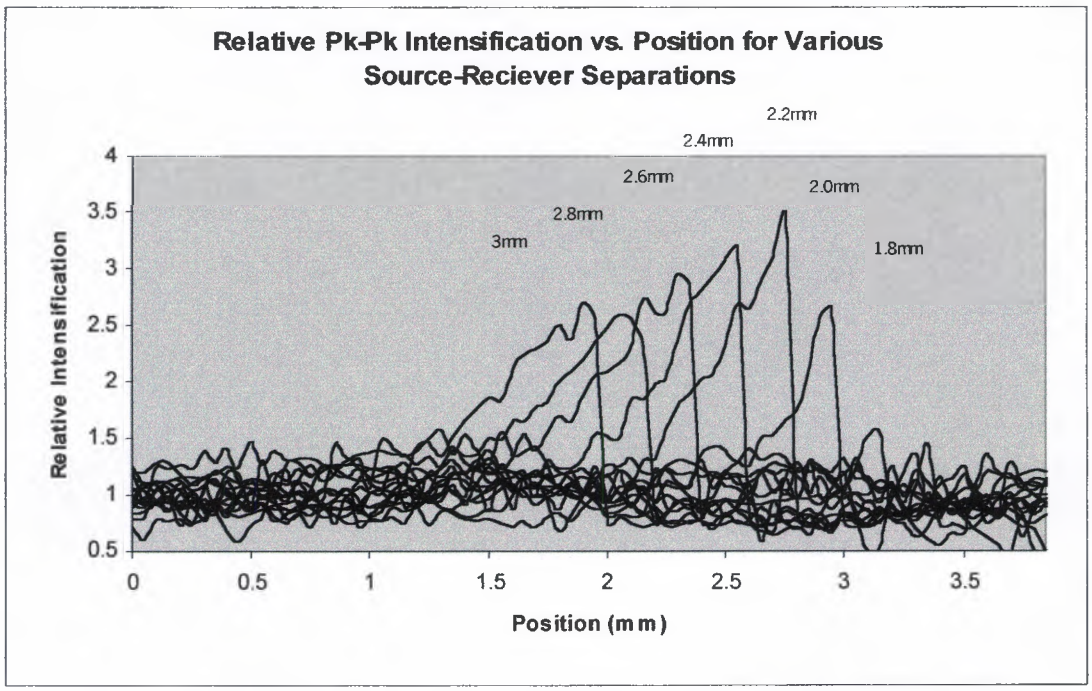

Figure 79 Relative intensification vs. position approaching a surface-breaking crack for various source-receiver separations.

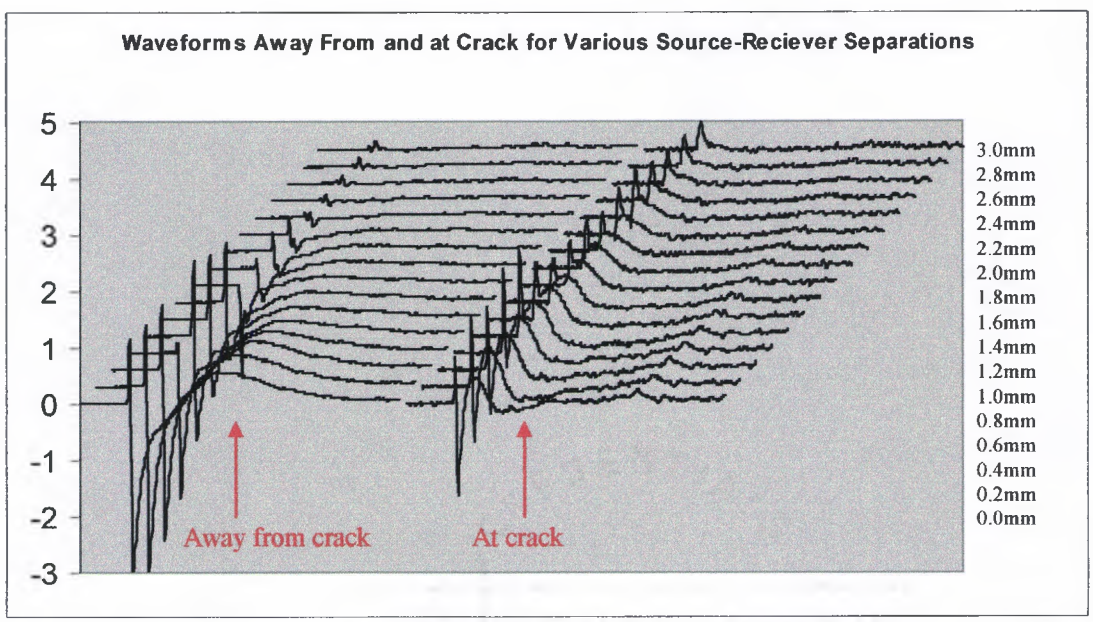

Figure 80 Comparison of waveforms away from and at a surface-breaking crack for various source-receiver separations (separations are listed on the right).

By viewing the waveforms of Figure 80, it can clearly be seen that although the waveform observed at the crack using the 0mm separation is the largest in magnitude, so to is the waveform away from the crack and thus the quantity of interest, the relative intensification, is not optimal at this separation. It can also be noted that there is a decay of amplitude with increasing separation in both the waveforms away and at the crack. The behavior of both of these decays (their respective rates of decay) is what leads to the existence of an ideal separation. This can be seen in Figure 81 where the amplitude decay of the waveforms away from the boundary, at the boundary, and the respective relative intensifications can be seen for both the crack measurements as well as the previous measurements conducted at the sample edge.

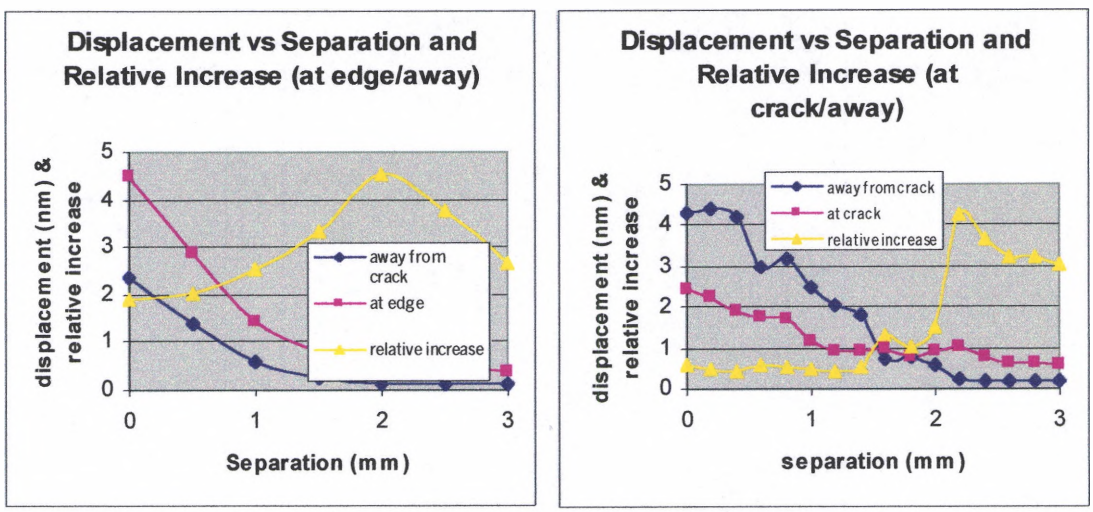

(a) (b)

Figure 81 Decay of fields with separation both away and at the boundary along with relative intensification for both the (a) crack measurements and (b) edge measurements.

A more direct comparison of the edge measurements and the crack measurements can be seen in Figure 82.

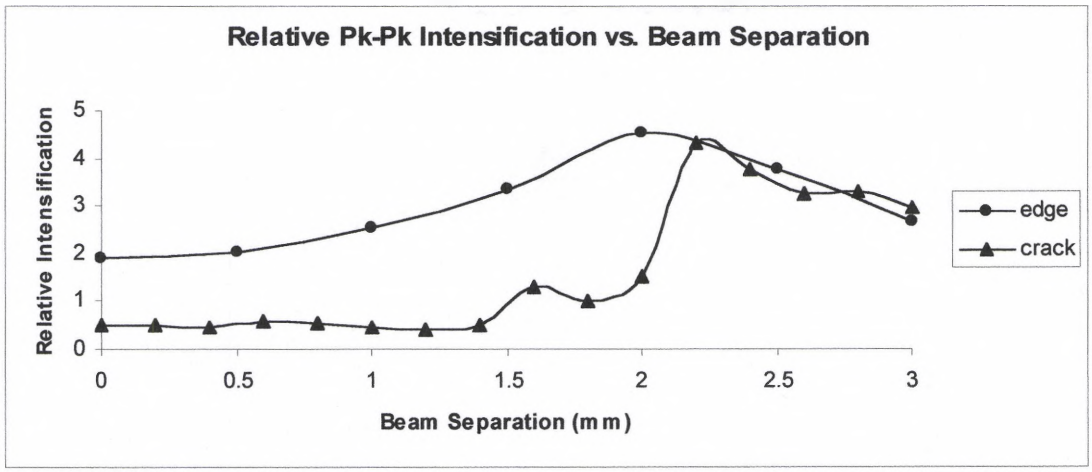

Figure 82 Comparison of edge and crack intensification vs. Separation data for 3mm diameter beam.

This comparison shows that both measurements at an edge, as well as data obtained using a surface crack, indicate an ideal source-receiver separation in a region within 1mm outside the excitation laser beam radius.

4.5 TWO-DIMENSIONAL DUAL-BEAM SCANNING AND THE REDUCTION OF NOISE IN CRACK IMAGING MEASUREMENTS

The measurements discussed in the previous sections were all made for the purpose of achieving the primary goal of this research, crack imaging. Having determined the ideal source/receiver positioning for this dual-beam scanning system, two-dimensional scanning of both beams, in an effort to monitor SAW displacement levels point-by-point over a sample, will now be discussed. As will be shown, clear images of surface-breaking cracks, using this technique, is accomplished using a time-gated analysis program which has been developed for the purpose of reducing waveform noise in crack imaging measurements.

In the following experiments, the source/receiver separation was set to 2.5mm for a 3mm diameter excitation beam. The laser power density was attenuated to approximately 0.35MW/cm² at the sample surface. The scanning system was set to move over an area of 0.7mm x 7mm which contained a through-the-thickness crack in an aluminum sample and to capture signals at 10 x 100 points. To create an image, the system analyzed the peak-peak displacement signal at each point and stored these values in a 10 x 100 matrix which was used to assign a 0-255 grayscale level dependant on the relative values when all of the data was stored. At each point in the measurement, a time-vs-displacement signal trace was captured and stored permitting post-measurement analysis of the data and the resulting image.

A diagram of the beam orientation and scanning direction, relative to the surface crack, can be seen in Figure 83. The peak-to-peak values of the averaged waveforms are then displayed in a greyscale image in Figure 84.

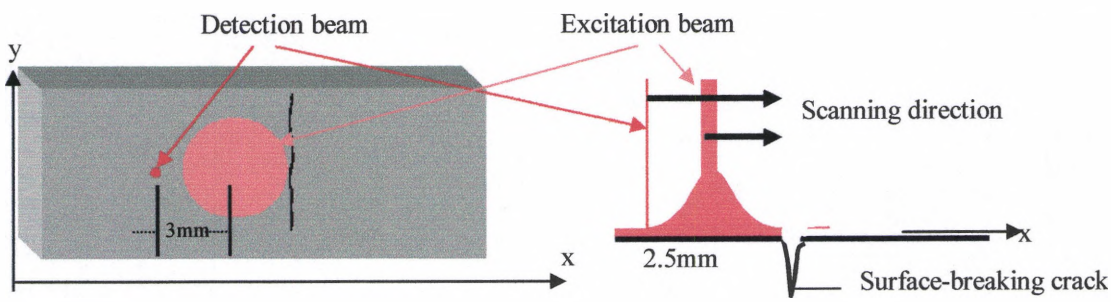

Figure 83 Diagram showing location of beams and scanning direction over crack.

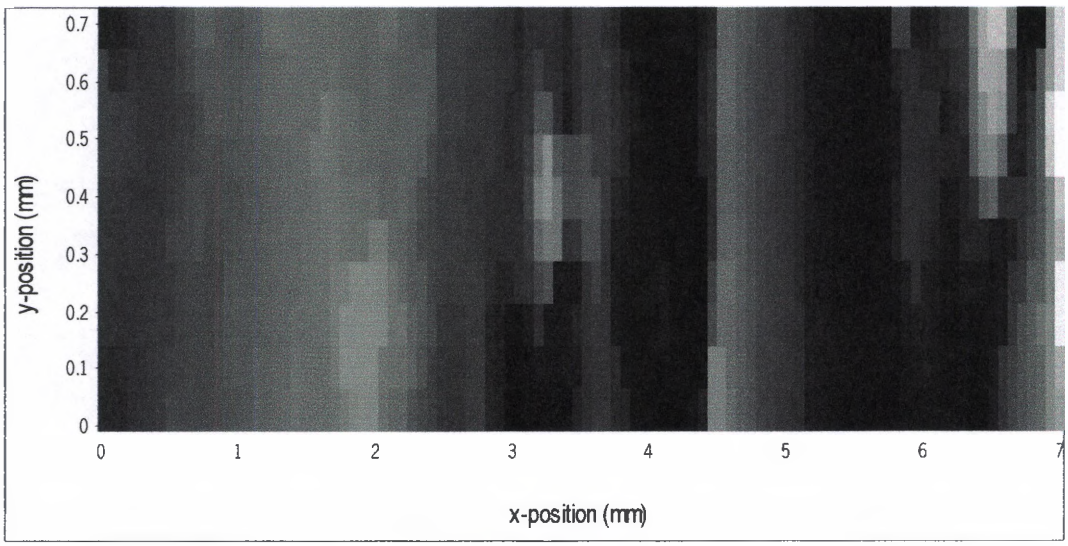

Figure 84 Peak-to-peak displacement field image of a dual beam, 7.0mm x 0.7mm scan over surface breaking crack.

The peak-to-peak image (shown in Figure 84) does not appear to display a clear representation of the surface breaking crack. The image shows significant intensification of the ultrasonic surface wave fields (represented by the brightest spots) at many positions across the entire measured area, and at regions where the surface crack was not present. In order to understand why the crack was not clearly imaged, the data obtained from this measurement can be displayed in a 3-dimensional surface plot representation (Figure 85).

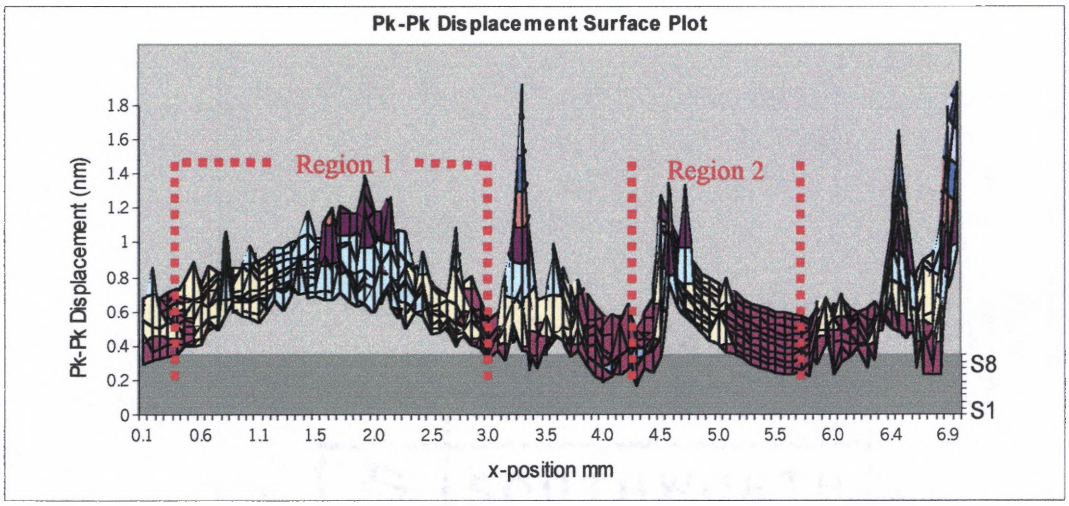

Figure 85 Surface plot of pk-pk displacement for dual beam scanning over area 7mm x 0.7mm.

By viewing the surface plot in Figure 85, it becomes more evident that the crack is being masked by a random noise. From this representation, it can be seen that there are two distinct regions where the intensification appears to occur consistently (labeled region 1 and region 2) along with many more localized intensifications that occur within and outside of these regions. The positions in which a very large localized intensification occurs (between regions 1 and 2 and towards the 7mm x-position) is shown to be greater in magnitude then the intensification within these labeled regions and thus, are over emphasized in the greyscale image.

In order to determine the source of these sharp intensifications, the actual displacement-field waveforms along a single horizontal line scan can be examined. The single peak-to-peak displacement vs. position line to be examined (y=0) is shown in Figure 86.

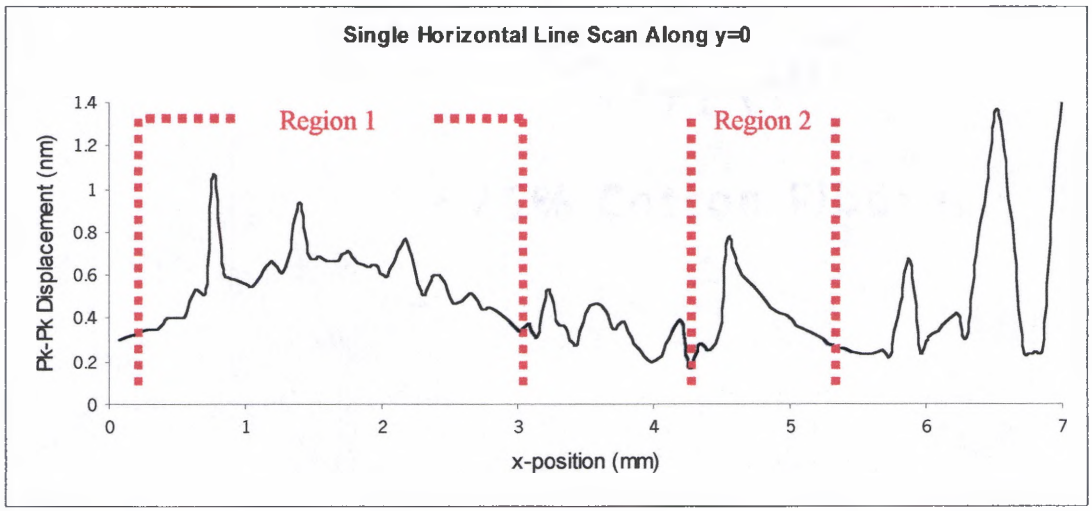

Figure 86 Single line of pk-pk displacement vs. position along the x-axis at y=0.

Further observation of the labeled regions of Figure 86 shows similarities to the intensifications which were shown in the previous sections by examining SAW interactions with a sample edge. The broad intensification of region 1 appears similar to the measurement in which only the excitation beam was scanned towards an edge. The sharp increase and decay of region 2 is similar to measurements taken in which the detection laser was scanned towards the edge. From these observations we can conclude that region 1 represents the position in the measurement where the excitation beam is scanning over the crack and the detection beam is following. Likewise, region 2 represents when the detection beam emerges onto the same side of the crack as the excitation beam which is ahead by 2.5mm.

The displacement-field waveforms which correspond to the line in Figure 86 are shown in both displacement vs. time with position vertical and displacement vs. position with time vertical in Figure 87.

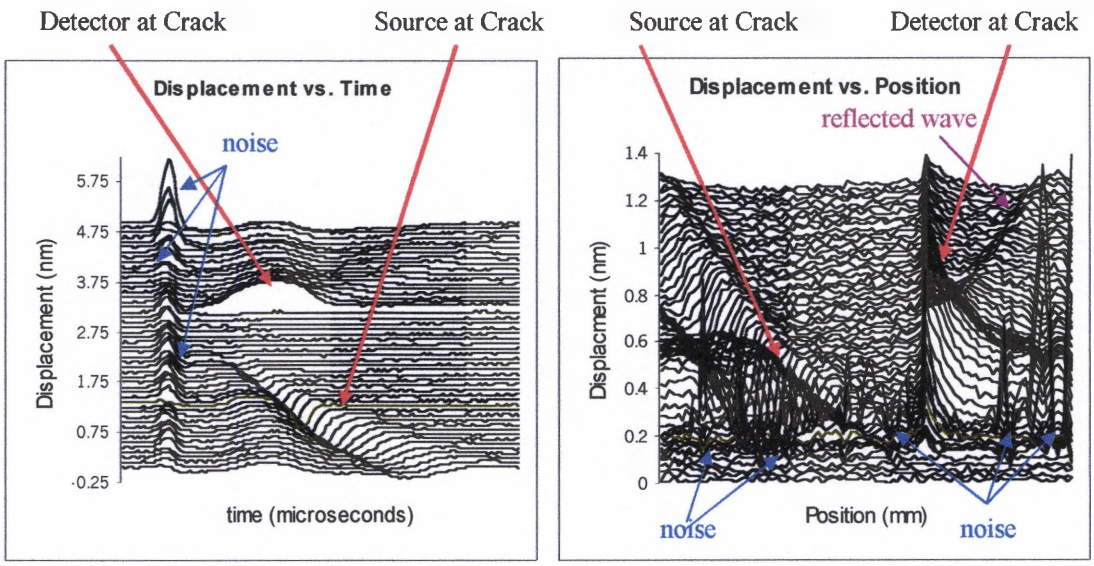

Figure 87 Cascaded waveforms of displacement vs. time (left) and displacement vs. position (right) for the line y=0.

From the plots of Figure 87, it becomes clear that the very localized intensifications, observed previously, occur earlier in time while the more consistent intensifications occur later in time. Using this observation, a time-gate window can be inserted into the data, placed just beyond this initial "noisy" waveform (Figure 88).

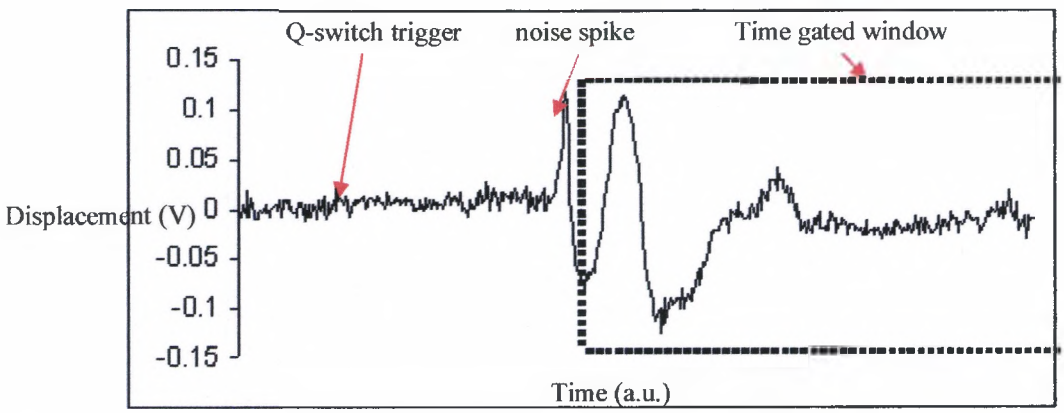

Figure 88 Placement of time window beyond initial displacement.

Using this time filter, where the data is only analyzed inside the window, the image shown earlier (Figure 84) is reproduced and shown along with the previous, unfiltered image in Figure 89.

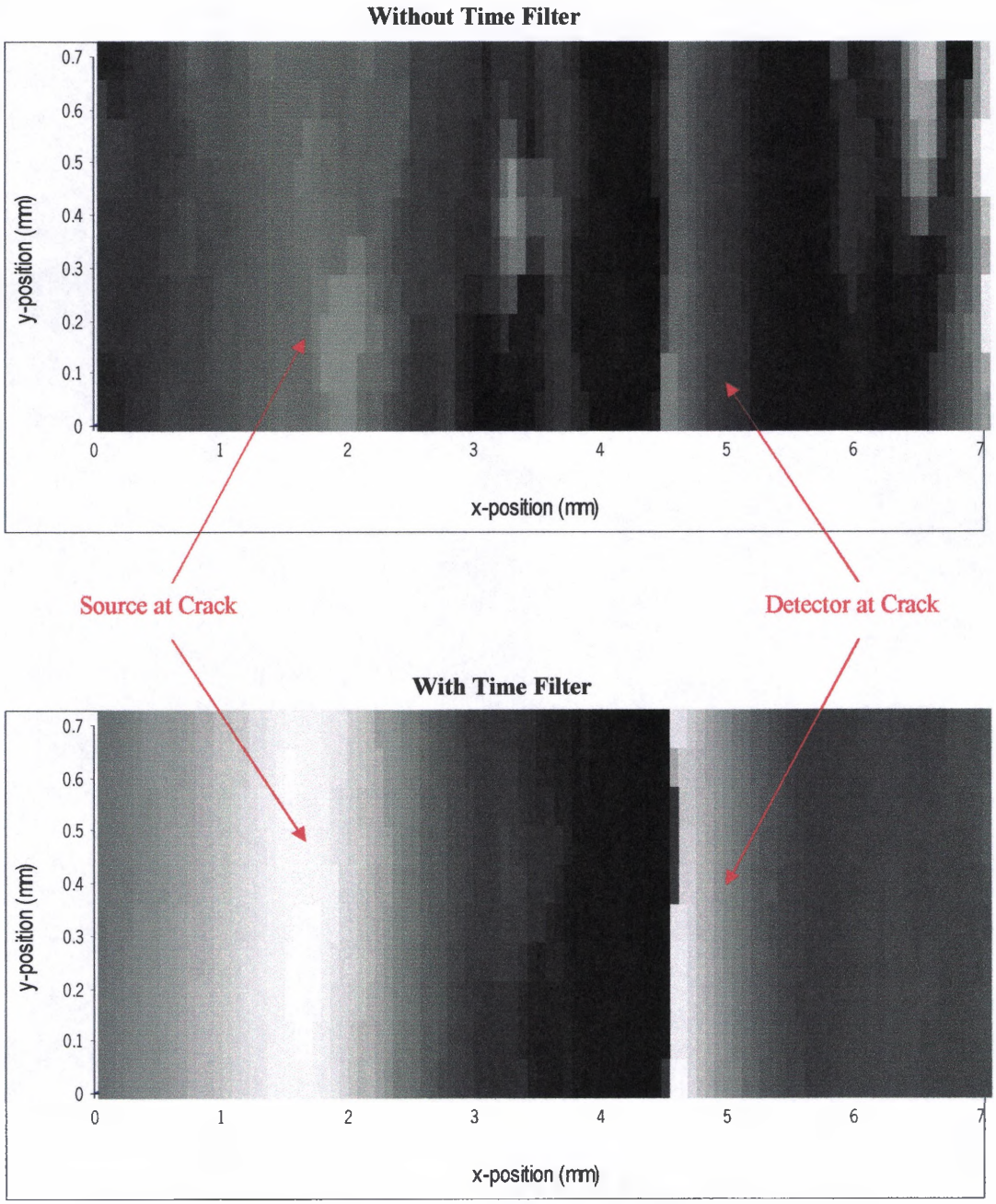

Figure 89 Image without time filter (above) and with time filter (below).

Viewing the filtered image in Figure 89, the presence of a surface breaking crack and its location now become much more evident as the noise has been decreased allowing the crack intensification to appear as the brightest points in the image.

To further enhance crack imaging capabilities, it can be seen from the waveforms in Figure 87 that the intensification which occurs as the excitation (source) beam is near the crack produces a negative going depression, while the intensification seen as the detection laser passes over the crack is a positive going surface displacement. Due to this polarity in the intensifications, the characteristic increases measured as each beam passes over the crack can be filtered and discriminated against in analysis.

As shown in Figure 89, the intensification occuring as the detection beam passes over the crack produces a sharper peak, which allows for a more resolved defect image. Analysis of only the positive going intensifications can, therefore, be used to filter out the broad peak produced by the excitation beam passing over the crack. Inserting a positive filter, which analyzes maximum displacement in lieu of peak-to peak displacement, allows for the surface plot of Figure 85 to be re-analyzed for only positive going intensifications (Figure 90).

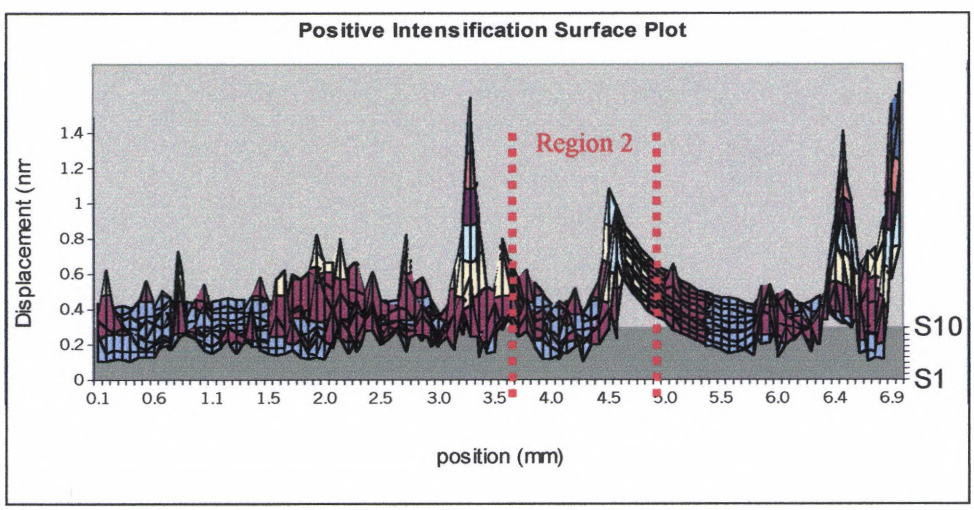

Figure 90 Image data displayed as surface plot for positive going intensification only.

Figure 90 shows that analysis of only the maximum (positive) displacement of the waveforms at each point removes the broad intensification which occurs due to the source beam passing over the crack. This surface plot has been displayed without the presence of the time filter to remove the noise. The time filter, shown in Figure 88 to produce the cleaner image in Figure 89, was placed somewhat arbitrarily into the data to remove the initial noisy waveform. It can be noticed, however, the filtered image shown in Figure 89, still retains some of the unwanted noise. For ideal crack detection capabilities, the intensification at the crack compared to the displacement levels away from the crack should be optimized. To accomplish this, a systematic investigation of the location in which the time filter is placed was carried out.

From Figure 90, the intensification of interest (region 2) is surrounded by unwanted noise. Thus the ratio of the displacement at the crack to the noise level is not sufficient for crack detection. It was shown previously though that inserting a time filter into the data can reduce the noise. To maximize the noise reduction filter, an analysis program was written using Labview to search the data for the optimal positioning of this time-gate. Details of this program can be found in Appendix C. The optimization algorithm works by comparing the desired intensification (near the crack) to the noise which occurs away from this region. The desired region is isolated by selecting a spatial window, such as shown in Figure 90, labeled region 2. All data which occurs outside this selected window is stored as an array with values x_i'. This can be considered as the "noise array". The program then analyzes the mean μ and the standard deviation σ of this noise. The program then computes, for all data points within the measurement x_i, the ratio of the difference between the value and

the mean to the standard deviation. This can be considered as the signal-to-noise ratio S/N. This ratio can then be defined as

$$S/N = \frac{x_i - \mu}{\sigma} = \frac{x_i - \frac{1}{n}\sum_{i=0}^{n-1} x_i'}{\sqrt{\frac{1}{n}\sum_{i=0}^{n-1}\left(x_i' - \frac{1}{n}\sum_{i=0}^{n-1} x_i'\right)^2}} \qquad \text{Eq. 59}$$

where n is the number of data points in the noise array x_i'.

Using this definition as the comparison of the positive crack intensification to the signal away from the crack, the program then scans a time filter through the waveform data, stored in arrays of 1024 points, in search of the optimal signal-to-noise ratio. A plot of this signal-to-noise ratio vs. the position of the time filter for the data line y=0 is shown in Figure 91.

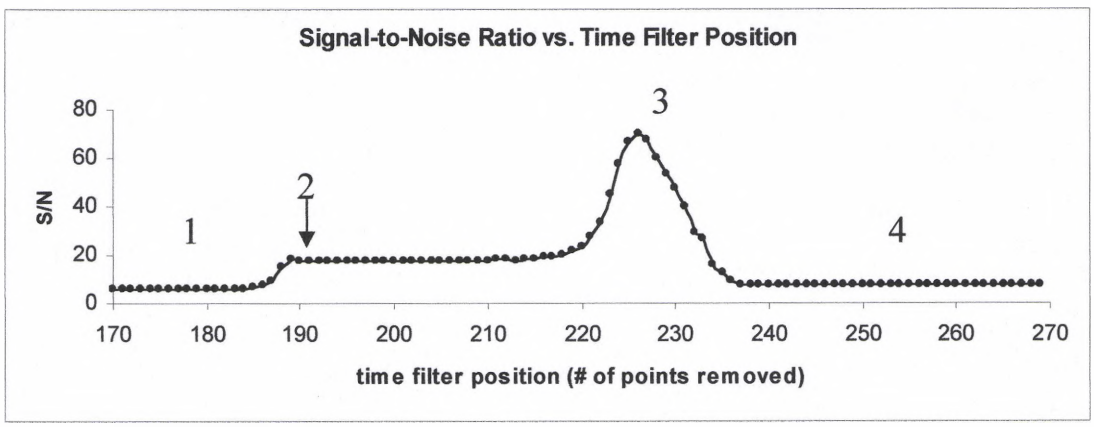

Figure 91 Signal-to-noise ratio vs. time filter position for data line y=0.

The plot in Figure 91 shows the position of the time filter has a significant effect on the comparison of the intensification at the crack to the displacement level away from the crack. The areas labeled 1-4 in Figure 91 are shown in their respective positions in the actual waveform, when the wave is at its peak positive intensification (detection beam at the crack), in Figure 92. The effect that each of

these time filter positions has on the noise level of the displacement vs. position measurements is shown in Figure 93.

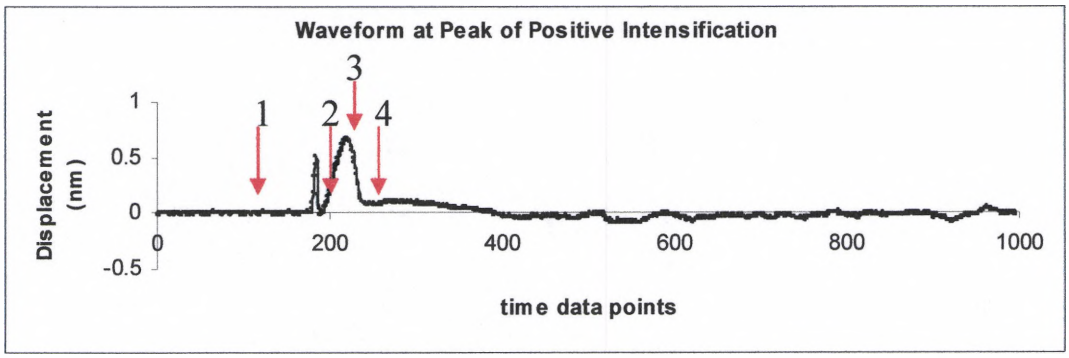

Figure 92 Diagram showing waveform at peak of positive intensification and positions of data filter corresponding to the same positions in Figure 91.

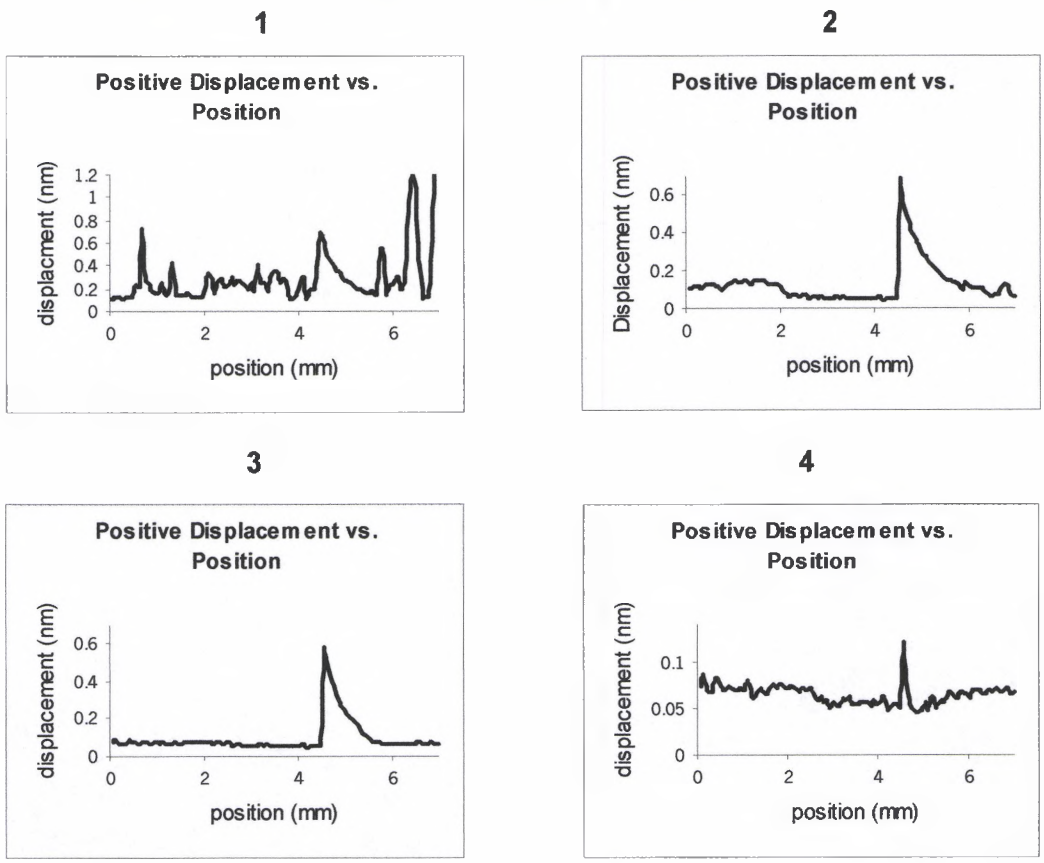

Figure 93 Displacement vs. position at each of the time data filter positions indicated by Figures 91 and 92.

Observing the level of noise away from the primary intensification in each of the plots of Figure 93 it becomes clear that the lowest noise level does indeed occur at the peak of the signal-to-noise vs. time filter position of Figure 91. Thus, in the computer analysis program, the data is analyzed for each horizontal (x-scan) data line and picks out the optimal time filter position. To compare this optimized filtering system to the original, unfiltered image data, both surface plots are shown in Figure 94. Finally, a comparison of the images produced using this optimized data processing method and the unfiltered image can be seen in Figure 95.

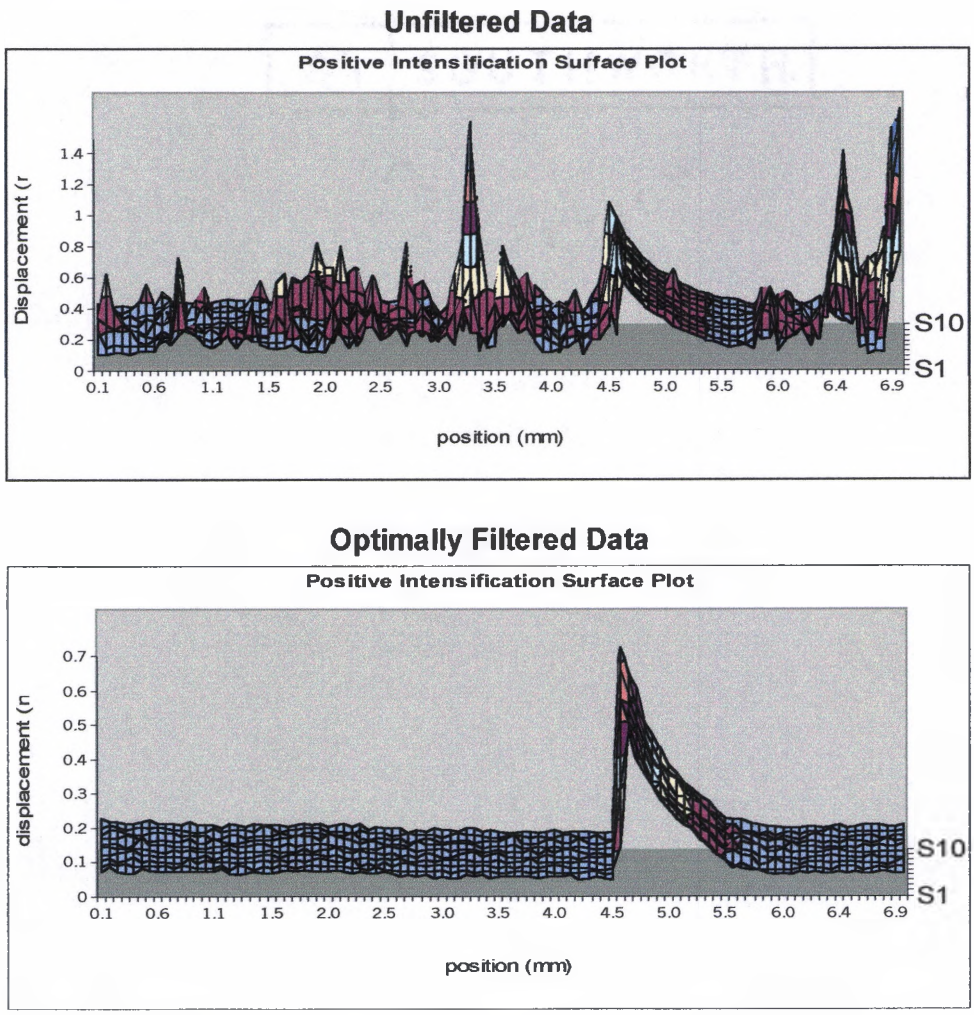

Figure 94 Comparison of unfiltered data (above) to optimally filtered data (below) in the surface plot representation.

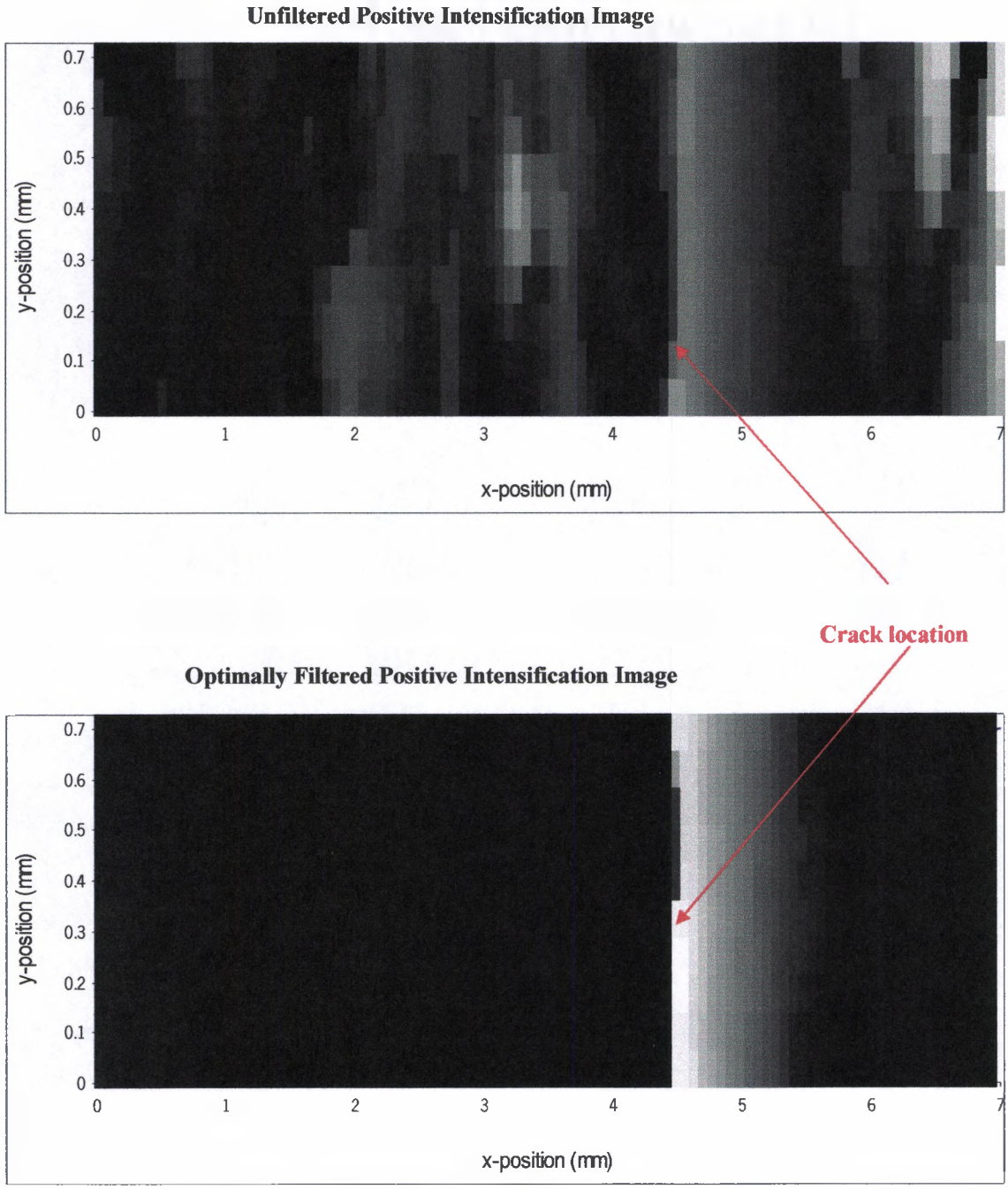

Figure 95 Comparison of unfiltered image (above) to optimally filtered image (below).

4.6 COMPARISON WITH RECENT NON-CONTACT CRACK DETECTION TECHNIQUES

The main objective of this research was to develop a completely non-contact, laser generation and detection system for imaging surface-breaking cracks. As was mentioned previously, recent laser based ultrasonic methods such as the NFSI and SLS have been shown to detect significant signal intensification in the presence of a surface defect. In this dual-beam scanning system, the observance of two distinct peaks in the crack region was observed. The noise filtered peak-to-peak image first displayed in Chapter the previous section is shown again in Figure 96.

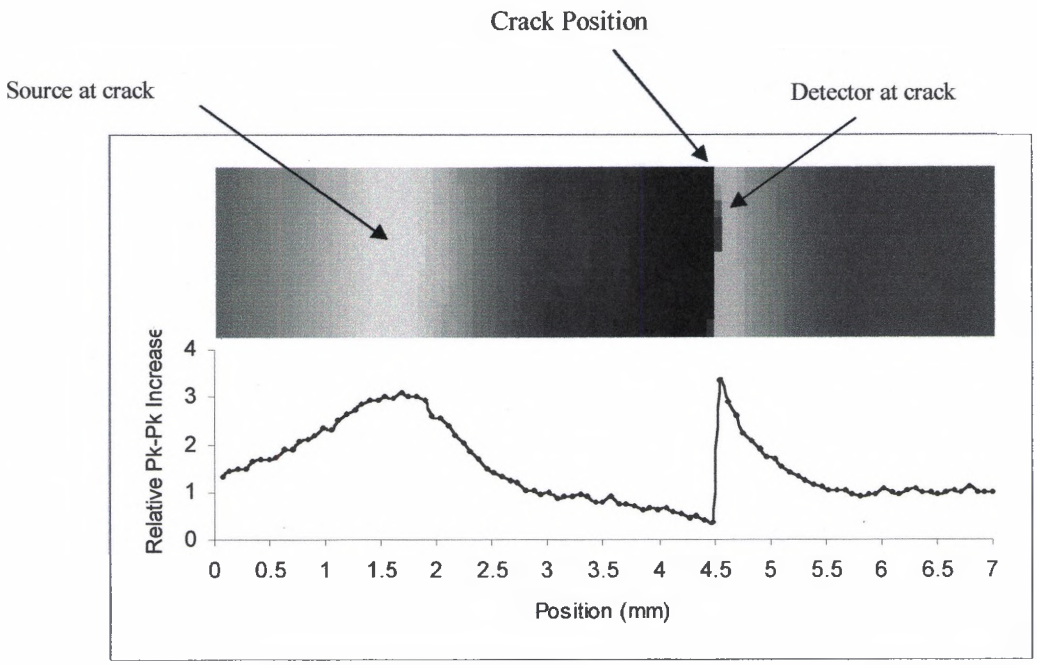

Figure 96 Peak-to-peak image of surface-breaking crack.

This double peak was attributed to the points in the scan where either the excitation laser or the detection laser is in the immediate vicinity of the crack. The broader peak corresponds to the excitation source approaching the crack while the detection laser follows. The characteristic shape of this intensification is similar to the measurements where the detection beam was left stationary and only the source is

scanned as well as results reported using the SLS technique[17]. The region in between the peaks (dark region) is a result of the beams being on opposite sides of the crack, thus little or no ultrasonic energy is detected. The sharper (right) intensification occurs as the detection beam emerges onto the same side of the crack as the source and is observed to be similar to the results obtained when the source was kept stationary while the detector was scanned, similar to the NFSI method[3,12,13,15]. Thus, in this dual-beam scanning method both the SLS and NFSI signal intensifications are detected. As was discussed in previously however, the peak attributed to the detection beam crossing the crack (NFSI technique) is sharper allowing for more resolved crack imaging.

For a qualitative comparison of this dual-beam scanning system with the NFSI technique, which utilizes a contact transducer for SAW generation, images are compared obtained using the same crack sample. The sample used was a through-the-thickness crack grown in a v-notched 50 mm x 50 mm x 10 mm block using a cyclic fatigue process[3]. A digital image along with a magnified portion of this sample is shown in Figure 97. A comparison of images obtained using both the positive intensification of the dual-beam scanning method and the NFSI techniques on this sample is then shown in Figure 98.

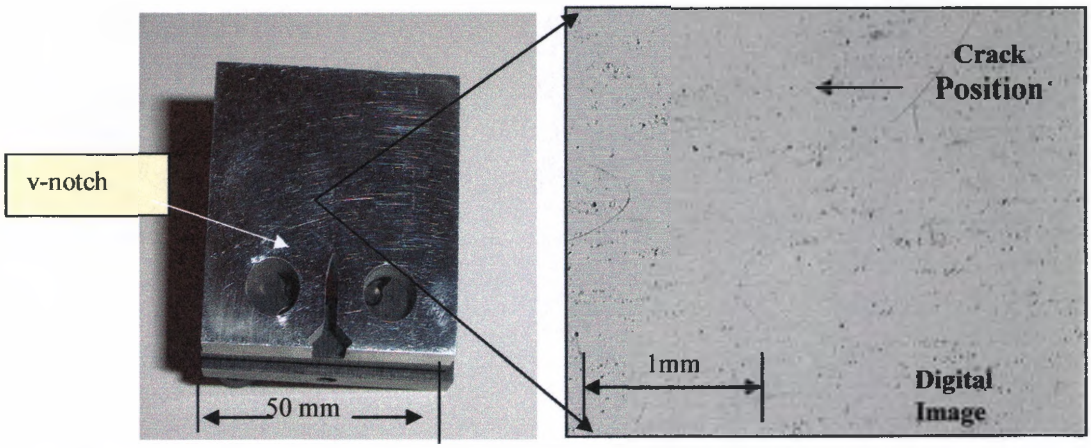

Figure 97 Digital image (left) and magnified portion (right) of crack sample[3].

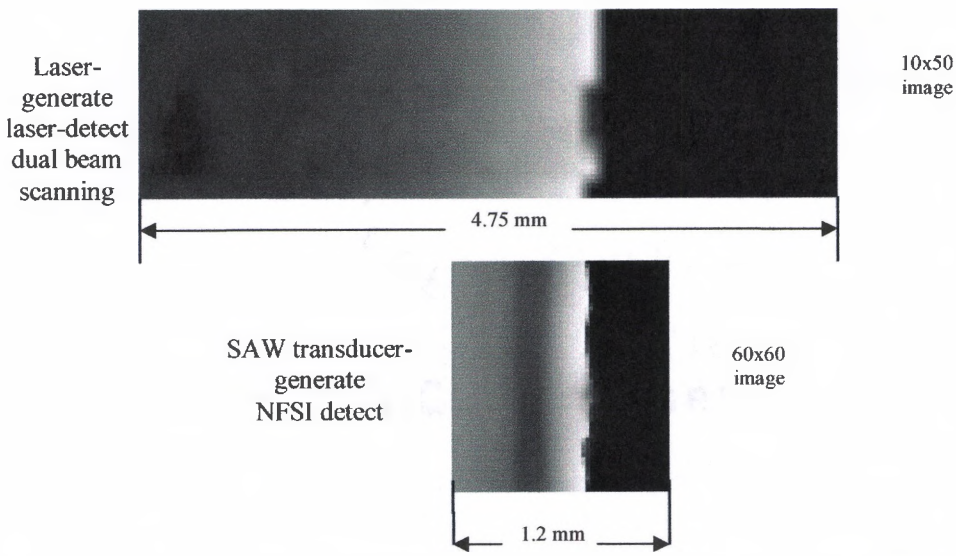

Figure 98 Images obtained using the dual-beam scanning and NFSI[3] techniques on a through-the-thickness crack in an Aluminum sample.

These images, although not taken over the same area or position of the crack, are shown to produce similar results on the same surface-breaking crack.

CHAPTER V

CONCLUSIONS AND RECOMMENDATIONS

5.1 SUMMARY

The detection of surface breaking defects in aerospace and industrial systems is a primary goal of NDE. The capability for early detection of surface-breaking cracks, before they lead to complete system failure, ensures not only a safer environment but provides additional time for proper remedy and/or replacement of the defective component. Recently, ultrasonic crack detection has been pursued in a non-contact manner, utilizing the benefits of remote laser technology for both the generation and detection of ultrasonic surface acoustic waves. Specifically, a near-field scanning interferometry technique (NFSI) has been developed[3,11,12,15] which uses a contact transducer for SAW generation and a non-contact heterodyne interferometry system for detection. In addition to crack detection, this NFSI system has shown the ability to image SAW interaction with surface breaking defects. Another non-contact crack detection method, known as the scanning laser source (SLS)[17], has shown that scanning a generation laser also provides the capability for surface crack detection. The motivation for this research was to combine both a laser generation source with a laser detection system for the purpose of detection, characterization, and ultimate imaging of surface-breaking cracks in a manner similar to the NFSI technique.

The results of this investigation showed that crack detection capabilities, for a dual-laser beam scanning configuration, were optimized for a closely positioned (near-field) source and receiver. A systematic investigation of source-receiver separation on the ability to detect relative free-boundary intensifications was conducted and revealed that the optimum position of the detection laser beam was just outside the excitation laser beam radius. This optimized positioning in the dual-beam scanning measurements was shown to be superior to techniques where either the source or the receiver was left stationary.

An automated two-dimensional scanning system was then developed in order to image surface-breaking cracks. This dual-beam scanning system was shown to detect regions of SAW intensification when either the detection or excitation laser passed over the crack thus providing data similar to both the NFSI technique and the SLS method in a single measurement. A noise reducing algorithm was also created to improve significantly the signal-to-noise ratios of the images. A qualitative comparison of images obtained using this method and the NFSI technique, on the same surface-breaking crack, showed similar results.

5.2 RECOMMENDATIONS FOR FUTURE WORK

While the preliminary crack imaging results obtained using this technique was comparable to the NFSI method on a simple, straight through-the-thickness crack sample, additional measurements on more complicated surface defects should be conducted and compared. Additionally, for practical purposes, a dramatic miniaturization of the experimental system should be attempted with the goal of developing a portable non-contact crack detection system as the current system is limited to laboratory use only.

APPENDIX A

THERMOELASTIC SURFACE DISPLACEMENT MODEL

The numerical technique used for the evaluation of equation 35 was developed using Labview. The program consists of four primary levels; (1) the spatial integration or summation of weighted line sources, (2) the time convolution of the Green's functions with the temporal profile of the laser pulse, (3) the time step layer, and (4) an observation point layer to observe the change in the waveform with increasing distance from the source center. Upon completion, all simulated waveforms are stored in a spreadsheet file. This entire program, in diagram form, is shown in Figure 99. The program output, displayed in a Labview front panel can be seen in Figure 100.

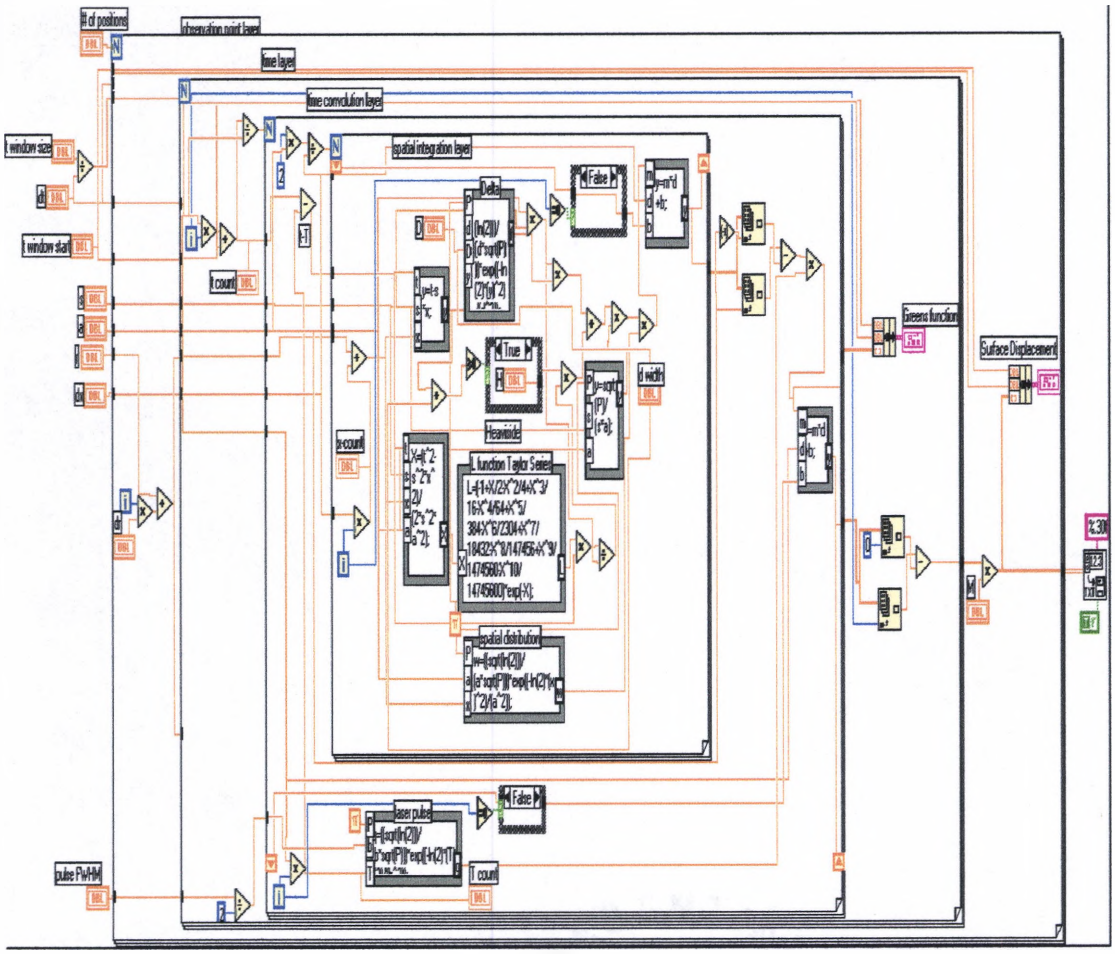

Figure 99 Numerical program displayed in a Labview diagram format.

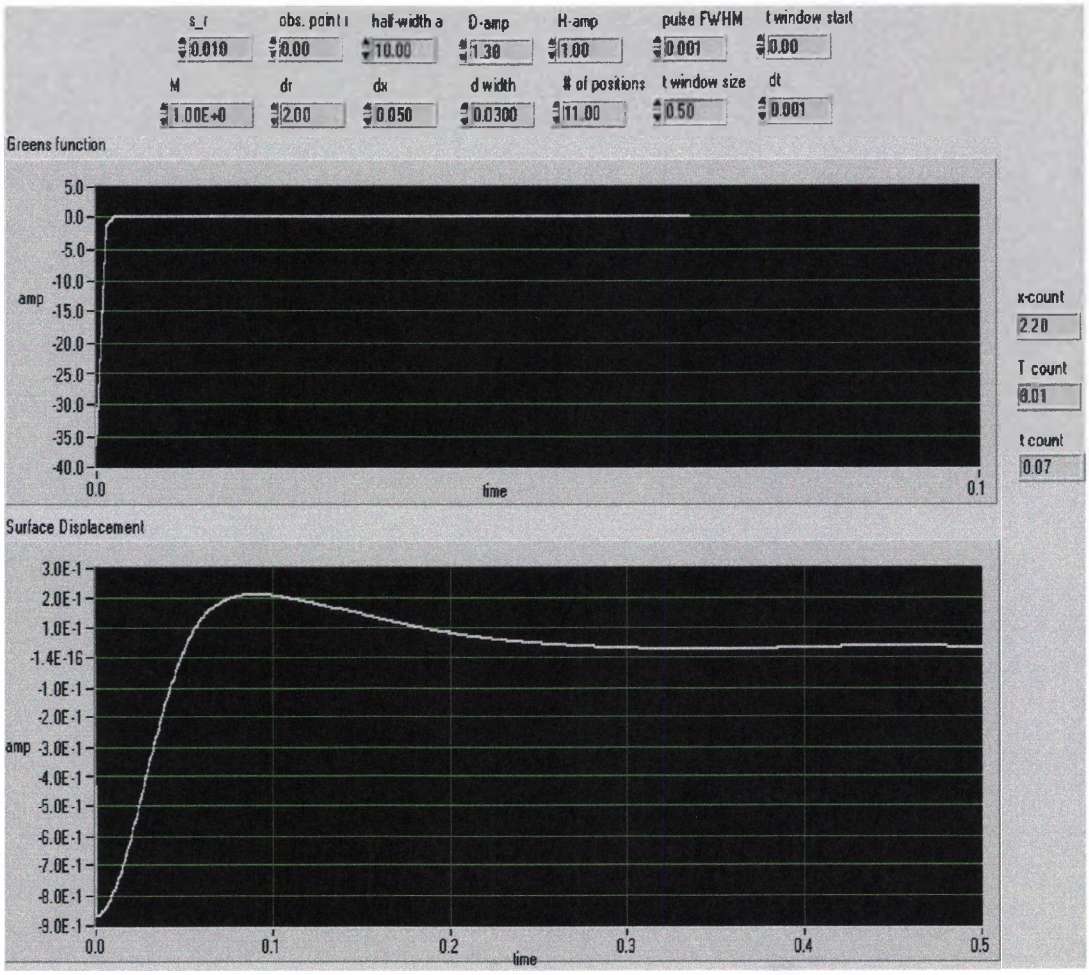

Figure 100 Front panel display showing both the Green's function and the overall surface displacement.

APPENDIX B

AUTOMATED DUAL BEAM SCANNING SYSTEM

The automated system described in Chapter 3 was developed using Labview. The front panel for the system is shown in Figure 101. The diagrams are also shown in Figures 102 through 110.

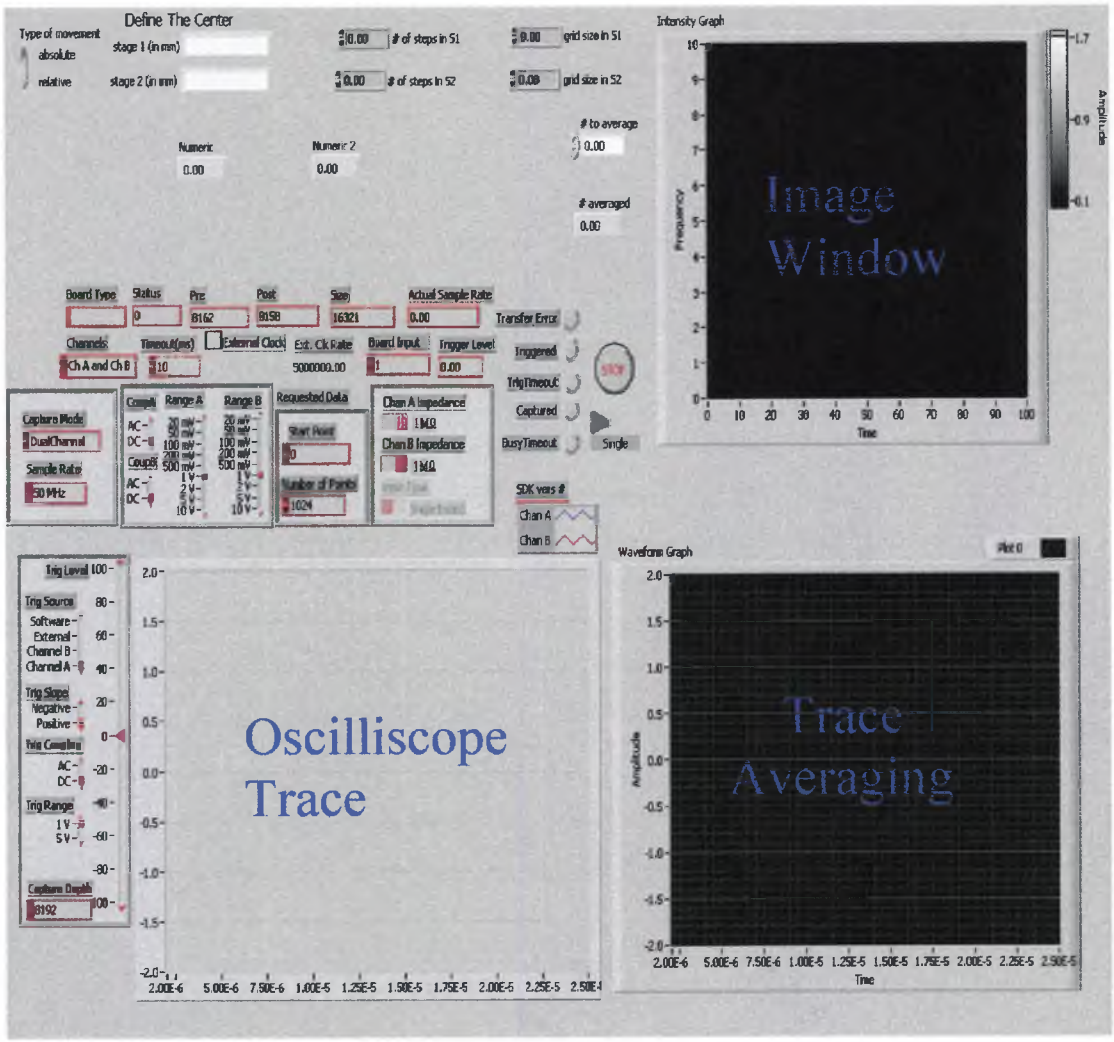

Figure 101 Front panel of Dual-Beam Scanning automated surface crack imaging system.

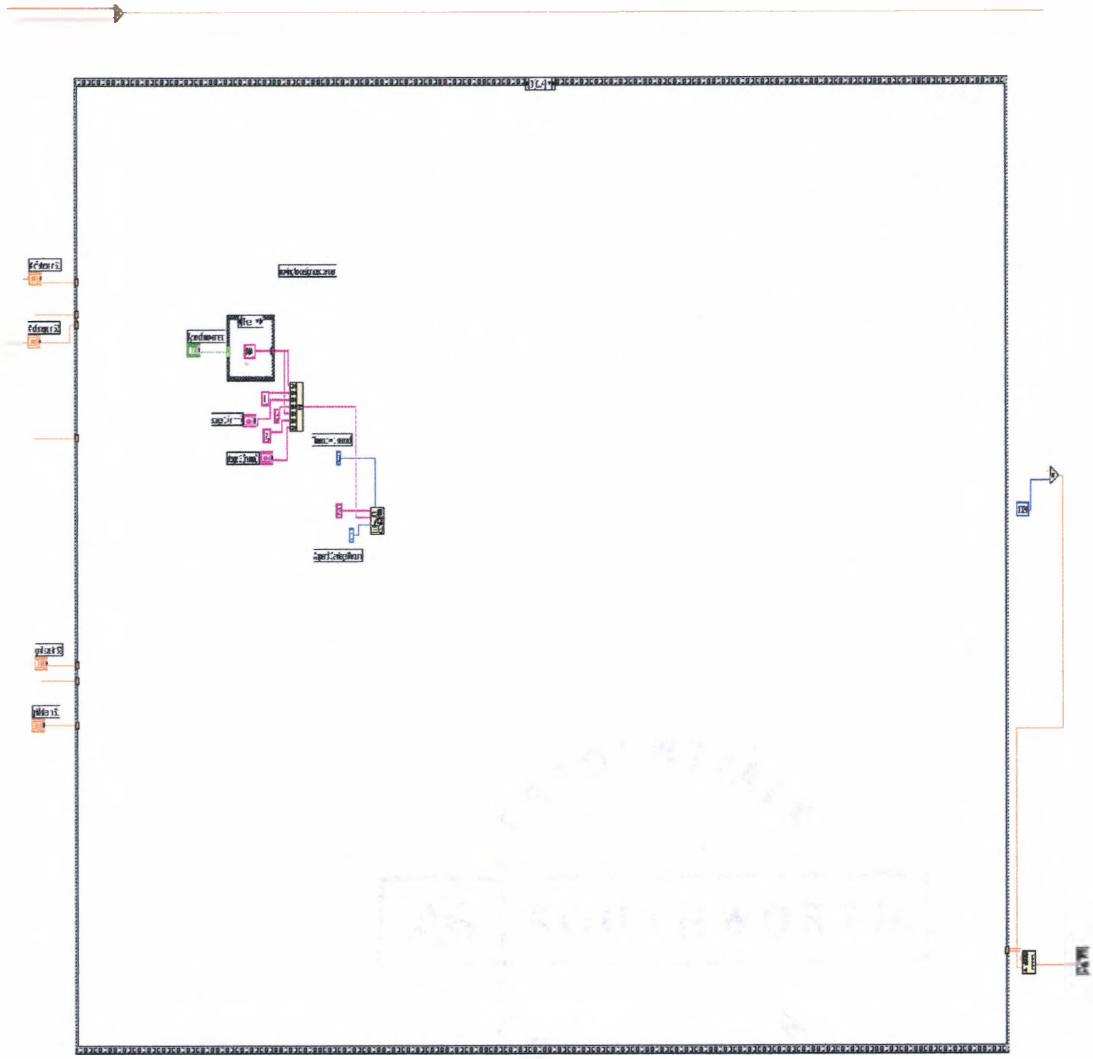

Figure 102 Labview Program: Frame 0.

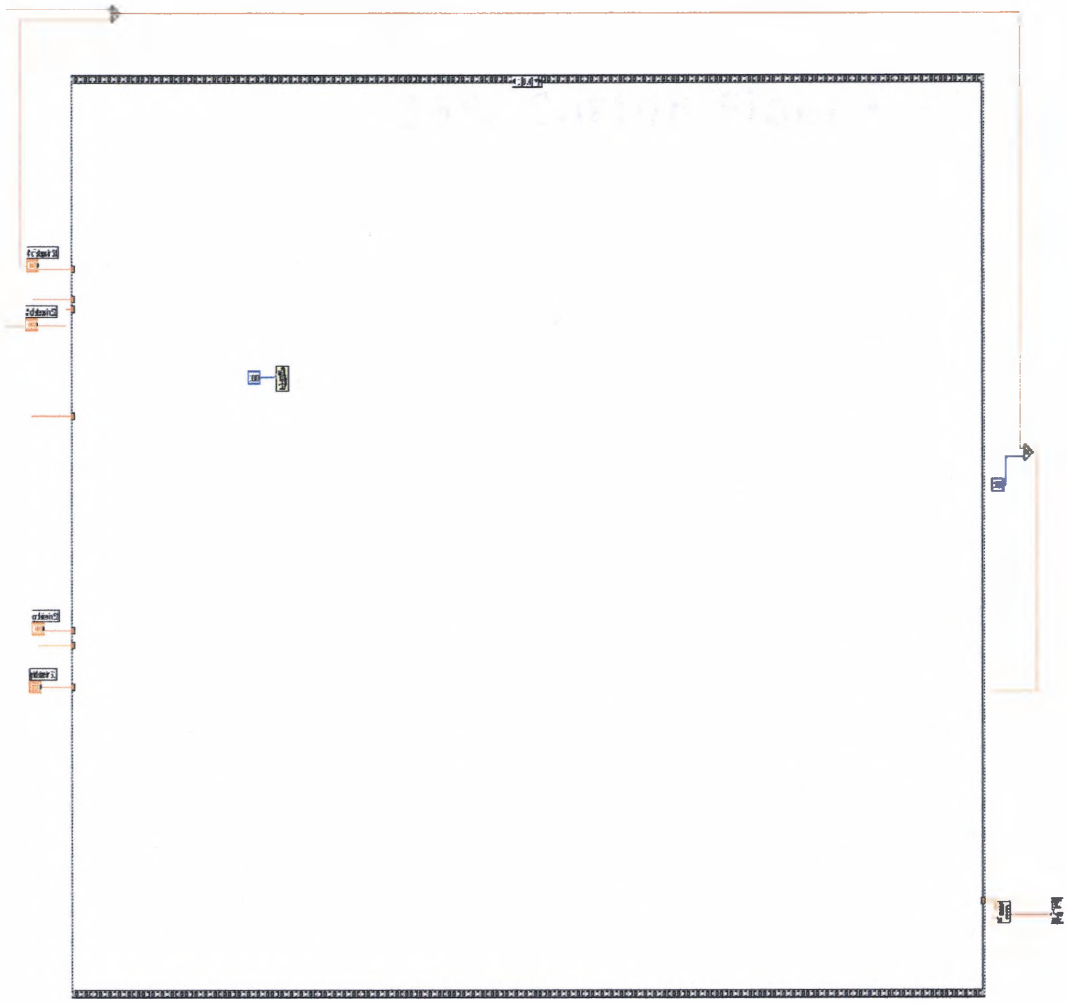

Figure 103 Labview Program: Frame 1.

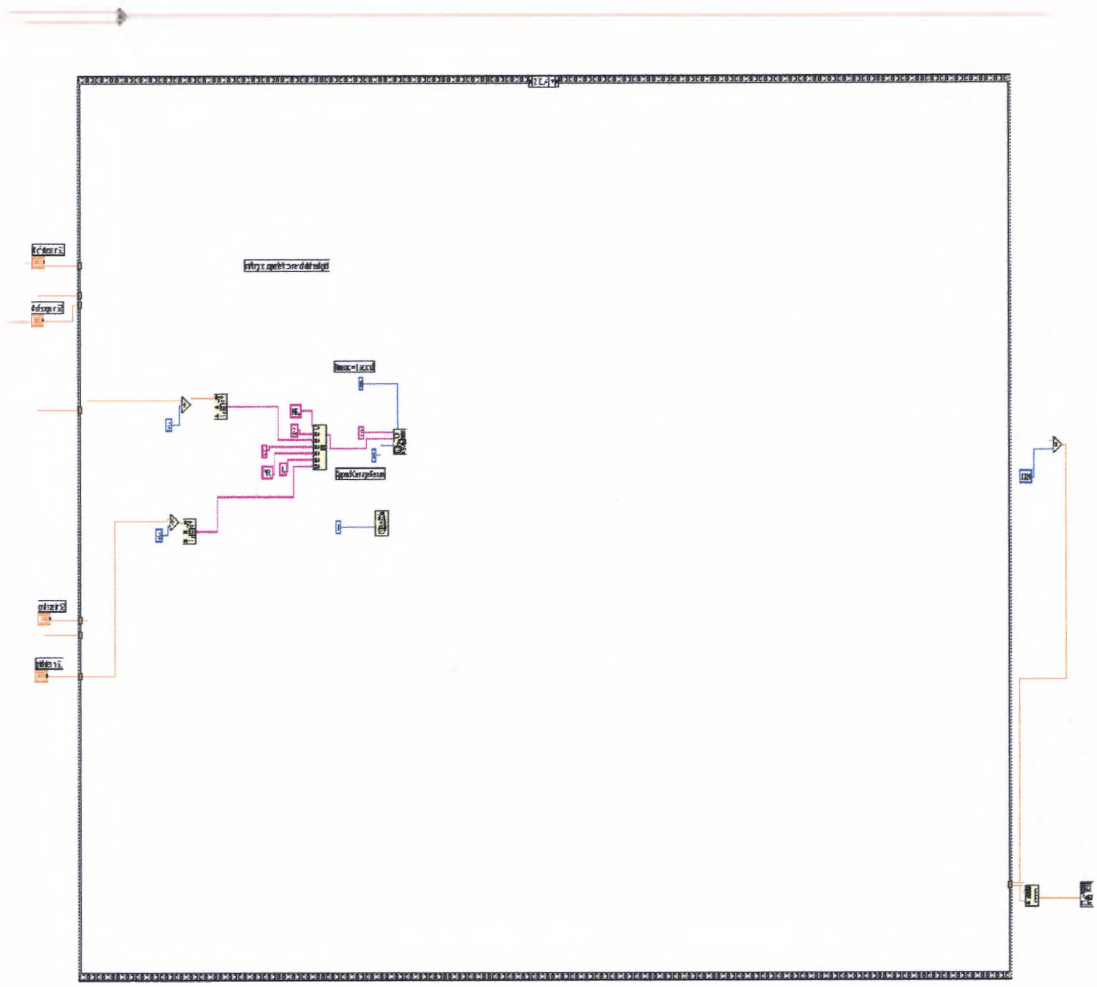

Figure 104: Labview Program: Frame 2

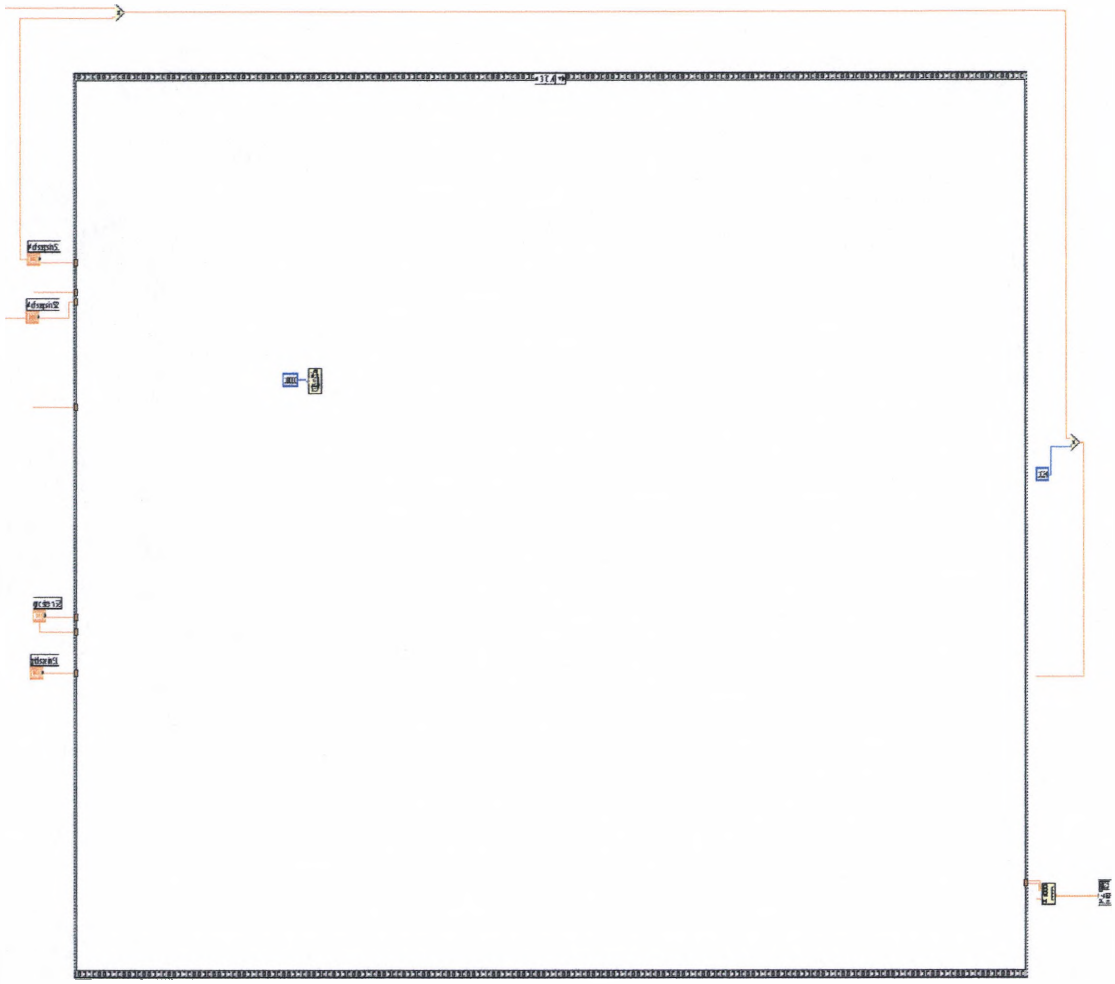

Figure 105: Labview Program: Frame 3.

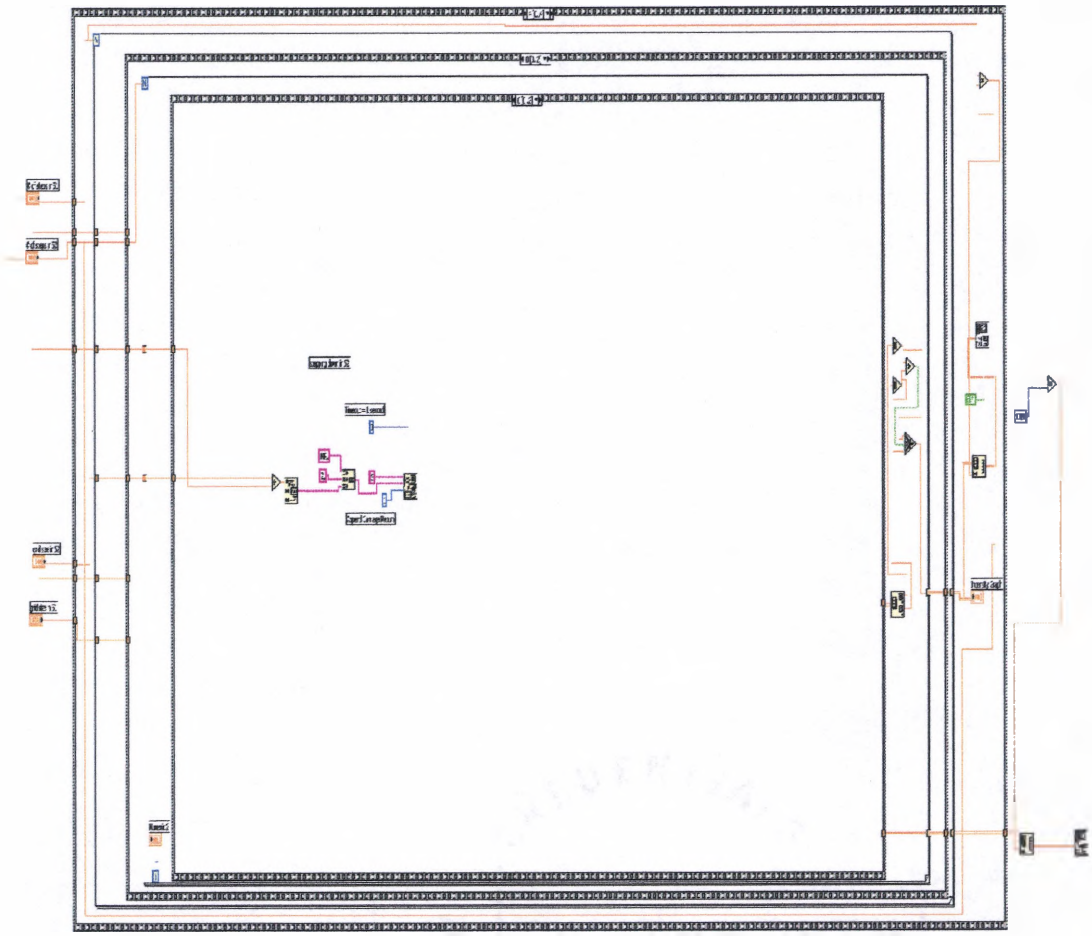

Figure 106: Labview Program: Frame 4.0.0

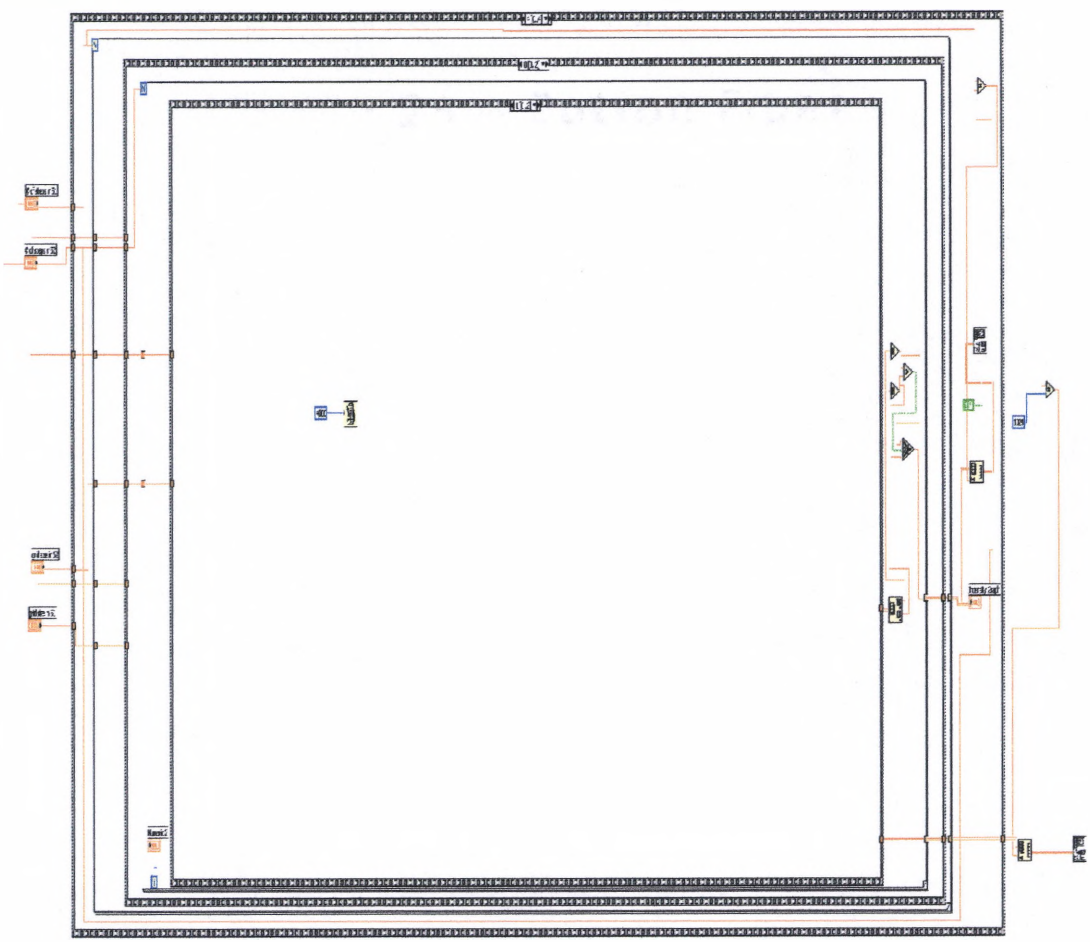

Figure 107: Labview Program: Frame 4.0.1

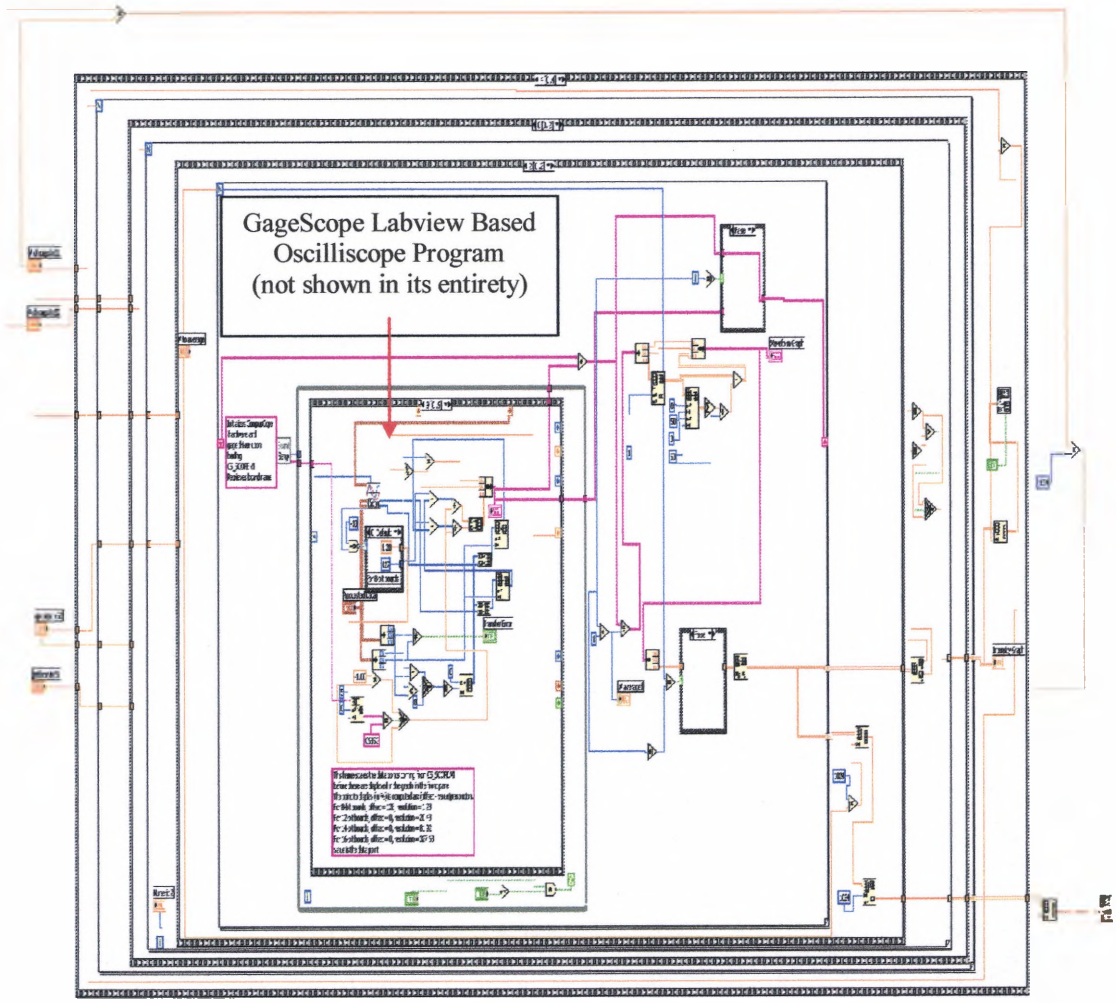

Figure 108: Labview Program: Frame 4.0.2

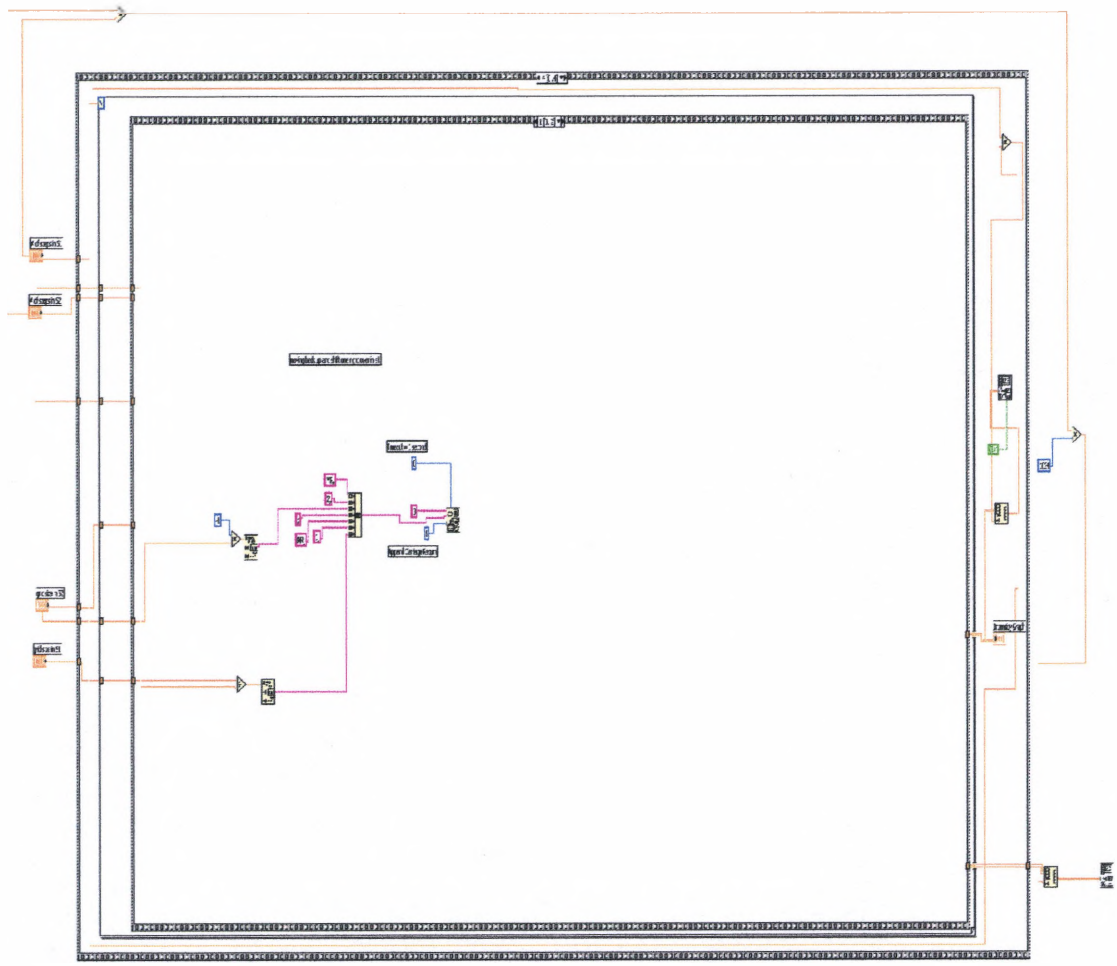

Figure 109: Labview Program: Frame 4.1

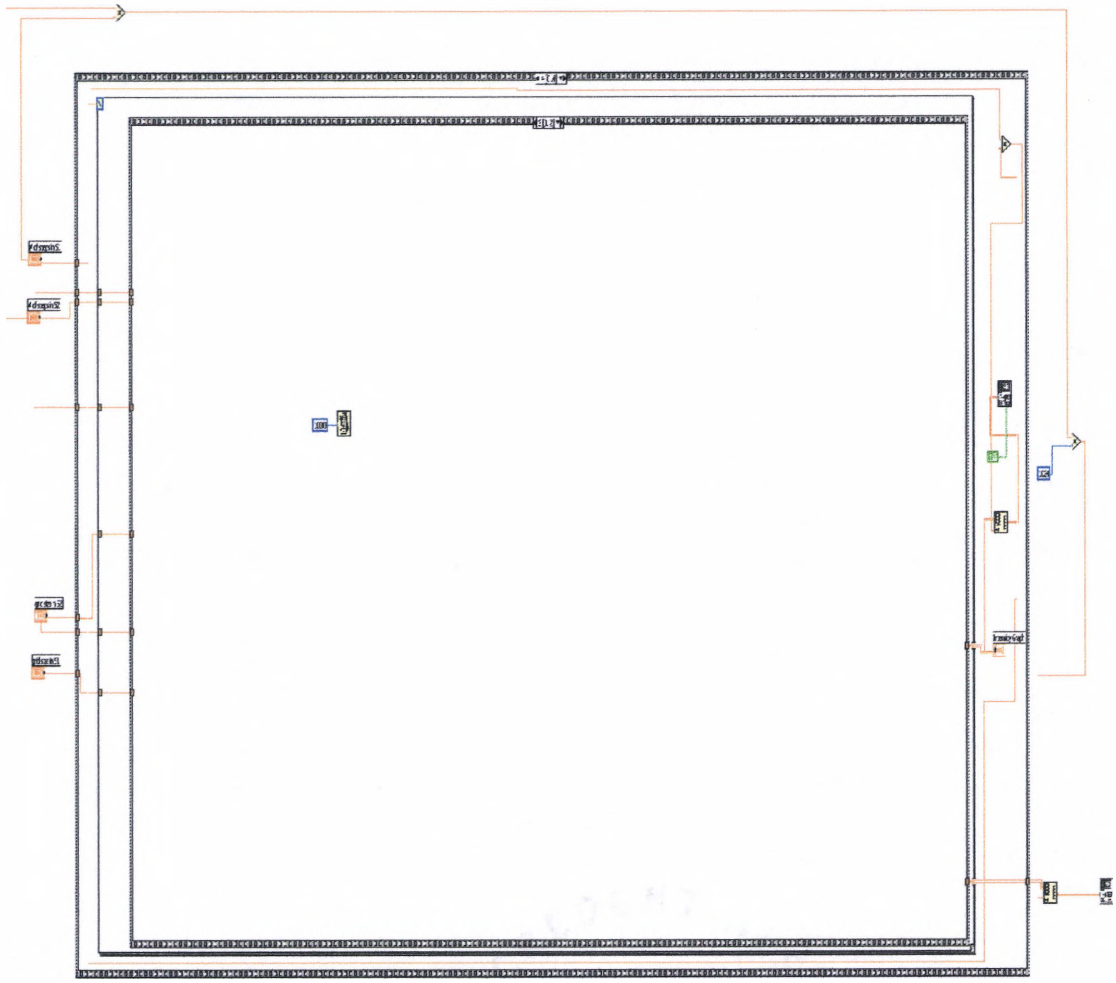

Figure 110: Labview Program: Frame 4.2

APPENDIX C

IMAGE NOISE FILTERING AND ANALYSIS PROGRAM

The data filtering process outlined in Chapter 4 was accomplished using an analysis program developed using Labview. As mentioned earlier, the program filters through each captured waveform and searches for the optimal time window which produces the greatest signal-to-noise ratio (defined in Chapter 4). In the program, the user enters the relevant experimental information (number of lines, points, window size etc.) A positional isolation window must also be defined. This window defines how the program distinguishes between the area of interest (possible crack intensification) and the external waveform noise. Thus, in a significantly noisy original image, one containing many bright intensification regions, one specific region, presumably a guess of the possible crack location, would be entered. The program then runs an algorithm in an attempt to isolate this intensification from the noise by systematically scanning a time resolved filter. The Labview diagram for this optimal time filter positioning program is shown in Figure111. The front panel for this portion is also shown in Figure 112. After running this algorithm, the program stores the values corresponding to the best time filter positions for each line in the image and then passes this information to a second program.

This second program (diagram shown in Figure113 and front panel shown in Figure114) retrieves these optimal data cut values and re-analyzes the data. This program allows for the data to be analyzed in several different manners; positive

intensification (max), negative intensification (abs. min), peak-to-peak analysis, and in terms of the standard deviation of each waveform. This portion of the program can also be run without using the optimal data filters and thus can analyze the raw data or using manually placed filters. At the completion of the program, line intensity files and images are stored for each of the analysis techniques mentioned previously.

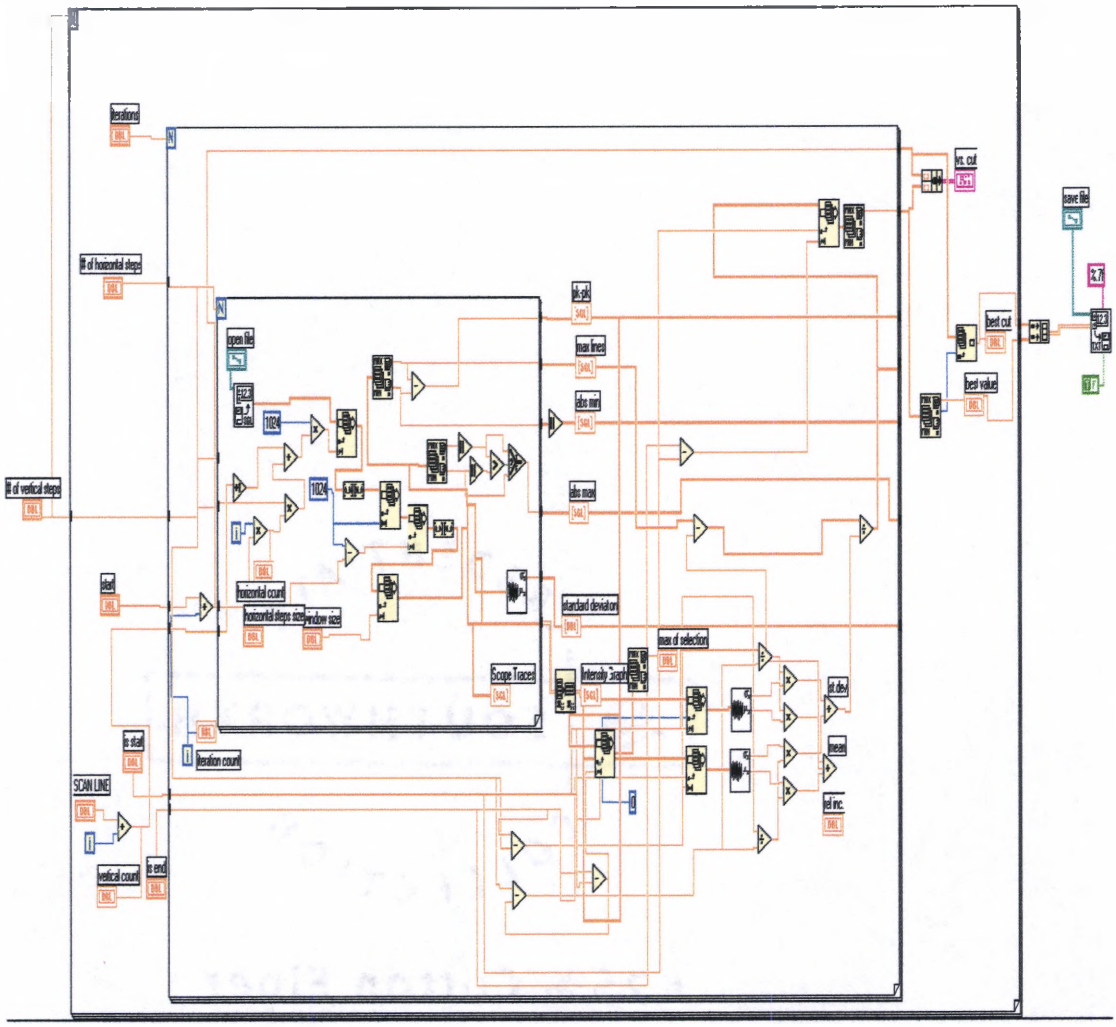

Figure 111 Labview diagram for the determination of optimal time filter positions.

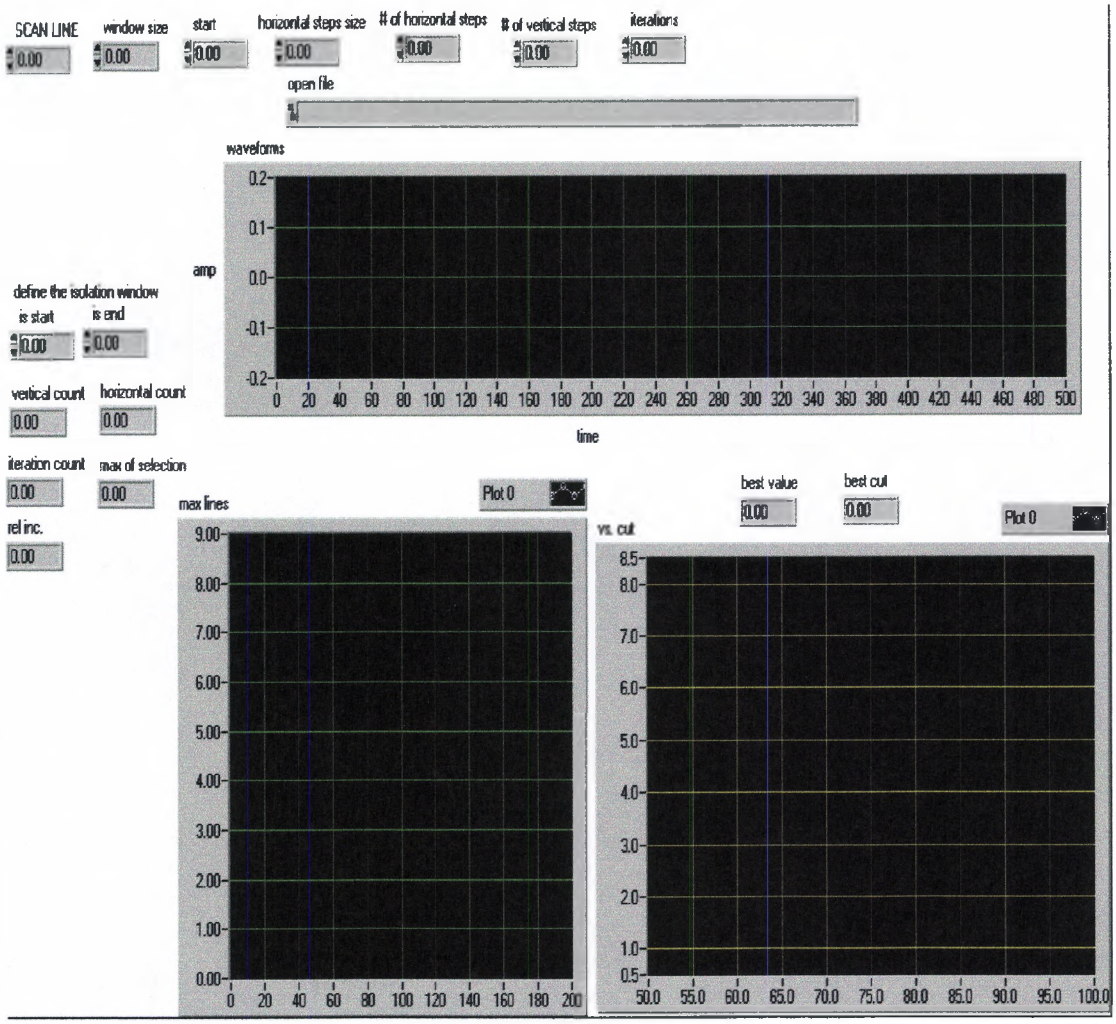

Figure 112 Labview front panel for the determination of optimal time filter positions.

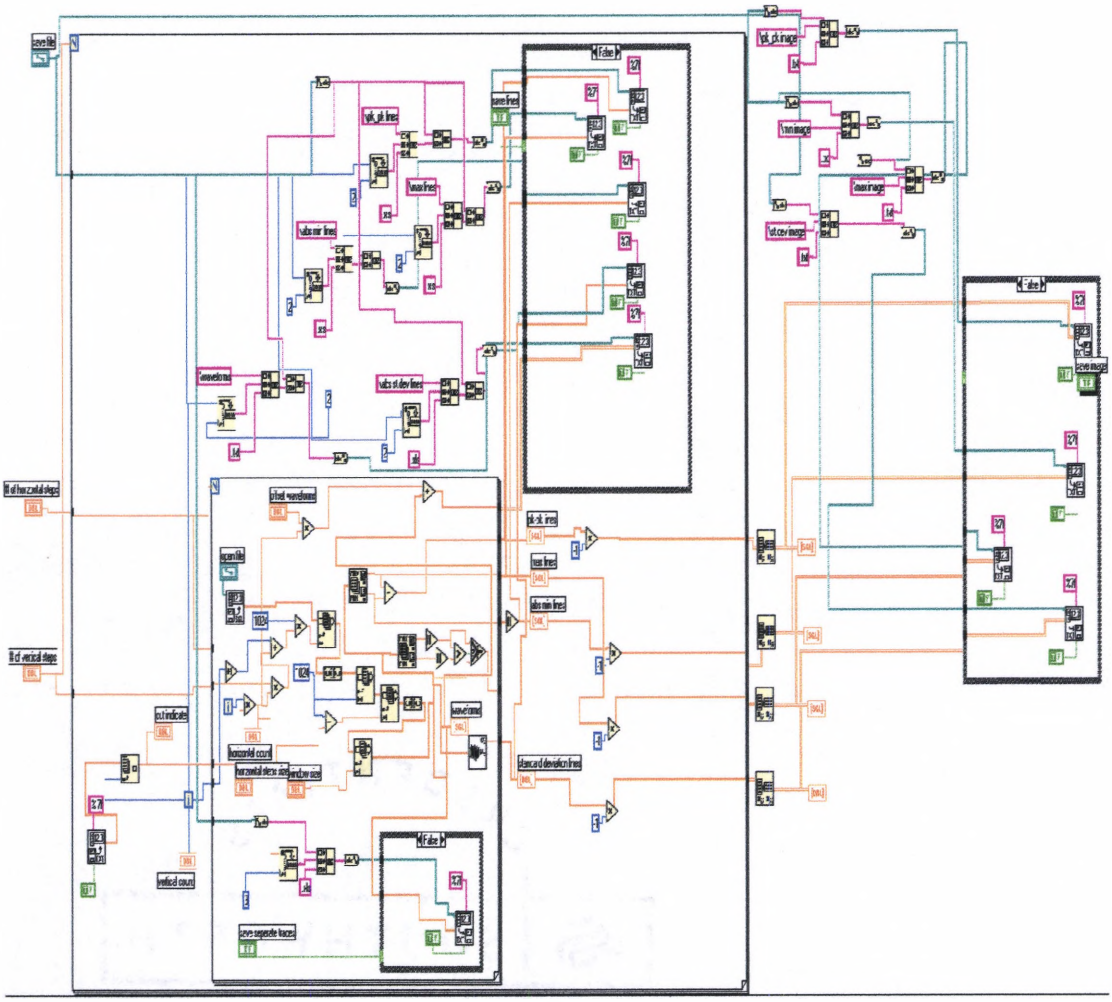

Figure 113 Labview diagram for re-analyzing using optimal time filter positions.

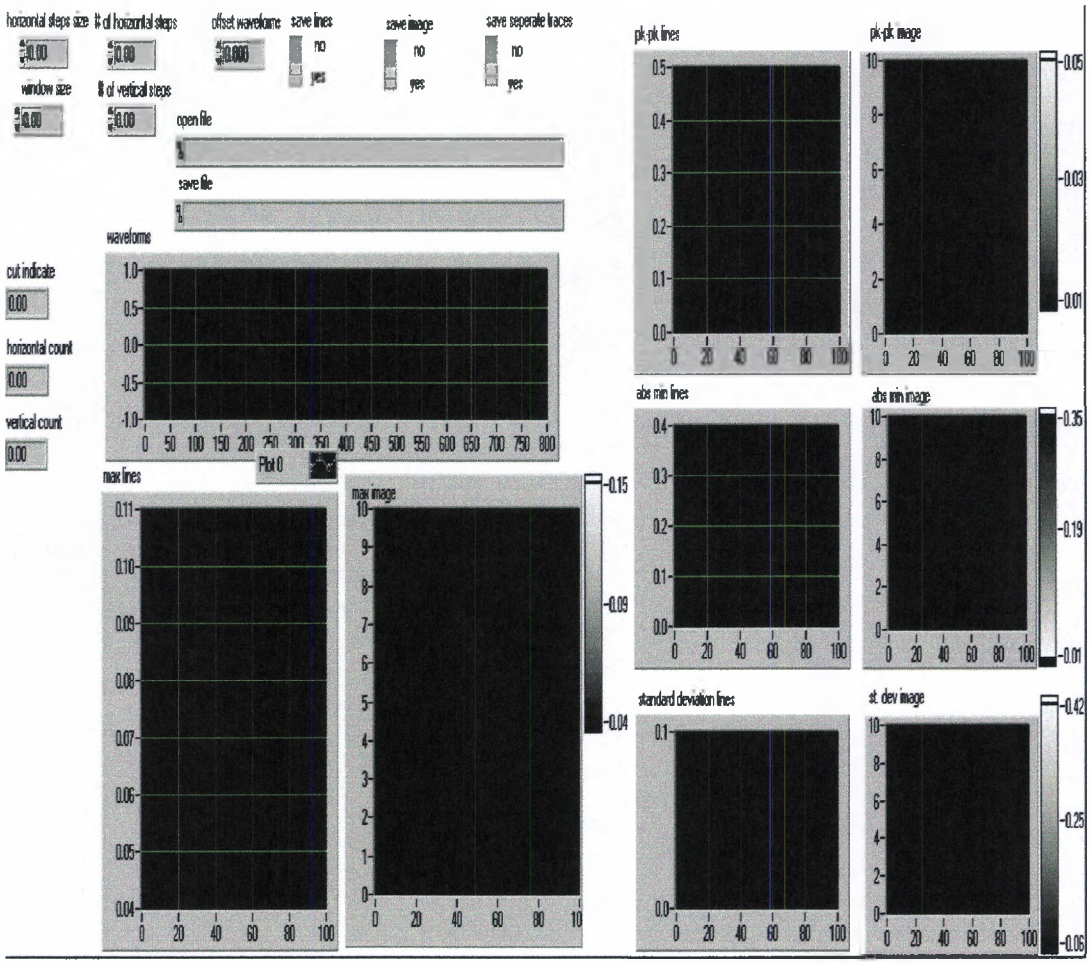

Figure 114 Labview front panel for re-analyzing using optimal time filter positions.

BIBLIOGRAPHY

1. L. Cartz, *Nondestructive Testing*, (ASM International, Materials Park, OH, 1996).

2. B. Hull, and V. John, *Non-Destructive Testing*, (Springer-Verlag, New York, 1988).

3. J. Blackshire, "Advanced Holographic and Interferometric NDE Imaging for Quantitative Microcrack Evaluation," Doctoral Thesis, University of Dayton, 2003.

4. Scruby and Drain, *Laser Ultrasonics* Adam Hilger, Bristol, 1990.

5. Achenbach, J.,*Wave Propagation in Elastic Solids*, North-Holland Publishing Company, New York, 1980.

6. Thompson, R., and Thompson, D., "Ultrasonics in nondestructive evaluation," Proc. IEEE, Vol. 73, 1985, p. 1716.

7. Buck, O., Frandsen, J., Marcus, H., *Fatigue Crack Growth Under Spectrum Loads*, ASTM Publishing, Philadelphia, 1976.

8. Auld, B., *Acoustic Fields and Waves in Solids, vols. I and II*, Krieger Publishing Company, Malabar, Florida, 1990.

9. Varadan, V.K., Varadan, V.V., *Elastic Wave Scattering and Propagation*, Ann Ar-bor Science Publishers, Ann Arbor, Michigan, 1982.

10. Her, S., Lu, S., "The Diffraction of Elastic Waves on the Tip of Slots," Journal of Nondestructive Evaluation, Vol. 20, No. 4, 2001, p. 133.

11. J. Blackshire, and S. Sathish, "Near-field ultrasonic scattering from surface-breaking cracks," *Applied Physics Letters*, 80(18):3442-3444, (2002).

12. J. Blackshire, S. Sathish, B. Duncan, and M. Millard, "Real-time, frequency-translated holographic visualization of surface acoustic wave interactions with surface-breaking defects," *Optics Letters*, 27(12):1025-1027, (2002).

13. J. Moulder, N. Nakagawa, K. No, Y. Lee, and J. McClelland, "Photoinductive imaging: a new NDE technique," in *Review of Progress in Quantitative NDE*, 8A, edited by D. Thompson and D. Chimenti, (Plenum, New York, 1989).

14. L. Favro, R. Thomas, X. Han, Z. Ouyang, G. Newaz, and D. Gentile, "Sonic infrared imaging of fatigue cracks," *International J. of Fatigue*, 23:471-476, (2001).

15. Blackshire "Ch 4.Interferometric and Holographic Imaging of Surface Wave Patterns for Characterization of Material Degradation", Meyendorf, Nagy, and Rokhlin, *Nondestructive Materials Characterization,* Springer, 2004.

16. Scruby, Dewhurst, Hutchins, and Palmer, "Quantitative Studies of Thermally Generated Elastic Waves in Laser-Irradiated Metals," *Journal of Applied Physics*, 51(12): 6210-6216, 1980.

17. Kromine, Fomitchov, Krishnaswamy, and Achenbach, "Laser Ultrasonic Detection of Surface Breaking Discontinuities: Scanning Laser Source Technique," *Materials Evaluation*, 173-177, 2000.

18. Nagy, Xiao, and Yan, "Ch 6. Ultrasonic Fatigue Crack Detection in Aluminum and Titanium Alloys", Meyendorf, Nagy, and Rokhlin, *Nondestructive Materials Characterization,* Springer, 2004.

19. Aldrin, Knopp, Blackshire, and Sathish, "Models and Methodology for Characterization of Surface-breaking Cracks Using Ultrasonic Near-field Scattering Measurement," *30th QNDE Conference*, Madison, WI, July, 2003.

20. Yim and Sohn, "Numerical Simulation and Visualization of Elastic Waves Using Mass-Spring Lattice Model," *IEEE Trans. UFFC*, 47(3): 549-558, 2000.

21. Yim and Choi, "Simulation of Ultrasonic Waves in Various Types of Elastic Media Using the Mass Spring Lattice Model," *Materials Evaluation*, 889-896, 2000.

22. Sohn and Krishnaswamy, "Mass Spring Lattice Modeling of the Scanning Laser Source Technique," *Ultrasonics*, 39: 543-551, 2002.

23. S.F Jacobs and D. Shough "Thermal Expansion Uniformity of Heraeus-Amersil TO8E Fused Silica," *Applied Optics*. 20, 3461-3463, 1981.

24. S.F Jacobs and D. Shough "Thermal Expansion Uniformity of Materials for Large Telescope Mirrors," *Applied Optics*. 23, 4237-4244, 1984.

25. P. Hariharan, "Ch 21. Interferometers," *Handbook of Optics Volume II*, McGraw-Hill Inc. 1995.

26. C. Davis, *Lasers and Electro-Optics*, Cambridge University Press, 1996.

27. T. Sanderson, C. Ume, J. Jarzynski, "Hyperbolic Heat Equations in Laser Generated Ultrasound Models," *Ultrasonics*, 33(6): 415-421, 1995.

28. White, "Generation of Elastic Waves by Transient Surface Heating," *Applied Physics Letters*, 34(12): 3559-3567, 1963.

29. H. S. Carslaw and J. C. Jaeger. *Conduction of Heat in Solids,* Oxford:Clarendon, 1959.

30. Hutchins and Tam, "Pulsed Photoacoustic Materials Characterization," *IEEE Trans. UFFC*, 33(5): 429-448, 1986.

31. L. R. F Rose, "Point-Source Representation for Laser-Generated Ultrasound," *Journal of the Acoustical Society of America*, 75(3): 723-732, 1984.

32. K. Aki and G. Richards, *Quantitative Seismology,* Freeman, San Francisco, 1980.

33. Scala and Doyle, "Time and Frequency Domain Characteristics of Laser-Generated Ultrasonic Surface Waves," *Journal of the Acoustical Society of America*, 85(4): 1989.

34. D. Royer, "Mixed Matrix Formulation for the Analysis of Laser-Generated Acoustic Waves by a Thermoelastic Line Source," *Ultrasonics*, 39: 345-354, (2001).

35. D. Royer and C. Chenu, "Experimental and Theoretical Waveforms of Rayleigh Waves Generated by a Thermoelastic Laser Line Source," *Ultrasonics,* 38: 891-895, (2000).

36. Light Age, Inc., *Pulsed Alexandrite Laser System, Operation/Maintenance Manual,* 1998.

37. A. Mourad, C. Desmet, and J. Thoen, "On the Polarity of Laser-Generated Surface Waves," *Ultrasonics,* 35: 393-397, (1997).

38. P.A. Doyle and C.M, Scala, "Near-Field Ultrasonic Rayleigh Waves From a Laser Line Source," *Ultrasonics,* 34: 1-8, (1996).